December 2022

Improved Pressure Loss And Multiphase Flow Behavior Predictions For In-Line Gas-Liquid Contactors Using Experimental Measurements And CFD Simulations

Evan Lowry

IMPROVED PRESSURE LOSS AND MULTIPHASE FLOW BEHAVIOR

PREDICTIONS FOR IN-LINE GAS-LIQUID CONTACTORS USING

EXPERIMENTAL MEASUREMENTS AND CFD SIMULATIONS

By

Evan Wesley Lowry
Bachelor of Science, University of Wyoming, 2015
Master of Science, University of Wyoming, 2016

A Dissertation

Submitted to the Graduate Faculty

of the

University of North Dakota

in partial fulfillment of the requirements

for the degree of

Doctor of Philosophy

Grand Forks, North Dakota

December

2022

Name: Evan Lowry

Degree: Doctor of Philosophy

This document, submitted in partial fulfillment of the requirements for the degree from the University of North Dakota, has been read by the Faculty Advisory Committee under whom the work has been done and is hereby approved.

Gautham krishnamoorthy
Dr. Gautham Krishnamoorthy

Michael Mann
Dr. Michael Mann

Yun Ji
Dr. Yun Ji

Frank Bowman
Dr. Frank Bowman

Anjali Sandip
Dr. Anjali Sandip

_____

This document is being submitted by the appointed advisory committee as having met all the requirements of the School of Graduate Studies at the University of North Dakota and is hereby approved.

Chris Nelson
Chris Nelson
Dean of the School of Graduate Studies

11/15/2022

Date

PERMISSION PAGE

Title   Improved Pressure Loss and Multiphase Flow Behavior Predictions for In-line
                 Gas-Liquid Contactors Using Experimental Measurements and CFD Simulations

Department   Chemical Engineering

Degree   Doctor of Philosophy

In presenting this dissertation in partial fulfillment of the requirements for a graduate degree from the University of North Dakota, I agree that the library of this University shall make it freely available for inspection. I further agree that permission for extensive copying for scholarly purposes may be granted by the professor who supervised my dissertation work or, in his absence, by the Chairperson of the department or the dean of the School of Graduate Studies. It is understood that any copying or publication or other use of this dissertation or part thereof for financial gain shall not be allowed without my written permission. It is also understood that due recognition shall be given to me and to the University of North Dakota in any scholarly use which may be made of any material in my dissertation.

<div style="text-align: right">

Evan Wesley Lowry
November 2nd, 2022

</div>

TABLE OF CONTENTS

LIST OF FIGURES

LIST OF TABLES

NOMENCLATURE

A	Cross-sectional area (m^2)
ΔB	Near-wall velocity distribution factor
C	Constant for interfacial pressure loss contribution
C_0	Empirical model constant
C_1, C_2, C_3, C_4	Empirical model constant
C_μ	Model constant = 0.09
C_s	Roughness constant = 0.5
C_p	Mixer channel frictional loss coefficient
D	Pipe diameter (m)
D_c	Mixer channel hydraulic diameter (m)
d_H	Hydraulic diameter defined by Theron et al., 2011 (m)
E	Empirical constant
e	Absolute roughness in Nikuradse equation (m)
e_{ext}^{ij}	Error of grid relative to extrapolated value
Fr_c	Froude number
f	Fanning friction factor
f_c	Mixer friction factor

f_n	Roughness correction function
g	Gravitational constant (m/s^2)
h	Representative cell size (m)
k	Turbulence kinetic energy (m^2/s^2)
K_s	Dimensional sand-grain roughness (m)
K_s^+	Dimensionless equivalent sand-grain roughness
K_s/D	Relative roughness
L	Mixer length (m)
ℓ	Streamline length (m)
L/D	Length to diameter ratio of mixing element
$\dot{m}_i$	Mass flow of phase i
N	Number of cells
N_μ	Viscosity Number
n	Power-law index
m	Power constant for two-phase flow
P	Pressure (N/m^2)
$\mathcal{P}$	Perimeter of mixer channel (m)
$Re = u_0 D\rho/\mu$	Reynolds number based on D
$Re_c = u_0 D_c \rho\tau/\epsilon\mu$	Reynolds number based on D_c
$Re_{c_i} = \rho_i u_{i_0}\tau D_c/\epsilon\mu_i$	Reynolds number of phase i based on D_c
$Re_{c_{film}} = 4\rho_L Q_L(D_c/D_{pipe})/\mathcal{P}\mu_L$	Reynolds number of liquid film on mixer channel
Re_{c_T}	Critical Reynolds number for onset of turbulent flow

Q_L	Liquid flowrate (m³/s)
r_{ij}	Refinement ratio between levels i and j
u^+	Dimensionless near-wall velocity
u	Near-wall velocity (m/s)
u_0	Average pipe flow velocity (m/s)
u_s	Superficial velocity (m/s)
ΔV_i	Volume of cell i
x	Vapor quality
y^+	Dimensionless wall distance
y	Dimensional wall distance (m)
Z	Ratio of mixer friction factor to pipe friction factor

Symbols

α_i	Correction factor for turbulent flow or non-circularity
β	Corrugation angle relative to flow axis (degrees)
Δ	Difference operator
ρ	Fluid density (kg/m³)
$\mathcal{E}_{ij}$	Error between refinement levels i and j
ϕ_L, ϕ_G	Liquid/gas two-phase frictional pressure loss multipliers
ϕ	Local variable of interest for grid refinement
ϵ	Void fraction of mixing element
μ	Dynamic viscosity (Pa · s)

π	Pi constant
ν_t	Turbulence viscosity (m^2/s)
κ	Von Karmen constant
ν	Kinematic viscosity (m^2/s)
σ	Interfacial tension (N/m)
τ_w	Wall shear-stress (kg/m·s^2)
τ	Tortuosity
$\chi = \sqrt{\Delta P_L / \Delta P_G}$	Martinelli parameter
ζ	Frictional loss coefficient of Streiff et al., 1979

Subscripts

L	Liquid
G	Gas
TP	Two-Phase
i	Phase (i.e. gas or liquid), unless otherwise noted
0	Free-stream velocity in the pipe
c	Mixer channel
crit	Critical (i.e. Critical Reynolds number)

ACKNOWLEDGEMENTS

I would like to thank my program advisor Dr. Gautham Krishnamoorthy, who always made time to help me work through a difficult concept or research problem. Without his mentorship and guidance, this program would not have been possible. Also, I thank my advisory committee members Dr. Michael Mann, Dr. Yun Ji, Dr. Frank Bowman, and Dr. Anjali Sandip. My sincerest thanks to my company program supervisor Dr. Yanxiao Yuan, who believed in me and encouraged me to embark on this journey; her support made this dissertation possible. Many thanks to Pentair for providing funding for this work and approval to continue my education.

Finally, I would like to thank my wife and son for their tireless support. Through the long evening study sessions, and weekends of research and writing, you believed in me and supported the pursuit of my goal.

ABSTRACT

Treatment of gas by liquid absorption is a common unit operation in industry. Traditionally, contact between the gas and liquid is accomplished in co-current flow utilizing a tower or column. With the increased demand for natural gas and renewable gas, higher treating capacities for new installations and methods for de-bottlenecking existing plants are needed. Co-current gas treating with static mixers is an increasingly attractive alternative for process intensification. The corrugated plate (SMV-style) mixer is currently the most widely used mixing element for gas-continuous mixing with a liquid phase and has been recommended as the best standard option for this service [1]. These geometries are also used as structured packing for counter-current service. Unfortunately, the pressure loss correlations available to the design engineer are sparse and only valid up to $Re_G < 50,000$. In contrast, most gas pipelines operate in the range of $10^5 < Re_G < 10^7$. Additionally, no robust multiphase pressure loss correlations exist for these geometries in co-current flow. Given that pressure loss is intrinsically linked to energy dispersion and mass transfer, it is critical to accurately understand this metric for a full-scale gas treating design.

To this end, an experimental campaign was undertaken to measure single- and multi-phase pressure loss in SMV-style mixers at high Reynolds number. An experimental system was constructed for this purpose and the results were utilized to inform a correlation for single-phase pressure loss based on theory. A CFD methodology was developed to accurately predict the pressure loss and provide another option for design and scale-up. Roughness of the lab-scale pipe

and retaining apparatus was identified as a critical parameter in de-convoluting the experimental results and matching the results with CFD. Residence time with various geometrical configurations was also explored computationally.

Finally, multiphase experimental results were fit with a new correlation based on the theory of multiphase pipe flow presented by Lockhart & Martinelli [2]. The onset of entrainment point inside the mixer channel was postulated as the critical parameter in determining the change multiphase flow regime inside the mixer element and the correlation of Ishii & Gromles provided the best fit to the experimental data [3]. Multi-phase CFD simulations with constant droplet size and reflecting wall boundary condition showed good agreement with the experimental data up to $Re_L < 84$. At higher liquid Reynolds numbers, the simplified CFD approach was not able to accurately capture the pressure loss above $Re_G = 110{,}000$, likely due to more complex interaction between surface films and droplets.

This work as provided several correlations which are broadly generalizable and useful for predicting pressure losses in static mixing geometries at high Reynolds numbers. The results will be useful for correlating with mass transfer to provide more robust predictions of co-current absorption in corrugated plate geometries.

CHAPTER 1

Introduction and Background

This chapter provides an overview of gas treating technology in the context of natural gas and biogas operations. Context for the research is provided and drawbacks of existing traditional treating methods are explained. Finally, a case for in-line contactors is provided along with potential applications and ranges of applicability in industry. Current shortfalls in design data and generalizable models for the design engineer are explored in the context of the research in this dissertation.

1.1   Motivation and Purpose

The global demand for energy has continued to increase at a near-exponential rate. With rising infrastructure in previously under-developed nations, the demand for fossil energy will likely continue its meteoric rise. Concerns over the changing climate and anthropogenic sources of atmospheric pollution and warming gases have led to an increased focus on natural gas and renewable gas resources (such as biogas) to meet some of this global energy demand [4]. Electricity generated from methane gas emits half of the CO_2 of electricity generated by coal [5]. Much of the significant drop in carbon intensity across the United States has been driven by increased adoption of gas powered electricity generation [6].

With increased natural gas consumption comes the need for infrastructure to handle the natural gas or biogas and effectively deliver the product to the consumer. Gas produced from reservoirs or from biological sources often contains a variety of species besides methane. The impact of these other species can range from nuisance, such as nitrogen, to dangerous, as in the

case of H$_2$S. Removal of these compounds or "upgrading" of the gas is essential. Figure 1.1

shows a simplified flow diagram for natural gas upgrading from wellhead to sales pipeline.

Figure 1.2 shows a typical biogas upgrading flow diagram for a gas-to-grid plant.
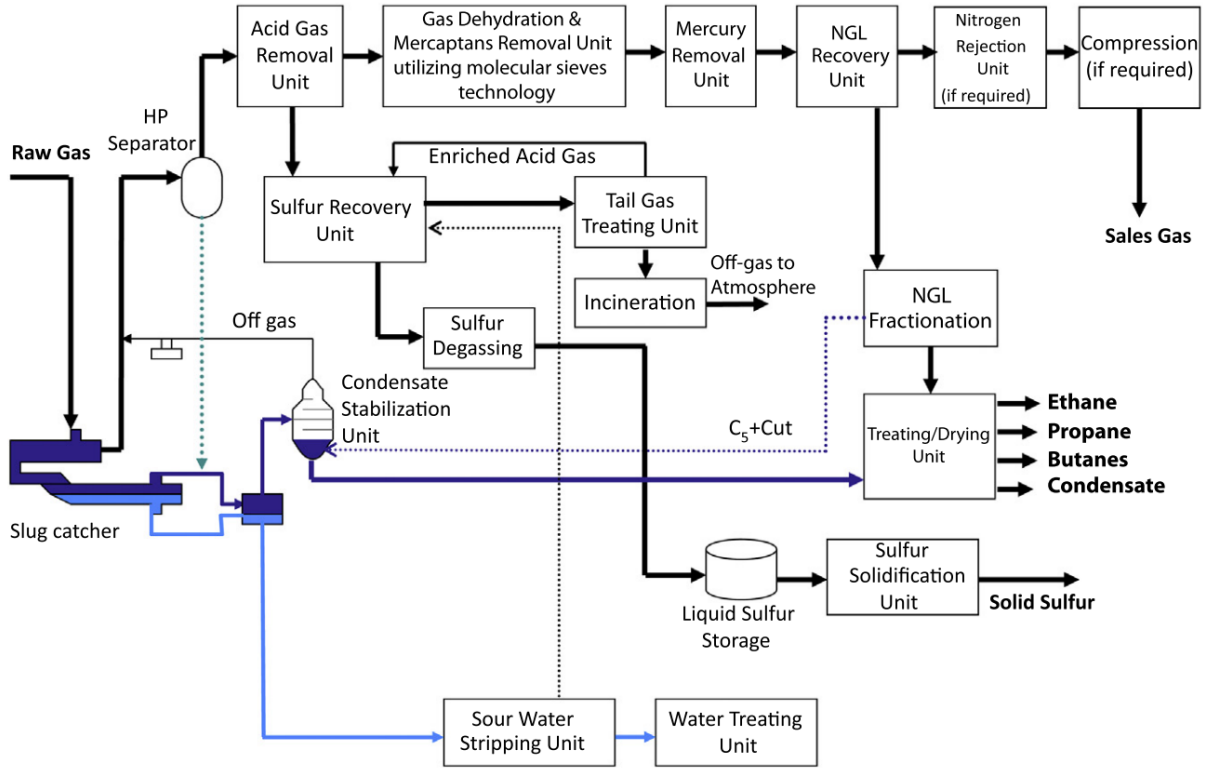
Figure 1.1. Overview of natural gas treatment process from well to sale. Reproduced from Mokhatab et al. [4]
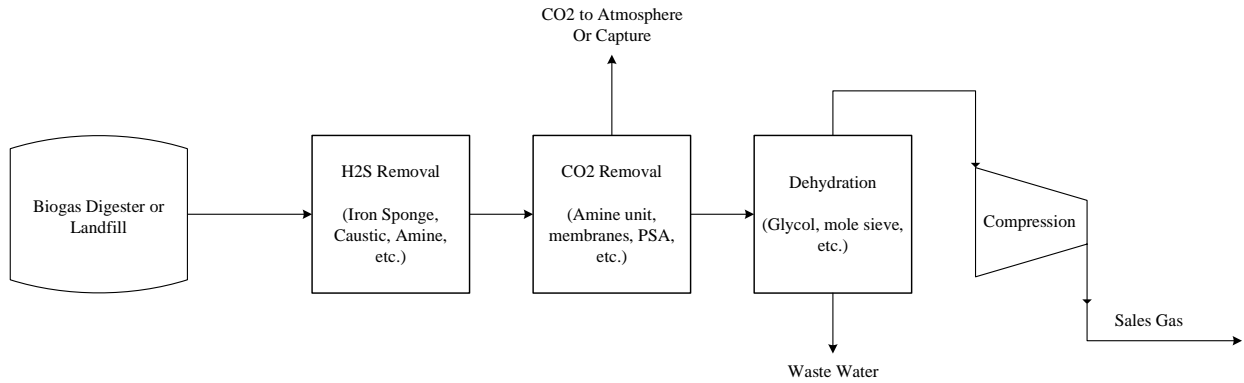
Figure 1.2. Basic biogas upgrading scheme for gas-to-grid

Regardless of the upgrading scheme, to remove unwanted species from the gas, liquid absorption is a commonplace unit operation. Gas sweetening, for example, involves the removal of acid gases (CO_2 and H_2S), typically utilizing an alkaline solvent such as amine or caustic which can react with the highly soluble acid gas species [7–9]. Additionally, oxygenates such as methanol or ketones may be removed utilizing water as a physical absorption solvent [10,11]. Dehydration of gas to reach the U.S. pipeline specification of 7 lb_m/MMSCF can be accomplished by contacting with glycol which has a high affinity for water vapor [4,12]. Absorption of heavy hydrocarbons in liquid oil can be used for lowering the hydrocarbon dew point of wet gas [13] or for removal of nitrogen [14].

The process of selectively removing species from gas using liquid is accomplished through gas-liquid mass transfer, often accompanied by a reaction in the liquid phase. Partial pressure, temperature, and physical solubility of species in the liquid determine how rapidly the species will be absorbed by the liquid. Traditionally, this process is accomplished in a contactor tower or column in which the gas flows vertically upward through the column and the liquid flows vertically downward.

3

The linear driving force model of mass transfer can be expressed in a simplified form as Equation 1.1.

$$N = k_G a(p - p_i) = k_L a(C^{eq} - C^b) \qquad\qquad 1.1$$

Where N is the mass flux across the interface between liquid and gas. The gas phase resistance (L.H.S. of Equation 1.1) is expressed in terms of the partial pressure of the species in the bulk gas phase (p) and at the interface (p_i). Similarly, the liquid phase mass transfer resistance (R.H.S. of Equation 1.1) is a function of the equilibrium concentration of the species at the interface (C^{eq}) and in the bulk liquid (C^b). The mass transfer coefficients in the gas-phase (k_G) and liquid phase (k_L). Finally, a is the interfacial area concentration between the gas and liquid. In many cases, the gas phase resistance is negligible and therefore the quantity $k_L a$ is the most controlling factor in the performance of gas liquid absorption. Table 1.1 shows a comparison between various gas-liquid mass transfer techniques and equipment.

Table 1.1. Comparison of conventional gas-liquid mass transfer methods and equipment [15]

Method	Examples	$k_L a$ (1/s)	Advantages	Disadvantages
Sieve Tray Column	• Sour gas caustic scrubbers • Glycol dehydration units • Sulfolane extraction	0.01 - 0.4	• Counter-current • Established technology • Good when more than 4 NTS are needed	• Large diameter tower required • Flooding possible • Solvent carry-over
Packed Column – Counter-current	• Amine Treating • Glycol dehydration units	0.0004-0.07	• Counter-current • High interfacial area • Established technology • Good when more than 4 NTS are needed	• Tendency to entrain and carry-over • Moderately large tower diameter required
Tube/Pipe Reactor	• Low residence time H_2S scrubbing	0.005 - 0.7	• Very simple operation • Low cost/high reliability	• Hard to control • Poor turn-down performance • Very hard to predict
Inline Static Mixing – Co-current	• Oxygenate scrubbing • Amine treating (some cases) • Low residence time extractions • Glycol dehydration units	0.005 – 1.5	• High mass transfer performance • High turndown ratio • Low cost/Small footprint • Good when <4 NTS needed	• Co-current • Higher pressure losses • Fewer predictive models available

As noted in Table 1.1, column-type treating systems (structured packing, sieve trays) have been very well established in industry for robust treatment of gas with liquid solvents. This is especially the case when the number of theoretical stages (NTS) is greater than four. Despite widespread usage, partly due to the massive amount of data available, columns can suffer from carry-over of solvent and have notoriously narrow operability ranges. Tubular reactors are similarly fraught with their own set of issues, namely lack of good predictive methods and unpredictable operation during transient flow.

Inline static mixing presents a good alternative to conventional methods. Static mixers generate very high interfacial area and are generally much more tolerant of turn-down conditions. While the options for liquid-liquid static mixers are broad, gas-liquid contacting presents unique physical challenges and few industrially available mixers are rated for this service. The SMV-style mixer is considered the industry standard for gas-continuous service with liquid (cf. Figure 1.3). Despite being the industry standard option for gas-liquid mass transfer in co-current in-line scenarios, there is a lack of data and correlations that extend into the normal range of operation for most gas transmission and processing situations. Indeed, the studies available in the open literature only provide data and extend predictions up to $Re_G \cong$ 50,000 [16–19]. By contrast, most gas lines operate between $10^5 < Re_G < 10^7$ [4]. Multiphase flow in these mixers has also not been thoroughly evaluated.

Basic Unit Operation	Fluids	Application	Mixer
Narrow residence time distribution (laminar regime)	Highly viscous fluids	Plug flow laminar	SMX/SMXL
Laminar flow heat transfer	Highly viscous heat sensitive	Heat transfer with viscous liquids	SMXL/SMR
Laminar flow mixing/blending	Highly viscous miscible	Blending laminar liquids	SMX/SMXL
	High & low viscosity, miscible	Mixing high/low viscosity liquids	SMX
Laminar flow dispersing	High & low viscosity immiscible	Dispersing high/low viscosity liquids	SMX
Turbulent flow dispersing	Liquid as continuous phase with gas	Mass transfer for dissolution of gases	SMV KMS
		Mass transfer with chemical reaction	SMV KMS
	Gas as continuous phase with liquid	Mass transfer for absorption	SMV
		Mass transfer with chemical reaction	SMV
		Vaporization	SMV
	Low viscosity, immiscible liquids	Dispersing, emulsifying	SMV KMS
		Mass transfer for extraction, washing	SMV KMS
		Mass transfer with chemical reaction	SMV KMS
Turbulent flow mixing / blending	Low viscosity, miscible	Blending low viscosity fluids	KVM SMV HEV KMS
Narrow residence time distribution	Low to medium viscosity fluid	Plug flow low viscosity fluids	SMV/SMVP KMS

Figure 1.3. Static mixer selection matrix. Reproduced from Paul et al. [1]

6

Based on this deficiency in the literature, this dissertation focuses on providing practical data and correlations for higher Reynolds numbers under single- and multi-phase conditions.

1.2   *Dissertation Organization*

This dissertation is organized into five chapters. Chapter 2 addresses single-phase flow through a single SMV-style mixer utilizing experimental data and CFD numerical simunulations. Chapter 3 extends this work to multiple mixers in various configurations. Chapter 4 provides experimental data and a correlation for multiphase flow with gas continuous phase through SMV-style mixers along with a CFD workflow. Finally, Chapter 5 provides overall conclusions and recommendations for future work.

CHAPTER 2

A New Correlation for Single-Phase Pressure Loss through SMV Static Mixers at High Reynolds Numbers[1]

Abstract

Robust, scalable correlations for pressure loss across corrugated (SMV-style) static mixers at high Reynolds (Re) numbers are currently lacking. To address this, results from an experimental and computational fluid dynamics (CFD) based study involving a single SMV mixing element for Re in the range of 8,000 – 250,000 are reported. The investigated scenarios encompassed three different pipe diameters and variations in the wall roughness.

The equivalent sand grain roughness was first estimated from measurements in an empty pipe and provided as an input to the CFD model. The agreement between the CFD predictions and measurements ascertained the validity of the roughness estimate. When the mixing element was absent, roughness contributed about 70-90% of the pressure losses in the rough stainless steel pipes and up to 7% of the losses in the smooth PVC pipe.

A capillary model based semi-analytical correlation was developed to generalize the pressure loss characteristics when the mixing element was present. The proposed correlation captured both current and historical pressure loss measurements with an improved accuracy over currently available correlations. Even when with the mixing element present, about 60% of the pressure losses were attributed to the inclusion of wall roughness.

2.1   Introduction

Static mixing technologies have played a substantial role in process intensification efforts over the past century. These fundamentally simple devices harness the kinetic energy of a flowing fluid to effectively mix and blend fluids without the need for stirred vessels or external energy sources. Advantages of low cost, low maintenance, and low power requirements have resulted in static mixers becoming a common tool for both single and multiphase mixing applications [20].

With the recent trend towards process intensification, the overall efficiency and small form-factor associated with static mixing reactors has renewed interest in this area. These types of reactors excel in absorption or fast-reaction scenarios that are constrained by low residence times, and where interfacial diffusion resistance is reasonably low, such as a high pressure, gas-continuous processes [21]. However, since static mixer geometries result in complex flow fields it is has been challenging to develop accurate and robust correlations that characterize their performance under dynamic process conditions. It is this lack of knowledge that has led to large amounts of research regarding mixing encompassing both laminar and turbulent regimes [22–26]. Understanding the dynamic pressure loss characteristics in these reactors is a critical first-step towards their design, optimization, and scale-up since heterogeneous heat and mass transfer characteristics is known to correlate strongly with pressure loss [27]. At high velocities, when liquid phase resistance to mass transfer is controlling, co-current operation is shown to result in higher mass transfer rates than operating in a counter-current mode [27]. During co-current operation, corrugated mixing elements, like the Sulzer SMV mixer can greatly enhance the turbulent mixing of both liquid-liquid and gas-liquid streams thereby reducing the required pipe

lengths for mixing or extraction applications. This corrugated plate type mixer is comprised of
channels that split the fluid prior to forcing it back together in cross-flow as shown in Figure 2.1.
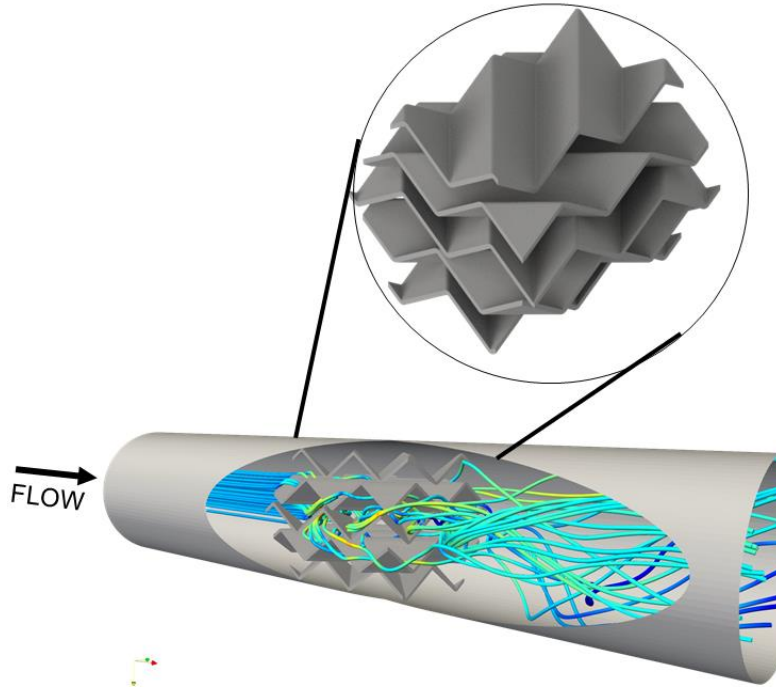
Figure 2.1 Flow in a corrugated plate type mixer

This same type of contacting scheme has been used for a variety of structured packing
options for packed tower systems [27]. This type of a stacked corrugated plate design has been
shown to yield high mass transfer rates while minimizing pressure losses and liquid holdup
[28,29] .

There are three common functional forms employed to quantify the pressure loss
(ΔP) across corrugated static mixers:

$$Z = \Delta P_{mixer}/\Delta P_{empty\ pipe} \qquad\qquad 2.1$$

The Z-factor [1] in Equation 2.1 is defined as the pressure loss across the mixer to that in an empty pipe. Z values generally range from $100 - 200$ in the turbulent regime for corrugated plate mixers.

A second method expresses ΔP in terms of the square of the fluid velocity (v) as [19]:

$$\Delta P = C_1 \times v^2 \qquad\qquad 2.2$$

Where C_1 in Equation 2.2 is a constant whose value is in the range 105 +/- 5 [19].

The third functional form is a Blasius type correlation where the fanning friction factor (f) is computed as a function of Reynolds number (Re) as [17,18]:

$$\frac{f}{2} = \frac{\Delta PD}{\rho u_0{}^2 L} = C_2 + \frac{C_3}{Re^{C_4}} \qquad\qquad 2.3$$

Where ρ is the velocity of the fluid and appropriate length scales: such as length of the static mixer element (L) and pipe diameter (D) are employed in the calculation. C_2, C_3 and C_4 are constants that are empirically determined.

A more sophisticated, semi-analytical model for pressure drop in corrugated mixers was presented and validated for water through 40-80 mm mixer elements by Paglianti et al. (2013) [16]. The model hypothesized that the total pressure drop across a corrugated element is the sum of the friction pressure drop and the interfacial pressure loss due to inlet/outlet effects. The correlation from [16] is expressed as:

$$\Delta P = \frac{\pi d_H L}{A \sin(\beta)} \frac{\zeta \rho u_s^2}{2} + 4\zeta \frac{Le_{inlet} + Le_{outlet}}{d_H} \frac{\rho u_s^2}{2} \qquad\qquad 2.4$$

Where β is the corrugation angle relative to the flow direction and Le_{inlet} and Le_{outlet} are the interfacial lengths that account for pressure losses at the interface between multiple elements. The authors did not demonstrate how this value was calculated in practice, and thus the values given in the paper were assumed to be generally applicable. The term ζ is the effective friction factor of the materials and was taken from previous work by the authors [30].

Building on prior work [31], a model was presented which accounts for four separate cases: (1) a single element with a L/D > 1; (2) multiple elements with L/D > 1; (3) a single element with L/D < 0.56; (4) multiple elements with L/D < 0.56 . It was noted that fluid bypass occurs when an individual element is less than 0.56 pipe diameters in length.

A comparison of three correlations (Equations 2.3 and 2.4) for the geometric static mixer parameters of interest in this study is shown in Figure 2.2. The parameters used in our calculations were: L , D, density, velocity, and mixer void fraction taken from Table 2.2 and experimental process conditions. β was set equal to 45 degrees, and ζ was calculated to be 0.01135 using the correlation provided by Paglianti et al [16].
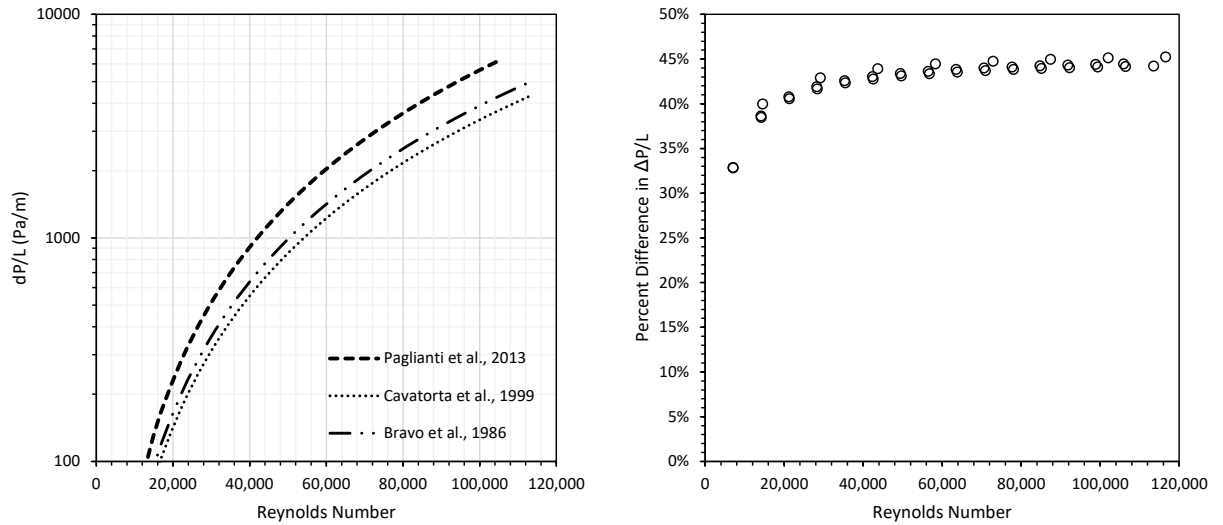
Figure 2.2. Pressure drop predicted by different correlations for a single 2-inch diameter corrugated element (left) and relative difference between Paglianti et al. (2013) and Cavatorta et al. (1999) (right)

What is clear from Figure 2.2 is that despite the large amount of interest in static mixer reactors with liquids/high pressure gases as the working fluid, a robust correlation that is applicable at higher Reynolds number conditions (10,000 – 100,000) is currently lacking. Second, the role played by pipe and mixer element surface roughness characteristics has not been explored in the context of a scaling lab data to larger diameter pipes and mixers. In order to fill this void, a comprehensive experimental and simulation-based study of the pressure loss behavior of a corrugated static mixer was undertaken to:

(1) Measure and quantify the role of sand-grain surface roughness at these conditions.

(2) Provide a more accurate, robust, and scalable pressure loss correlation.

(3) Evaluate the efficacy of computational fluid dynamics (CFD) simulations as a pressure loss prediction and scale-up tool.

2.2 Methods

2.2.1 Measurements

2.2.1.1 Experimental System

To measure the experimental pressure drop across the lab scale mixing elements, two flow systems were constructed. The first system was designed to operate with compressed air up to a pressure of 120 psig. Air flow (at 110 psig) was supplied by a 150 HP air compressor with a 1000 gal holding vessel. All process piping was composed of schedule 40 stainless steel in 1-inch nominal sizing. A pipe run of 24 inches was allowed after the inlet valve to allow the flow to fully develop prior to measuring the flowrate using a cylindrical averaging differential pressure probe. The differential pressure gauges for the flowmeter and measurement section were acquired from Alicat Scientific, Inc. (Tuscon, AZ, USA) and have a calibrated accuracy of 0.2% across the entire range of Reynolds numbers. A computer data acquisition system was used to log the data from the differential pressure meters. The system was capable of producing maximum velocities of around 30 m/s in the 1-inch pipe configuration (Re of 440,000). The piping configuration was constructed to allow the measurement section to be switched to a 2-inch nominal pipe run for measurements in a larger diameter. For all tests, a pipe run of at least 10 pipe diameters was placed before the measurement section to allow for flow development. A 1/8 inch retaining stud was fixed in the pipe to hold the mixing elements in place inside the pipe during testing.

To carry out testing in a 4-inch diameter pipe, a second experimental system was constructed to operate at near ambient pressure conditions with a 4-inch diameter PVC pipe conduit. A compressed air amplifier (Brauer Limited, Milton Keynes, UK) was used to boost

compressor air to a max flowrate of 615 CFM (Re of 275,000) at near ambient conditions. The flowrate was monitored using a cylindrical averaging differential pressure probe and a differential pressure gauge manufactured by Dwyer (Michigan City, IN, USA) with an accuracy of 0.5% across the measurement range.

Corrugated mixing elements with five plates and a corrugation angle of 45 degrees relative to the pipe axis were fabricated in for use in the 1-inch, 2-inch, and 4-inch diameter pipes. The corrugated mixer was 3D-printed from ABS material using the same CAD file utilized for the CFD simulations. A flow diagram of the first experimental set up employed to make pressure drop measurements is shown in Figure 2.3.
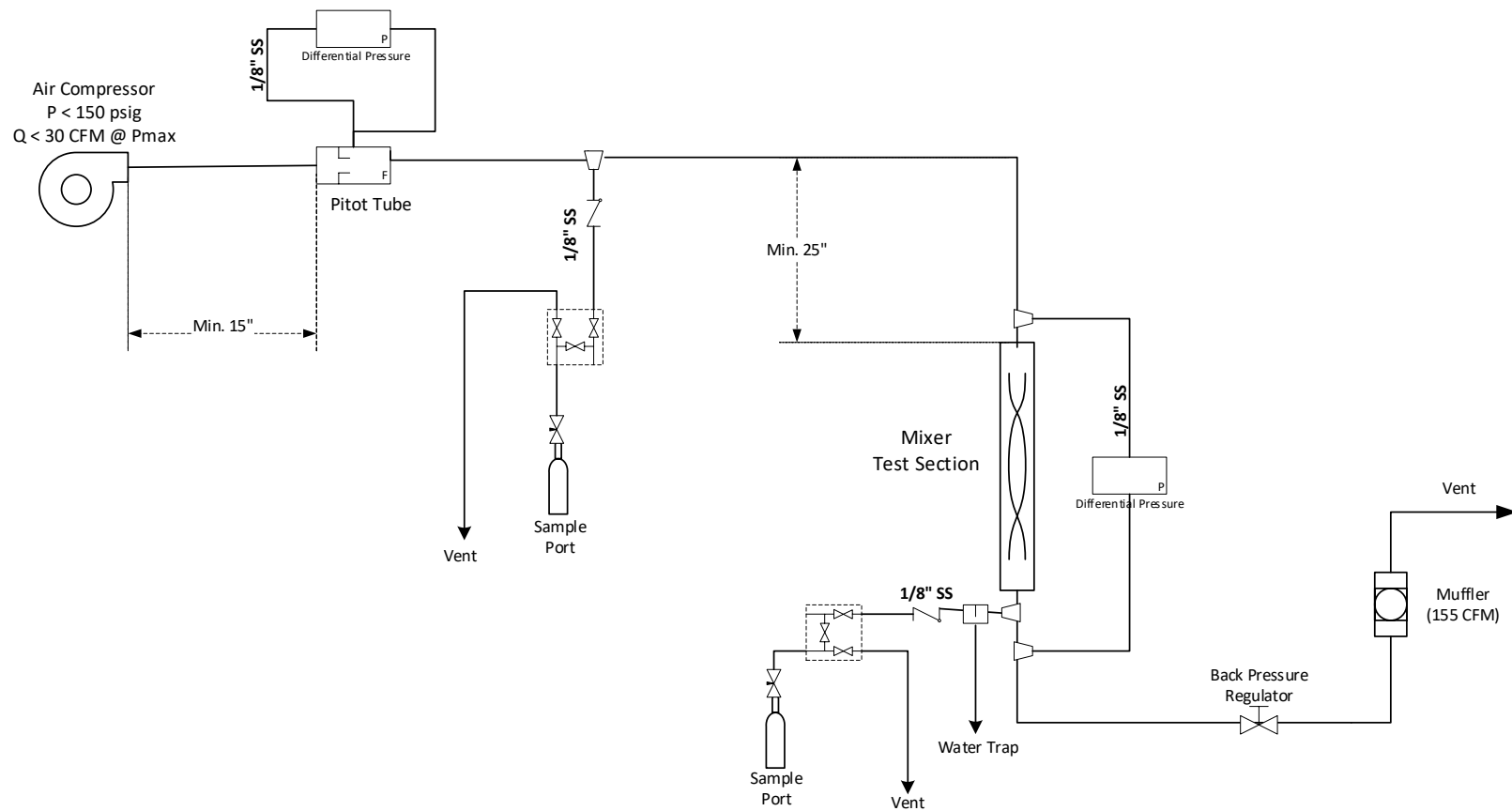
Figure 2.3. Process flow diagram of first experimental system

In order to conduct a pressure loss test in both systems, the flowrate was incrementally increased to the maximum flowrate over a period of approximately 20 minutes for each test. This method allowed for enough data acquisition to construct a curve of flow versus differential pressure. Data points were collected every 230 ms via the data acquisition system. Once steady state conditions were obtained, the average differential pressure loss data was then calculated across several seconds of the steady-state condition.

Prior to carrying out the test with the static mixers present along the flow path, the experimental configuration along with the pressure gauges were assessed for their measurement accuracies by estimating the standard error associated with the pressure drop measurements. Pressure drop data associated flow in an empty pipe was determined by gradually varying the flow rates. At each flow rate, the pressure drop data was sampled across a 20-minute time period (after steady state was obtained) to obtain a standard error that was statistically invariant. The systematic errors were less than 2% above Reynolds numbers of 25,000.

2.2.1.2 Relative Roughness Estimation in an Empty Pipe

Since the focus of this study was to assess the pressure loss effects solely due to the corrugated static mixing elements and the pipe housing directly around the mixer, it was important to subtract the extra empty pipe pressure losses from the measurements. The pressure losses of the empty pipe housings were measured by continuously logging the flowrate and differential pressure across the test section using a computer with data acquisition software. By fitting a line to this averaged raw data, the fanning friction factor (f) could be directly determined using Equation 2.5.

$$\frac{1}{\sqrt{f}} = -4.0 \log_{10} \left(\frac{\frac{K_s}{D}}{3.7} + \frac{1.255}{Re\sqrt{f}} \right) \qquad\qquad 2.5$$

The result of this procedure provided the effective relative roughness for each pipe

housing and is summarized in Table 2.1.

Table 2.1. Results of empty pipe experiment and fit with Colebrook-White equation

Nominal Pipe Diameter (inch)	Reynolds Number Range	Calc'd Relative Roughness
1	15,000 - 150,000	0.17379
2	5,000 - 100,000	0.11407
4	30,000 - 130,000	0.00010

The baseline (empty pipe) pressure loss at each operating condition (Reynolds number)

could now be estimated by computing the friction factor using Equation 2.5 and estimating ΔP

using Equation 2.3. A comparison of the modeled pressure loss (empirical) using Equation 2.3

and 2.5 and actual measurements are shown in Figure 2.4 to demonstrate the validity of our relative

roughness estimation method.
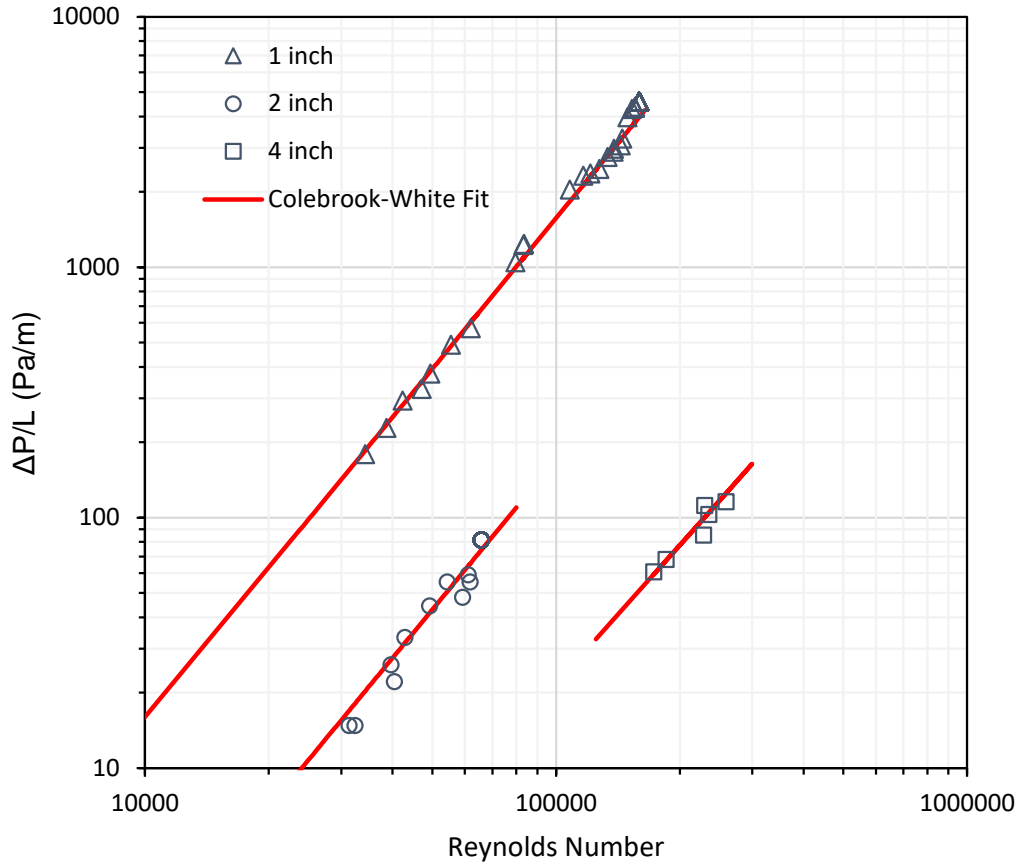
Figure 2.4. Experimental pressure loss measurements and calculated pressure loss resulting from the fit of the Colebrook-White equation (Eq. 5) for 1-inch, 2-inch, and 4-inch empty pipes

When carrying out measurements with the static mixer, this baseline pressure loss was subtracted from the measured total pressure to delineate losses attributed to the mixing element and immediate surrounding pipe housing alone. Trials were conducted at the three pipe diameters for Re ranging from 10,000 – 200,000.

2.2.2 Computational Fluid Dynamics Simulations

2.2.2.1 Rough Pipe Simulations

In order to evaluate the ability of CFD simulations to account for rough pipe walls as well as determine the optimal first cell height at the pipe wall, several empty pipe meshes were constructed. Three meshes for each diameter were constructed, each with a different height of the first cell on the pipe wall. The meshes were constructed with Gmsh [32], which is an open-source meshing software capable of creating high-quality hexahedral mesh configurations with very minimal skew. Figure 2.5 shows a cross-sectional view of the three meshes (fine, medium, and coarse) created for the 1-inch pipe size.
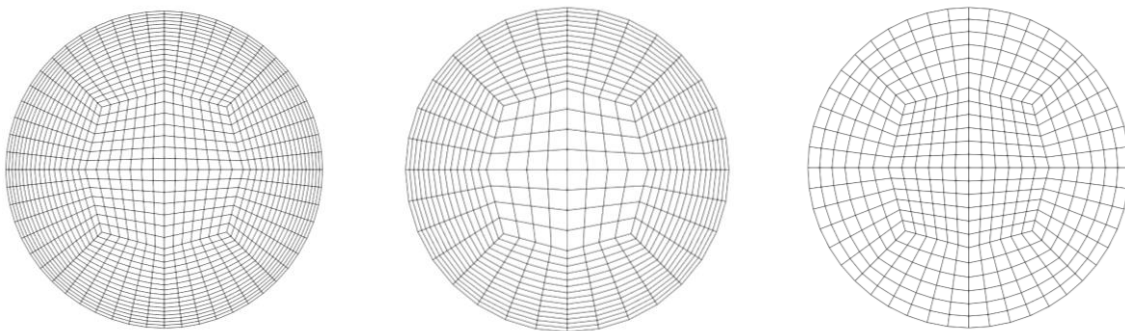
Figure 2.5. Cross-sectional view of the three empty pipe meshes. From left to right: fine, medium, coarse

Ansys Fluent (version R2019), was evaluated for its ability to predict the empty pipe pressure loss using rough wall functions. The inlet and outlet boundaries of the 10-diameter long model pipe were considered to be periodic boundaries in order to simulate fully developed flow conditions. The SIMPLEC solver was chosen due to its proven fast, robust convergence [33]. Second-order upwind schemes were utilized for the flow and turbulence variables. Each simulation was conducted until the residuals achieved a convergence criteria of 1×10^{-5}. The

near-wall region was modeled using the standard rough-wall implementation in Ansys Fluent, described in the following section. The realizable $k - \epsilon$ model was chosen for the turbulence fields due to its superior formulation for the turbulent viscosity and enhanced handling of dissipation near boundary layers [34]. At the end of the simulation, the steady-state isothermal pressure gradient was extracted. The conditions for the numerical simulations were the same as the experimental work with the working fluid modeled as an incompressible fluid with the same density of compressed air at 100 psig and 70 °F.

2.2.2.2 Roughness Implementation in Ansys Fluent

Ansys Fluent requires the user to specify the sand-grain roughness (K_s) (estimated in Table 2.1) and a roughness constant (C_s). The sand-grain roughness of a surface is implemented in Ansys Fluent by shifting the law-of-the-wall mean velocity distribution by a factor (ΔB) based on the specified surface roughness. The shifting function (ΔB) is determined according to the boundary layer corrections provided by Cebeci and Bradshaw [35].

The hydrodynamically smooth treatment is applied when $K_s^+ < 2.25$, meaning no correction is applied to the near wall functions. In the transitional regime $(2.25 < K_s^+ \leq 90)$, Equation 2.6 is applied to determine the functional correction.

$$\Delta B = \frac{1}{\kappa} ln \left[\frac{K_s^+ - 2.25}{87.75} + C_s K_s^+ \right] \times sin\big(0.4258 \, (ln(K_s^+ - 0.811))\big)$$

2.6

When $K_s^+ > 90$ the shift parameter is calculated by Equation 2.7.

$$\Delta B = \frac{1}{\kappa} ln[1 + C_s K_s^+]$$

2.7

In Equations 2.6 and 2.7, the roughness constant C_s was kept at the default value of 0.5 for all simulations. The dimensionless roughness height (K_s^+) was estimated from the sand grain roughness in Table 2.1 as:

$$K_s^+ = \frac{K_s C_\mu^{\frac{1}{4}} k^{\frac{1}{2}}}{\nu}$$

2.8

Where C_μ is an empirical model constant, k is the turbulent kinetic energy and ν is the turbulent viscosity. The definition of y^+ is given by Equation 2.9.

$$y^+ = \frac{C_\mu^{\frac{1}{4}} k^{\frac{1}{2}} y}{\nu}$$

2.9

Once the shift parameter is determined, the non-dimensional cell wall distance y^+ can be determined by Equation 2.11 in terms of the shift in the value of the dimensionless wall velocity (defined by Equation 2.10).

$$u^+ = \frac{u}{\sqrt{\frac{\tau_w}{\rho}}}$$

2.10

$$u^+ = \frac{1}{\kappa} ln(Ey^+) - \Delta B$$

2.11

2.2.2.3 Mixer Mesh Generation and Evaluation

The static mixer 3D CAD geometries were constructed from the fabricator models in order to have the most accurate similarity between the CFD and experiment. Each mixer was composed of five corrugated plates arranged at 45 degrees with the flow axis. The corrugation bend angle was 109 degrees. The mixer dimensions were ssuch that they fit tightly into the nominal pipe size for which they were designed. Figure 2.6 shows a drawing of one of the corrugated mixers from different view points.
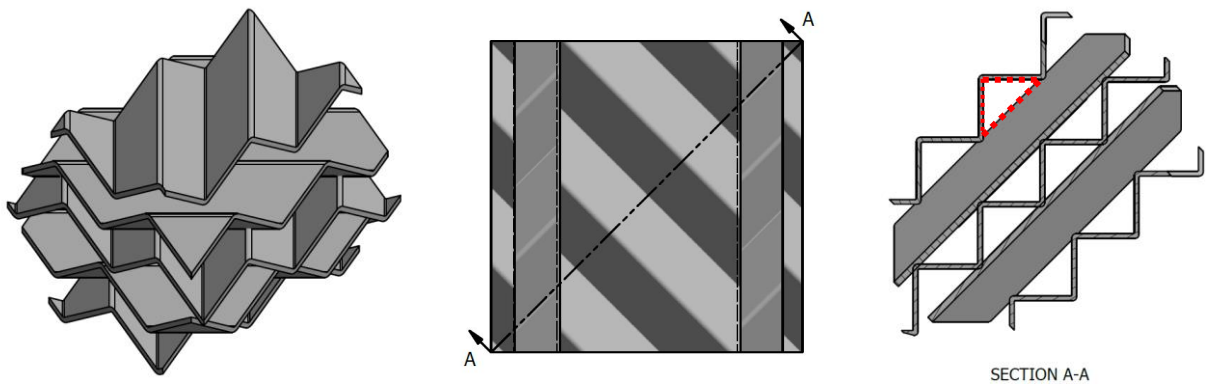
Figure 2.6. 3D CAD rendering of the corrugated mixer used for CFD simulations. The red dashed lines denote the perimeter (P) of one channel used for determination of the hydraulic diameter

Each mixer can be characterized by key variables such as the void fraction (ϵ), the tortuosity (τ), and the hydraulic diameter of a channel in the mixer. The void fraction is the mixer material volume divided by the total volume occupied by the mixer element. The hydraulic diameter (D_c) of the mixer channel can be estimated by calculating the diameter of an

equivalent circle with the same perimeter ($\mathcal{P}$, depicted as the red dashed lines in Figure 2.6) as the mixer according to Equation 2.12.

$$D_c = \frac{\mathcal{P}}{\pi}$$

2.12

The tortuosity is defined as the length of a theoretical flow-path through the mixer divided by the actual distance traveled in the primary direction of flow [36]. Recently, Zare & Hashemabadi [37] showed that the tortuosity could be accurately estimated by taking the average streamline length from a CFD simulation and comparing to the distance traveled in the primary flow direction. Applying this same concept, the post-processed data from the simulations for all three mixer sizes was utilized to calculate the tortuosity of each mixer. A total of 10,000 streamlines were calculated based on the flow field through the mixer and this was used to extract the tortuosity for each streamline. From this, the overall average tortuosity of the mixer was calculated. The sand-grain roughness (Ks) for the mixer material was used as an input to the CFD simulations and was based off standard roughness values for the materials of construction provided by the fabricator. Table 2.2 shows the key variables for each mixer element used in the experimental and CFD work.

Table 2.2. Experimental and CFD Model Mixer Element Dimensions

D (in)	L/D	ε	τ	D_c (in)	K_s (micron)
1	1	0.756	1.457	0.118	10
2	1	0.879	1.428	0.315	10
4	1	0.879	1.373	0.787	100

Given the complex geometry of the corrugated mixer elements, a grid refinement study was conducted to evaluate the impact on pressure loss prediction. Two meshes of each size of

24

mixer were created using the snappyHexMesh (a utility included in OpenFOAM ver. 1906). The mixing elements were situated in the center of the empty pipe housing mesh, which was 10 pipe diameters in length. The finest level mesh from the empty pipe simulations was chosen as the pipe housing. The first mesh resolution was chosen such that the average dimensionless wall distance of the first cell (y^+) (cf. Equation 2.9) was below 30 to justify the use of enhanced wall functions. The coarser meshes were created by lowering the refinement level by one in all locations of the mesh. Simulations were conducted in each mesh refinement at the highest experimental Reynolds number to evaluate impact on pressure loss.

Table 2.3 shows the percent change in pressure loss calculated by increasing the refinement level of the mesh. Based on the results of the grid refinement study, the most refined (fine) mixer mesh was chosen at all diameters in order to minimize the impact on the simulation results.

Table 2.3. Results of grid convergence simulations

Diameter (inch)	No. of Mesh Elements			$\Delta P/L$ (Pa/m)			%Δ, Medium-Fine
	Coarse	Medium	Fine	Coarse	Medium	Fine	
1	206,478	562,024	770,967	262,435	223,922	224,552	0.3%
2	764,284	1,495,442	2,570,634	15,287	14,567	13,794	-5.6%
4	1,356,201	2,312,566	4,075,483	16,325	15,295	14,369	-6.4%

2.3   Results

2.3.1   CFD Simulations of Empty Pipe

The adequacy of the mesh resolution, turbulence model and sand grain roughness provided as input to FLUENT was evaluated by carrying out empty pipe simulations and comparing the pressure drop data as a function of Reynolds number. The results are shown in Figure 2.7.
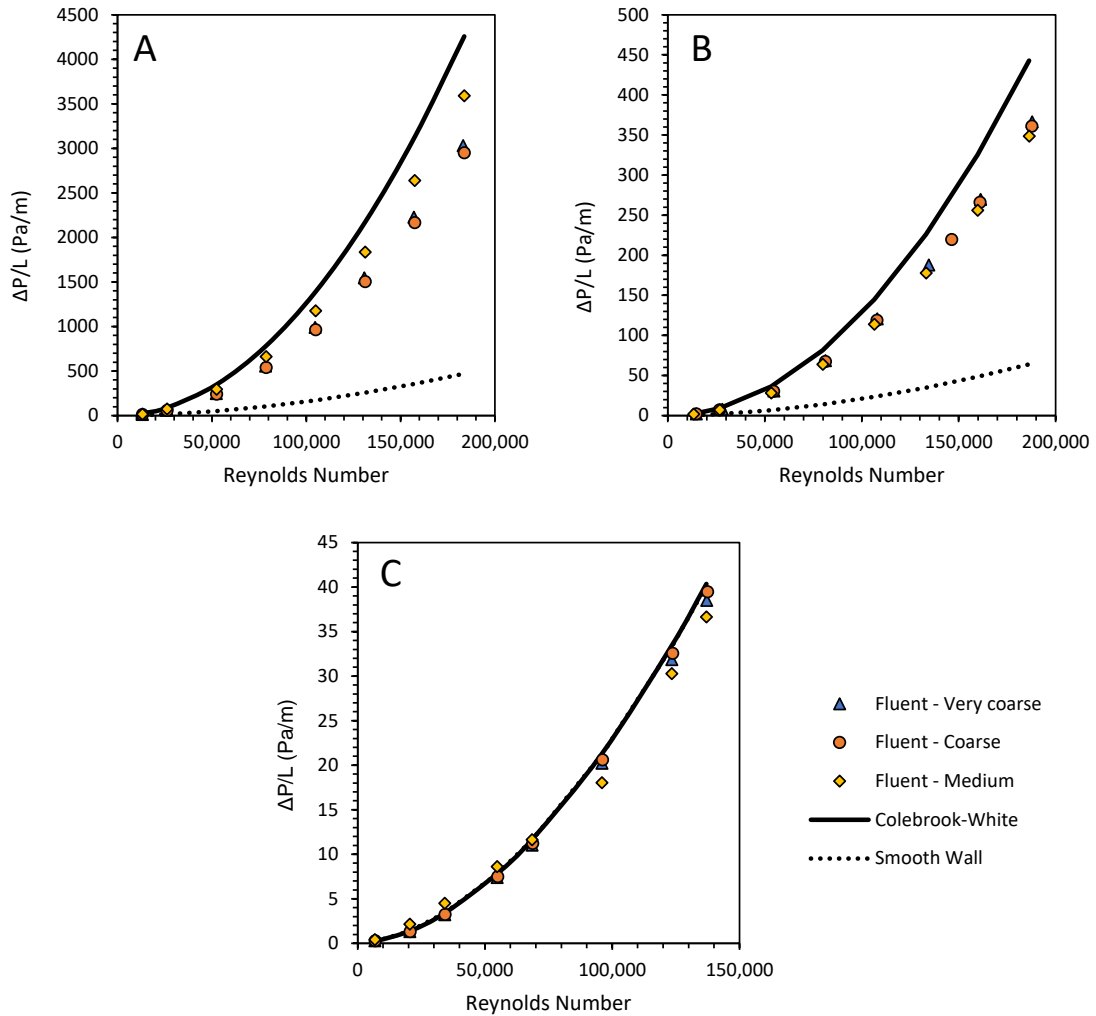
Figure 2.7. Comparison of ΔP/L for an empty-pipe versus Reynolds number (fit of experimental data versus FLUENT simulations at 3 mesh resolutions) for 1-inch (A), 2 inch (B), and 4 inch (C) pipe diameters

Good agreement is seen between the CFD predictions and measurements. The figure also shows the difference in pressure loss (i.e., ΔP/L with roughness versus ΔP/L without roughness) as a function of Reynolds number. In an empty pipe, roughness has a 70-90% contribution to the pressure loss at higher Reynolds numbers in the 1-inch and 2 inch stainless steel pipes and up to 7% contribution in the 4 inch PVC pipe that is smoother than the steel pipe (cf. Table 2.1).

2.3.2 Generalized Correlation for Pressure Loss with Static Mixer

2.3.2.1 Pressure Loss Model

In order to correlate the experimental pressure loss data, the corrugated mixer was considered to be a type of porous media possessing certain geometric characteristics. The superficial velocity through the mixer can be expressed as a function of the mean flow velocity (u_0), the tortuosity (τ) and void fraction (ϵ) of the mixer [38].

$$u_s = \frac{u_0 \tau}{\epsilon}$$

2.13

Where $\tau = \ell/L$ and ℓ is the average streamline length through the mixer of length, L. At low Reynolds numbers, the pressure loss through a porous media is proportional to the viscous forces and the kinetic energy losses of the flow. However at high Reynolds number conditions, the kinetic-energy losses dominate flow. The capillary model presented by Comiti and Renaud is useful for understanding generalized flow through a porous media [38]. By grouping the viscous pressure loss expressed by the Poiseuille equation and the kinetic terms, they arrived at a combined pressure loss expression for flow through a packed bed [39]. Unlike previous work [39,40], here we choose to employ the definition of specific surface area ($a_s = 6/D_c$) for a packed bed of regular spherical particles ($\tau = 1.44$) since the tortuosity of the single corrugated mixer is nearly identical [41]. This leads to the new formulation presented in Equation 2.14 with the primary change being the presence of the value of 72 in the numerator as opposed to 32 in previous work [39].

$$\frac{\Delta P}{\ell} = \frac{72\tau^2 \mu u_0}{\epsilon D_c^2} + \frac{2C_p \tau^3 \rho u_0^2}{D_c}$$

2.14

In Equation 2.14, C_p is the effective friction factor of the interior mixer channel wall. When the assumption is made that the roughness of the channels is on the same order of magnitude as the channel diameter itself, the friction factor of the channel can be estimated via the classic Nikuradse equation for fully turbulent flow in highly rough pipes in the natural logarithm form [42]:

$$\frac{1}{\sqrt{C_p/2}} = 2.46 \ln\left(\frac{D_c}{2e}\right) + 4.92 \qquad\qquad 2.15$$

Under the assumption that $e \cong D_c$, the friction factor for the kinetic-loss term becomes $C_p \cong 0.1936$. This assumption works well for when the channels have many flow directional changes before impacting the pipe wall. However, when the channels end at the pipe wall, as in the case of the corrugated mixer in this study, a better assumption is that $e \cong D_c/2$ which leads to $C_p \cong 0.0826$ by solving Equation 2.15 [38]. By re-arranging Equation 2.14, a combined friction factor for the mixer as a porous media may be conveniently defined:

$$f_c = \frac{D_c \Delta P \epsilon^2}{2L\rho u_0^2 \tau^3} = \frac{36\epsilon\mu}{\rho u_0 \tau D_c} + C_p \qquad\qquad 2.16$$

Noting the dimensionless first term on the right hand side of Equation 2.16, a Reynolds number for the mixer channel may be defined.

$$Re_c = \frac{\rho u_0 \tau D_c}{\epsilon\mu} \qquad\qquad 2.17$$

Finally, combining Equations 2.15, 2.16, and 2.17, the semi-analytical friction factor model for the mixer in terms of the channel geometry is expressed by Equation 2.18. Note the

similarity in the function form of this equation and the Blasius-type equation for pressure loss (cf. Equation 2.3)

$$f_c = \frac{36}{Re_c} + 0.0826 \qquad\qquad 2.18$$

This final expression is used as a semi-analytical basis for fitting the experimental data across the range of flow velocities and pipe diameters. Using this formulation, the pressure loss across a mixing element can be calculated by using Equation 2.19.

$$\frac{\Delta P}{L} = \frac{2 f_c \rho u_0^2 \tau^3}{D_c \epsilon^2} \qquad\qquad 2.19$$

The first term of Equation 2.18 represents the Darcy contributions to flow and is primarily controlling in the low Reynolds number regimes. The second constant term is attributable to the losses in high turbulence associated with the rough corrugations and dominates at high Reynolds numbers. Legrande (2002) [40] proposes that the change from Darcy flow to transitional flow occurs near $Re_c = 13$ and the fully turbulent regime starts near $Re_c = 830$.

2.3.2.2 Pressure Loss Measurement with Static Mixer

After collecting the pressure loss data using the laboratory systems described in Section 2.2.1.1, the data for one corrugated mixer for the diameters and specifications listed in Table 2.2 was processed to remove the losses due to the extra pipe lengths upstream and downstream of the mixer elements. Figure 2.8 shows the pressure loss data (not all points shown for clarity) along with previous correlations from the literature, CFD results, and the current proposed correlation of Equation 2.18 [16–18]. The existing correlations tended to under-predict the pressure losses compared to the experimental measurements in this study with the exception of the Paglianti et

al. correlation [16] for the 4-inch diameter mixer. Overall, the proposed correlation that accounts for wall roughness effects provided better agreement with the measured data and the CFD results (carried out with wall roughness). The data for the 2-inch mixer showed more scatter and less fit compared to the other sizes. The ability of the proposed correlation to fit the data over the range of Reynolds numbers indicates that it may represent a more general formulation that previously used in the literature.
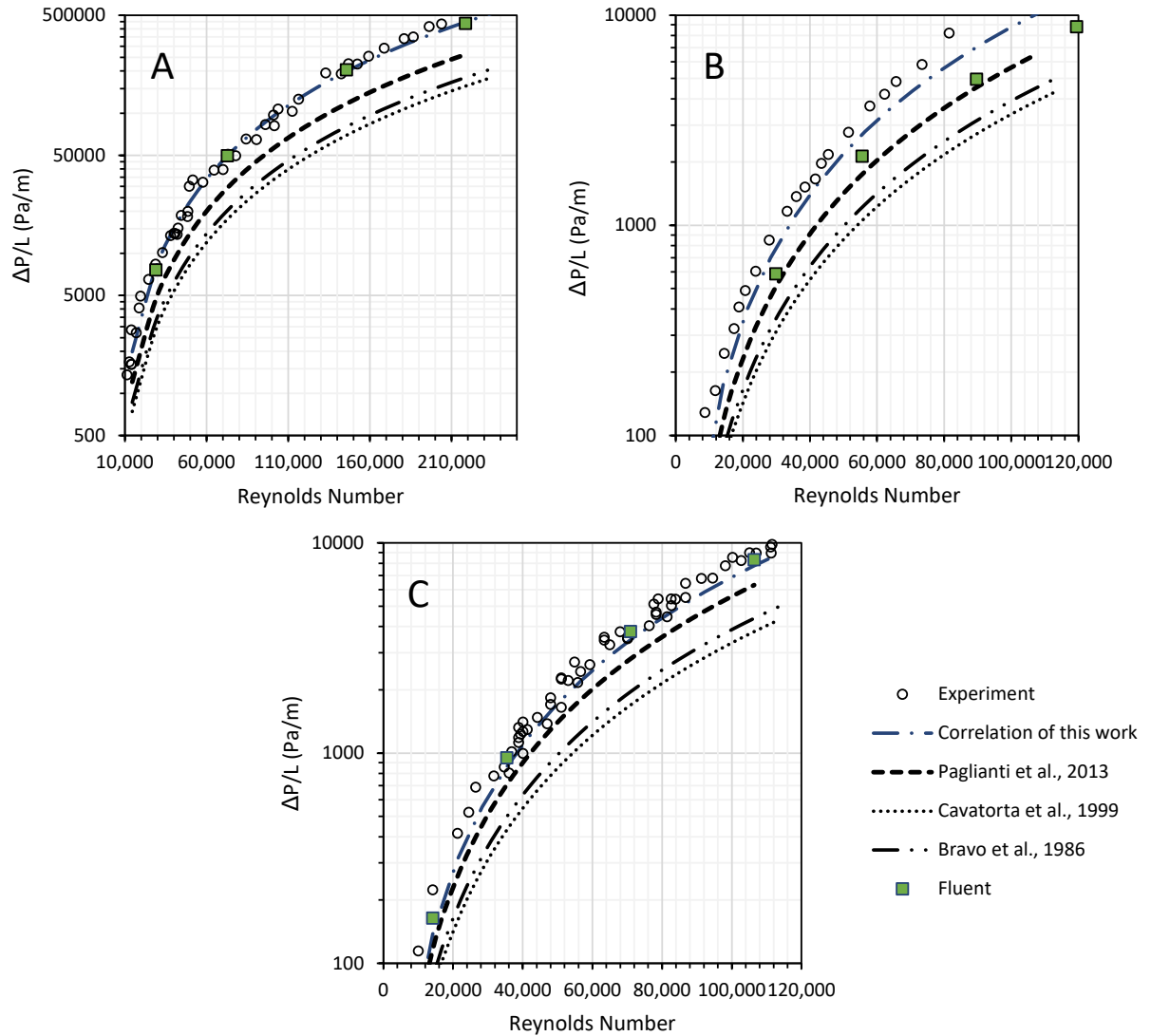
Figure 2.8. Experimental data and correlation for 1-inch, 2-inch, and 4-inch diameter mixer shown with literature correlations and CFD results

However, the CFD results obtained with Fluent were slightly lower than expected. It is suspected that this may be due to various nuisance factors that could not be accounted for in the CFD model such as irregular flows around weld locations or heterogeneous roughness in the pipe housing. To ascertain this, the sensitivity of the CFD simulations to wall roughness effects was carried out. Figure 2.9 shows the relative error in pressure loss introduced by neglecting surface roughness as a function of Reynolds number in Ansys FLUENT. In the pipe with the static

32

mixer, roughness has up to 60% contribution to the total pressure loss at these Reynolds numbers, with higher contribution in the smaller steel pipes. This finding is critical to proper scaling of lab experiments conducted in small piping where contributions of relative roughness are significant. Direct upscaling without considering these effects at lab scales can results in incorrect predictions of pressure loss in larger pipe diameters.
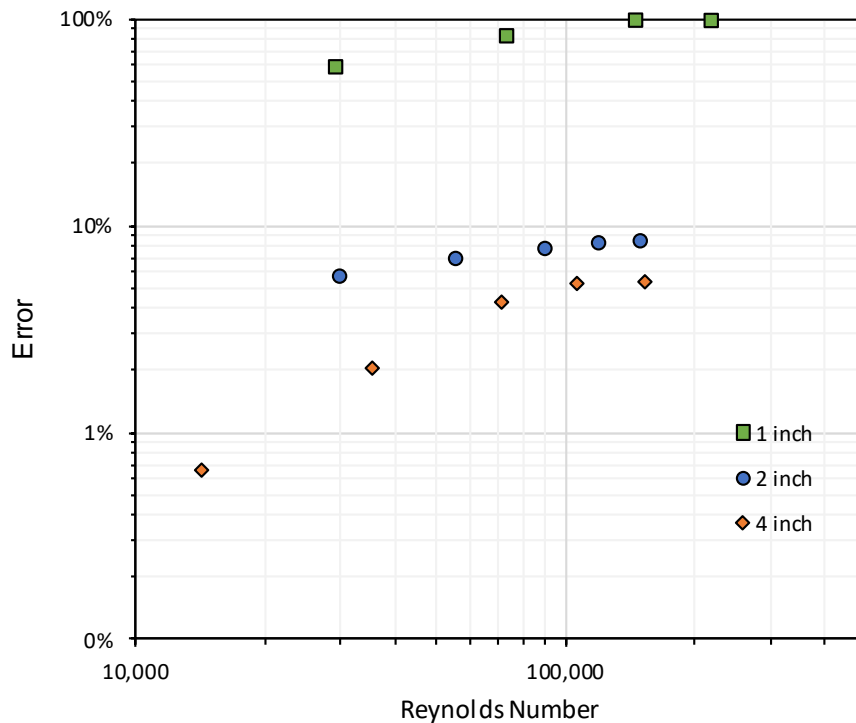
Figure 2.9. Sensitivity of pressure loss calculations to surface roughness in CFD simulation for 1-inch, 2-inch, and 4-inch

2.3.2.3 Friction Factor Estimation with Static Mixer

The pressure loss measurements were then employed to calculate a friction factor based on Equation 2.19. The data covered the range of $1500 < Re_c < 48{,}500$ which is equivalent to $8000 < Re < 2.5 \times 10^5$ in terms of the traditional Reynolds number using the pipe diameter as the characteristic dimension. As shown in Figure 2.10, the data collapsed very well into the semi-

33

analytical model of Equation 2.18. This suggests that this formulation provides a reasonable

approximation for the pressure losses through the corrugated geometry.

$$f_c = \frac{36}{Re_c} + 0.0826$$
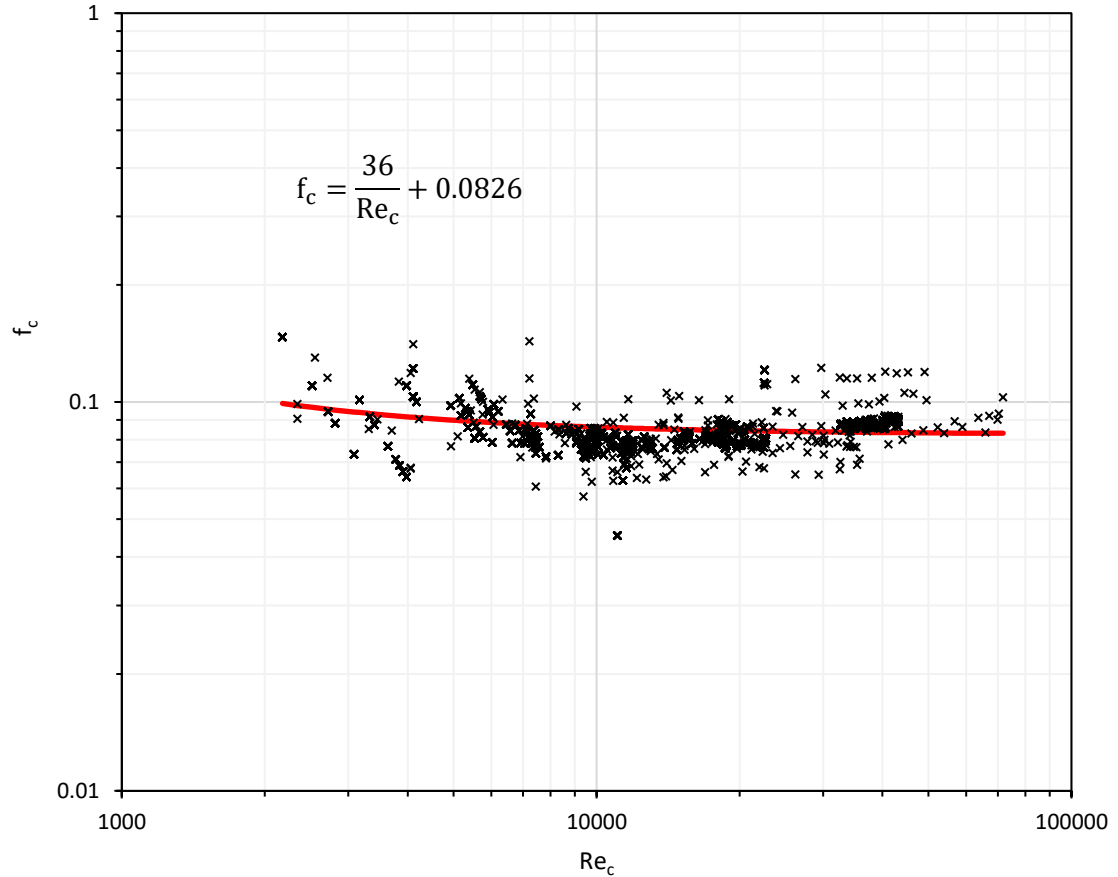
Figure 2.10. Aggregated experimental data in terms of the mixer friction factor and the mixer Reynolds number

The correlation and data were also compared to other available literature data at lower

Reynolds numbers to evaluate the robustness of the proposed correlation. The mixer geometrical

details given in each reference were used for calculating the relevant quantities and the tortuosity

was estimated from the values calculated using CFD in this study while interpolating for the

changes due to differences in diameter and void fraction. The data extracted from the literature

was fit surprisingly well by the correlation, even considering the disparate experimental

conditions and mixer geometrical details. The advantage of the proposed model over previous models lies in the fact that all the data extracted from the literature and measured in this study is well fit by the single model. Additionally, all key geometrical details governing the flow are taken into account by including the tortuosity and void fraction of the mixer, as opposed to only the void fraction. Inclusion of the tortuosity allows the data to collapse to a single correlation that accounts for differences in plate thickness, mixer fit, and length. It is possible that the tortuosity could be eliminated from the model by expressing as a function of the void fraction, similar to previous work in the area of porous media research [36]. This modification would simplify the model for ease of use, however this would require additional study.
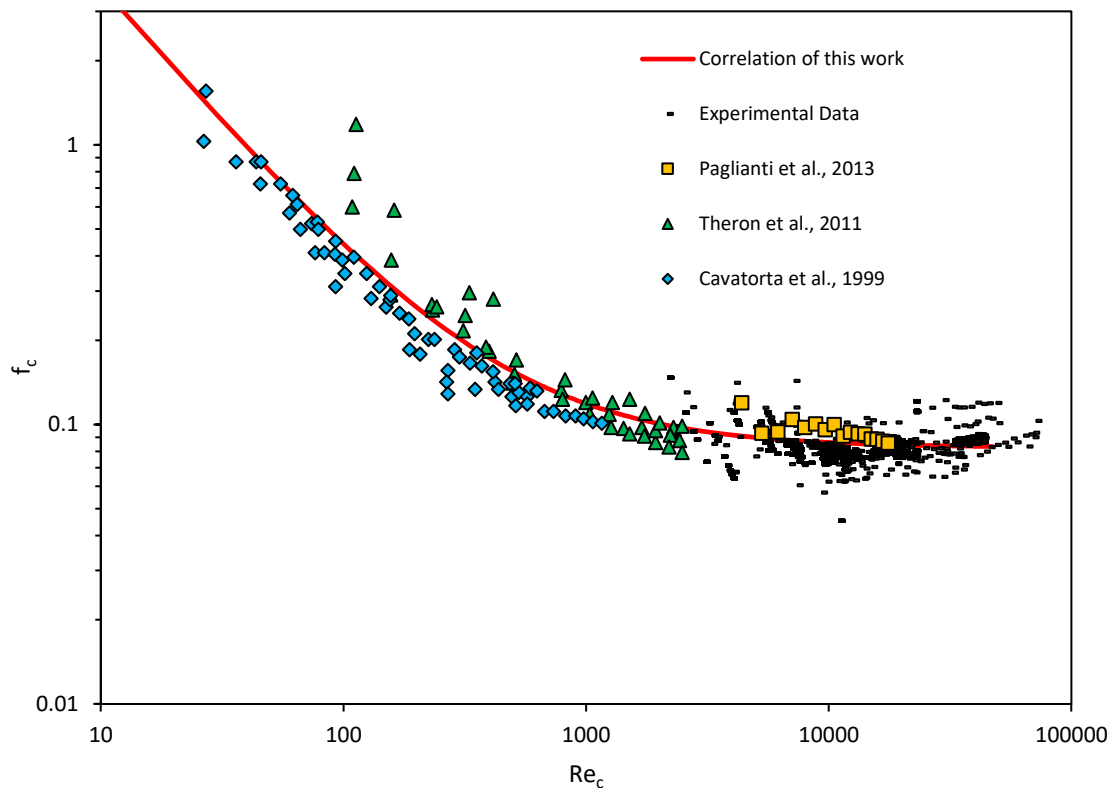
Figure 2.11. Literature data for single mixer-element pressure loss compared to the correlation of Equation 2.18 in terms of the mixer friction factor and the mixer Reynolds number

Lage & Antohe (2000) defined the flow regime boundaries as the point at which the

contributions of the viscous or inertial forces was less than 5% for the turbulent regime and the

Darcy regime, respectively. Adopting this criteria, the critical channel Reynolds number at which

turbulent flow starts is $Re_{c_T} = 8,300$ which is somewhat higher than previous works have

observed [40,43].

Finally, the Z-factors for the single mixer element were estimated from the experimental

data in the different pipe sizes as a function of Reynolds number. The figure below shows that

the Z factor ranges from 80 – 400 and is highly dependent on pipe diameter and roughness. This

may indicate that the Z factor is not a completely satisfactory method for pressure loss

determination.
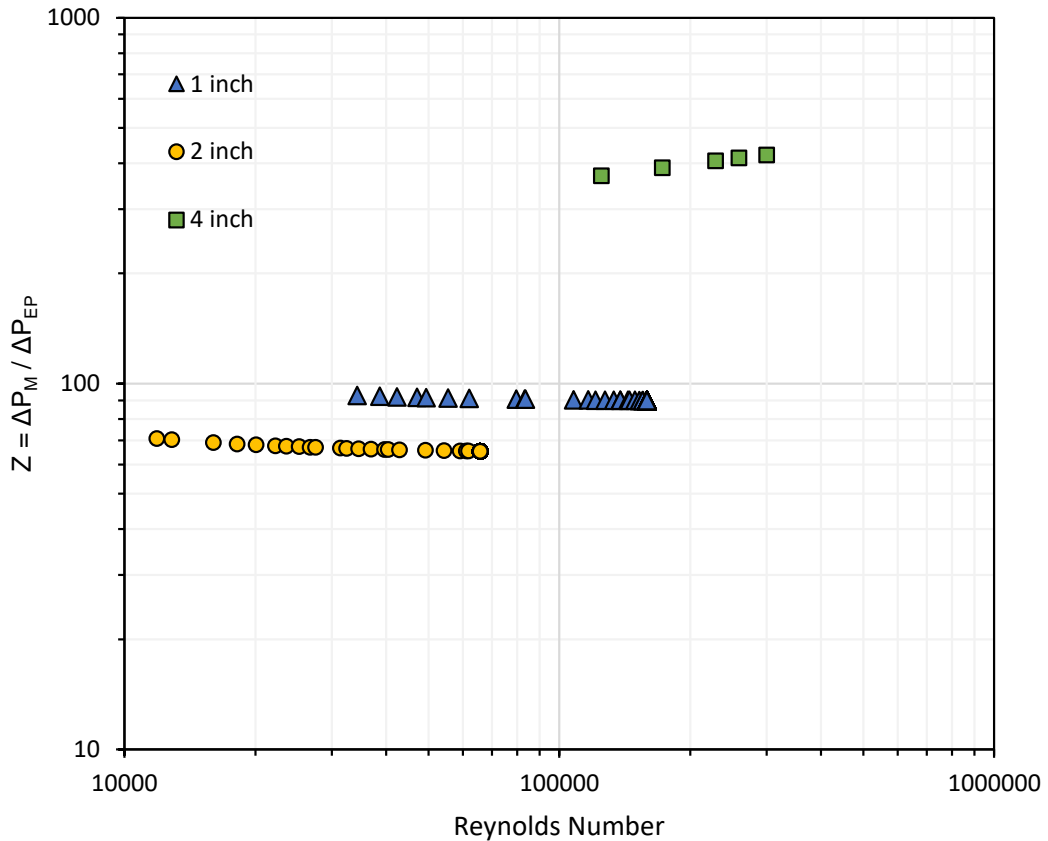
Figure 2.12. Z-factor estimates calculated from the experimental data for mixer and empty pipe (not all data points shown for clarity)

2.4   Conclusions

Robust, scalable correlations for pressure loss across SMV static mixers at high Reynolds (Re) numbers are currently lacking. This is first demonstrated by showing up to 45% deviation among current correlations at Re > 10000. To fill this void, an experimental and computational fluid dynamics (CFD) based study of a single corrugated static mixer for Reynolds numbers in the range of 10,000 – 250,000 is reported. The measurements were carried out in pipes of diameters of 1-inch, 2-inch, and 4-inch with significant variations in the pipe relative roughness.

The equivalent sand grain roughness was estimated based on the measurements and was provided as an input to the CFD model. The agreement of the CFD predictions with the measurements ascertained the validity of the roughness estimate. In an empty pipe, roughness contributed about 70-90% of the pressure loss at higher Reynolds numbers in the 1-inch and 2-inch stainless steel pipes and up to 7% of pressure loss in the 4 inch PVC pipe.

A new semi-analytical correlation for pressure loss across an SMV static mixer at high Reynolds (Re) numbers was proposed. The data was compared to the new proposed correlation as well as existing correlations from the literature. It was revealed that the existing correlations tend to under-predict the pressure losses compared to the measured data. On the other hand, our proposed correlation was able to account for the data of this study and also provide a satisfactory fit of the applicable raw data from the literature. This new correlation is more general since it accounts for the key geometric variables including tortuosity and void fraction. Additionally, the semi-analytical approach includes the impact of hydrodynamic roughness induced by the corrugated plate shape. CFD simulation was used to facilitate scale-up and delineate the pressure losses arising from roughness and manufacturing defects in these configurations. With the static mixer, roughness had up to a 60% contribution to the overall pressure loss, with the highest contributions in the 1-inch pipe. The Z-factor was also calculated and proved to be unsatisfactory for providing a generalizable correlation for pressure loss.

Overall, this study was able to provide a more robust correlation for the pressure loss in corrugated static mixers that may be easily extensible to geometrical variants without the need for additional measurements. Additionally, CFD was shown to be an acceptable tool for evaluating the pressure losses which further validates this method for scale-up predictions when large-scale data is unavailable. Future work will examine how the proposed correlation and CFD

simulation can be used to predict pressure losses in different linear mixer configurations and

orientations as well as developing links to mass transfer behavior in these types of mixers.

CHAPTER 3

An Improved Correlation for Dry Pressure Losses Across Static Mixers at

High Reynolds Numbers[2]

Abstract

Corrugated (SMV-style) static mixers are industrially important for process
intensification and can promote gas-liquid mass transfer in processes such as sour gas
sweetening. Current correlations for pressure loss are limited to Reynolds numbers (Re) below
40,000, far below the ranges encountered in natural gas systems (105 < Re < 107). An
experimental and numerical study of pressure drop across multiple corrugated mixers in the
range 104 < Re < 2 x 105 encompassing different configurations (aligned, rotated), pipe
diameters (1 inch to 4 inches) and sand grain surface roughness values (10 microns – 5,000
microns) is reported here. Our previous correlation for pressure loss across a single corrugated
element is shown to be extendable to multiple corrugated mixing elements. Through the
inclusion of mixer tortuosity (τ), porosity (ε), and macro-scale (geometric) wall roughness (e),
the correlation also matches historical pressure drop data (at different τ, ε) reported in literature
thereby demonstrating the utility of these variables as parameters that can help optimize mixer
performance. Experiments and computational fluid dynamics (CFD) modeling revealed that the
rotated configuration increased the residence time by up to 13% in comparison to the aligned
configuration. This may have implications on the selective absorption of sour gas components
that are based on fast kinetics. In addition, the role of wall roughness (both pipe housing and

mixer) was demonstrated to be significant in this study (accounting for 55% of the pressure losses) and must be accurately accounted for when scaling lab measurements.

3.1   Introduction

3.1.1   Sour Gas Sweetening

Global demand for natural gas continues to climb due to its status as an increasingly attractive alternative to petroleum and coal fuels for electricity generation, residential heating, and use as a petrochemical feedstock. Natural gas is currently abundant and provides excellent energy density and has a much lower carbon footprint compared to coal and liquid petroleum [6]. With U.S. production exceeding 36 trillion cubic feet per year, optimizing natural gas treatment strategies within an increasingly strained infrastructure is critical. Much of produced natural gas contains contaminants such as hydrogen sulfide (H_2S), carbon dioxide (CO_2), mercaptans, and oxygenates which must be removed prior to sale and use [44]. Gas-liquid mass transfer represents a common unit operation used to accomplish such contaminant removal [4]. Absorption of contaminants from gas streams with a liquid phase is common in applications used in processes ranging from creating grid-quality natural gas for fuel to ensuring clean air to limit environmental emissions.

Hydrogen sulfide in natural gas poses a significant challenge since it causes corrosion and is highly poisonous even at relatively low concentrations. Additionally, environmental release of hydrogen sulfide contributes to SO_x generation in the atmosphere. Traditional methods for removing hydrogen sulfide have been amine-treating towers with methyl diethanolamine (MDEA) solvent or other amine blends [44]. Although the most common method for accomplishing this type of operation is a trayed or packed tower, with increased demand for

intensified process equipment, co-current contacting is also an attractive solution [45]. In some cases, this mode of contacting offers more compact equipment footprints, reduced solvent usage, larger turndown ratios, and lower capital expenditure [8,11,46]. This is particularly true when only a few theoretical thermodynamic stages are required or when the reaction is fast [47]. Static mixing equipment is a natural choice for many co-current contacting scenarios. Static mixers reduce the overall reaction volume required for H_2S removal as compared to direct pipeline injection of MEA-triazine or caustic, which often causes solids precipitation or persistent liquid contamination issues downstream [48]. Additionally, many situations do not have adequate infrastructure for a Claus acid gas treatment process which further increases the viability of fast, non-regenerable methods as a less capital-intensive method for removal of H_2S [49]. Non-regenerable solvents such as caustic, hydrogen peroxide, and triazine have all been utilized with good effect. The need for methods of H_2S removal with lower cost and complexity have been previously identified in the literature [50].

3.1.2   *Static Mixers: A Technological Alternative*

Static mixing presents an attractive alternative to these traditional methods of H2S removal since it provides higher mass transfer capability in comparatively small capital equipment sizes [12]. Additionally, these devices designed in a modular manner allow for rapid deployment and re-use at various locations. The two major design criteria needed for proper sizing of a static mixing reactor are (1) accurate pressure loss prediction, and (2) mass transfer prediction, which is often a function of the pressure loss.

For in-line mixing with a gas continuous phase, the options for static mixers are sparse. The corrugated mixer has been identified as the best engineering design choice for this scenario

[13]. Corrugated static mixers, like the SMV-style mixer (originally manufactured by Sulzer Ltd.), are common in industry and combine high specific geometric surface area with proven performance [13,14]. Geometrically similar designs, such as MellapakTM, are often employed in the form of structured packing for vertical contacting installations [15]. Deploying a static mixer contactor requires the design engineer to thoroughly understand the pressure loss across the active contacting zone given that it is well known that pressure loss or energy dissipation relates to the mass transfer across a static mixer contactor [16]. Unfortunately, currently available correlations for pressure loss may only be accurate for Reynolds numbers that are too low to approximate realistic process conditions [17]. Current correlations fall short of accurately matching experimental data for Reynolds numbers higher than about 50,000 [16,18,19]. Other knowledge gaps are: pressure loss under process conditions, mean residence time (and approach to ideal plug flow), droplet size distribution, and interfacial area at high Reynolds numbers. This study is a first step towards filling this void in the existing literature.

To address this deficiency in the literature and extend previous work, an experimental study was conducted to measure the single-phase pressure loss through corrugated static mixers in a variety of pipe diameters and series configurations (i.e., aligned and rotated). A correlation developed in a preceding study was extended for predicting pressure loss across the range of tested diameters and configurations [17]. Highly resolved CFD simulations were also performed with OpenFOAM ver. 1912 to: predict pressure losses, deduce tortuosity from fluid pathlines and quantify the role played by mixer and pipe surface roughness. Finally, conclusions are presented relating to the applicability of the correlation and the role of CFD simulation in aiding the static mixer contactor design process.

3.2   Methods

3.2.1   Experimental System

Measurements of pressure drop across multiple corrugated mixers in the range $10^4 < \text{Re} < 2 \times 10^5$ encompassing different configurations (aligned, rotated), pipe diameters (1 inch to 4 inches) and sand grain surface roughness values (10 microns – 5,000 microns) were made in this study. The author's field experiences have shown that most gas processing pipelines operate within a range of Reynolds numbers between $10^5 < \text{Re} < 10^7$. Additionally, most pipeline sizes fall between 2 to 48 inches in diameter which justifies investigation of a wider range of diameters and Reynolds numbers. Operating pressures vary widely from up to 1,500 psig at the wellhead to less than 100 psig for distribution lines for sales gas [4]. Generally, the viscosity of natural gas is close to that of compressed air [51]. This information justified the use of compressed air as an environmentally safer proxy for natural gas for the laboratory measurements.

To measure the experimental pressure loss across the lab scale mixing elements, two flow systems were constructed. The first system was designed to operate with compressed air up to a pressure of 120 psig. Air flow (at 120 psig) was supplied by a 150 HP air compressor with a 1,000 gal pressure vessel. All process piping was composed of schedule 40 stainless steel in 1-inch nominal sizing. A pipe run of 24 inches was allowed after the inlet valve to allow the flow to fully develop prior to measuring the flowrate using a cylindrical averaging differential pressure probe. The differential pressure gauges for the flowmeter and measurement section were acquired from Alicat Scientific, Inc. (Tuscon, AZ, USA) and have a calibrated accuracy of 0.2% across the entire range of Reynolds numbers. A computer data acquisition system was used to log the data from the differential pressure meters. The system was capable of producing maximum velocities of around

44

30 m/s in the 1-inch empty pipe configuration (Re of 440,000). The piping configuration was constructed to allow the measurement section to be switched to a 2-inch nominal pipe run for measurements in a larger diameter. For all tests, a pipe run of at least 10 pipe diameters was placed before the measurement section to allow for flow development. A 1/8 inch stainless steel retaining stud was fixed in the bottom of the pipe to hold the mixing elements in place inside the pipe during testing.

To carry out testing in a 4-inch diameter pipe, a second experimental system was constructed to operate at near ambient pressure conditions with a 4-inch diameter PVC pipe conduit. A compressed air amplifier (Brauer Limited, Milton Keynes, UK) was used to boost compressor air to a max flowrate of 615 CFM (Re of 275,000) at near ambient conditions. The flowrate was monitored using a cylindrical averaging differential pressure probe and a differential pressure gauge manufactured by Dwyer (Michigan City, IN, USA) with an accuracy of 0.5% across the measurement range.

3.2.2   Static Mixer Configurations

Corrugated mixing elements with five plates and a corrugation angle of 45 degrees relative to the pipe axis were fabricated for use in the 1-inch, 2-inch, and 4-inch diameter pipes. The corrugated mixers were 3D-printed from acrylonitrile butadiene styrene plastic (ABS) material using the same 3D CAD drawing utilized for the CFD simulations. Two configurations were tested with both 2 and 3 mixer elements in series. The aligned configuration consists of mixer elements placed in series with no rotation of each mixer relative to the previous in series. By contrast, the rotated configuration consists of mixer placed in series with each consecutive mixer rotated by 90

degrees relative the previous. Figure 3.1 shows the aligned and rotated configurations with three mixing elements.

Figure 3.1. Aligned (A) and rotated (B) configurations with three mixing elements

Tsai et al. showed that flow channel configuration (45 vs. 60 degree channel angle) had essentially no bearing on the effective interfacial area but drastically affected the hydraulics [52]. Hohlfeld showed that for selective absorption of H2S a contact time of $0.01 - 0.03$ sec is required which may be accomplished with multiple mixers in various arrangements [50]. In addition, multiple mixers can have a positive impact on the droplet size/interfacial area [53,54]. Zhu et al. showed that mass transfer coefficient correlates to specific power [53]. Therefore more mixing elements may promote mass transfer while also increasing energy dissipation in the form of pressure drop. This information was taken into account when determining the corrugation angle and configurations to test in the laboratory.

3.2.3 Computational Fluid Dynamics Simulation

3.2.3.1 Grid Convergence

To properly ascertain the level of mesh refinement necessary to accurately simulate the pressure loss through the complex mixer geometry, a grid convergence study was conducted. The 1- and 4-inch mixer models were tested in the 3 rotated element configuration (i.e. three mixers oriented in the pipe at 90° with respect to each other). Meshes of coarse, medium, and fine spatial resolutions were constructed. All hex-dominant meshes were created using the snappyHexMesh utility provided in OpenFOAM version 1912.

Celik et al. [55] and Roache [56] present a comprehensive methodology for determining the uncertainty associated with a particular grid refinement level. The method relies on utilizing a Richardson extrapolation to determine the value of a particular variable of interest (i.e. velocity, or pressure loss) in the limit of infinitely small cell size. First, the representative cell size is calculated by Equation 3.1.

$$h = \left[\frac{1}{N} \sum_{i=1}^{N} (\Delta V_i) \right]^{\frac{1}{3}} \qquad\qquad 3.1$$

Where N is the number of cells and ΔV_i is the volume of the ith cell. The ratio of cell heights between the different refinement levels can be defined. In this case, refinement level 1 represents the finest mesh and refinement level 3, the coarsest mesh. Then the ratio between level 2 and level 1 would be $r_{21} = h_2/h_1$. The apparent order, p, may be calculated by iteratively solving Equations 3.2-3.3

47

$$p = \frac{1}{\ln(r_{21})} \left| \ln \left| \frac{\mathcal{E}_{32}}{\mathcal{E}_{21}} \right| + q(p) \right|$$ 3.2

$$q(p) = \ln \left(\frac{r_{21}^p - \left(\frac{|\mathcal{E}_{32}/\mathcal{E}_{21}|}{\mathcal{E}_{32}/\mathcal{E}_{21}} \right)}{r_{32}^p - \left(\frac{|\mathcal{E}_{32}/\mathcal{E}_{21}|}{\mathcal{E}_{32}/\mathcal{E}_{21}} \right)} \right)$$ 3.3

Where $\mathcal{E}_{ij} = \phi_i - \phi_j$ and ϕ is the variable of interest, such as pressure loss or local velocity. Finally, the extrapolated value may be calculated by Equation 3.4.

$$\phi_{ext}^{21} = (r_{21}^p \phi_1 - \phi_2)/(r_{21}^p - 1)$$ 3.4

The error relative to the extrapolated value can be estimated from Equation 3.5.

$$e_{ext}^{21} = \left| \frac{\phi_{ext}^{21} - \phi_2}{\phi_{ext}^{21}} \right|$$ 3.5

Finally, the grid convergence index (GCI), which has been shown to be a more reliable error estimate [55,56], can be calculated via Equation 3.6. Note the 1.25 factor which represents a safety factor.

$$GCI = \frac{1.25 e_{ext}^{21}}{r_{21}^p - 1}$$ 3.6

Steady-state, single-phase isothermal flow simulations were conducted at Reynolds numbers representing the low and high range from the experimental work for each of the meshes. A time-averaged representation of the flow field using the Reynolds-Averaged Navier Stokes (RANS) simulation approach was used to model the turbulent flow for all simulations in this

study. The two-equation realizable k-ε model was chosen to provide closure to the Reynolds

stress terms. The realizable k-ε model has been shown to provide good predictions of energy

dissipation at the walls for separated flows with adverse pressure gradients at high Reynolds

numbers that are representative of the flows encountered in this study [34]. Additionally,

previous work has indicated that the k-ε turbulence modeling framework leads to good

predictions when surface roughness is a factor, often better than other models such as the

Reynolds stress transport model [57,58].

Table 3.1. Grid convergence simulation results with 3 rotated 1- and 4-inch elements

Re	Refinement	Diameter	Cell Count	h (m)	Max Velocity at Outlet (m/s)	ΔP (Pa)
13,880	Coarse	4	665,858	1.92E-03	3.83	38.1
	Medium	4	2,263,454	1.27E-03	4.05	39.2
	Fine	4	4,401,870	1.02E-03	4.25	39.6
	Extrapolated	4	-	0.00E+00	4.41	39.9
145,738	Coarse	4	665,858	1.92E-03	41.12	3717.9
	Medium	4	2,263,454	1.27E-03	39.19	3756.4
	Fine	4	4,401,870	1.02E-03	38.57	3768.5
	Extrapolated	4	-	0.00E+00	38.03	3778.6
27,760	Coarse	1	371,828	5.14E-04	4.45	95.0
	Medium	1	1,272,002	3.41E-04	4.49	94.7
	Fine	1	2,969,864	2.57E-04	4.24	98.5
	Extrapolated	1	-	0.00E+00	4.08	100.3
208,197	Coarse	1	371,828	5.14E-04	32.85	5292.6
	Medium	1	1,272,002	3.41E-04	30.17	5326.5
	Fine	1	2,969,864	2.57E-04	29.52	5341.8
	Extrapolated	1	-	0.00E+00	29.36	5350.6

Figure 3.2 presents the pressure loss and max velocity profiles across the various grid

refinements for a few selected cases. The extrapolated continuous value is also shown based on

the calculations using Equations 3.1-3.6. Oscillation was only detected on one set of solutions

with the 1-inch domain under low Reynolds number. The oscillatory behavior between the

medium and fine mesh refinements did not preclude finding an extrapolated solution in this case.

Indeed, other studies have found that the Richardson extrapolation is capable of estimating error

even is oscillation is present between refinement levels [59].
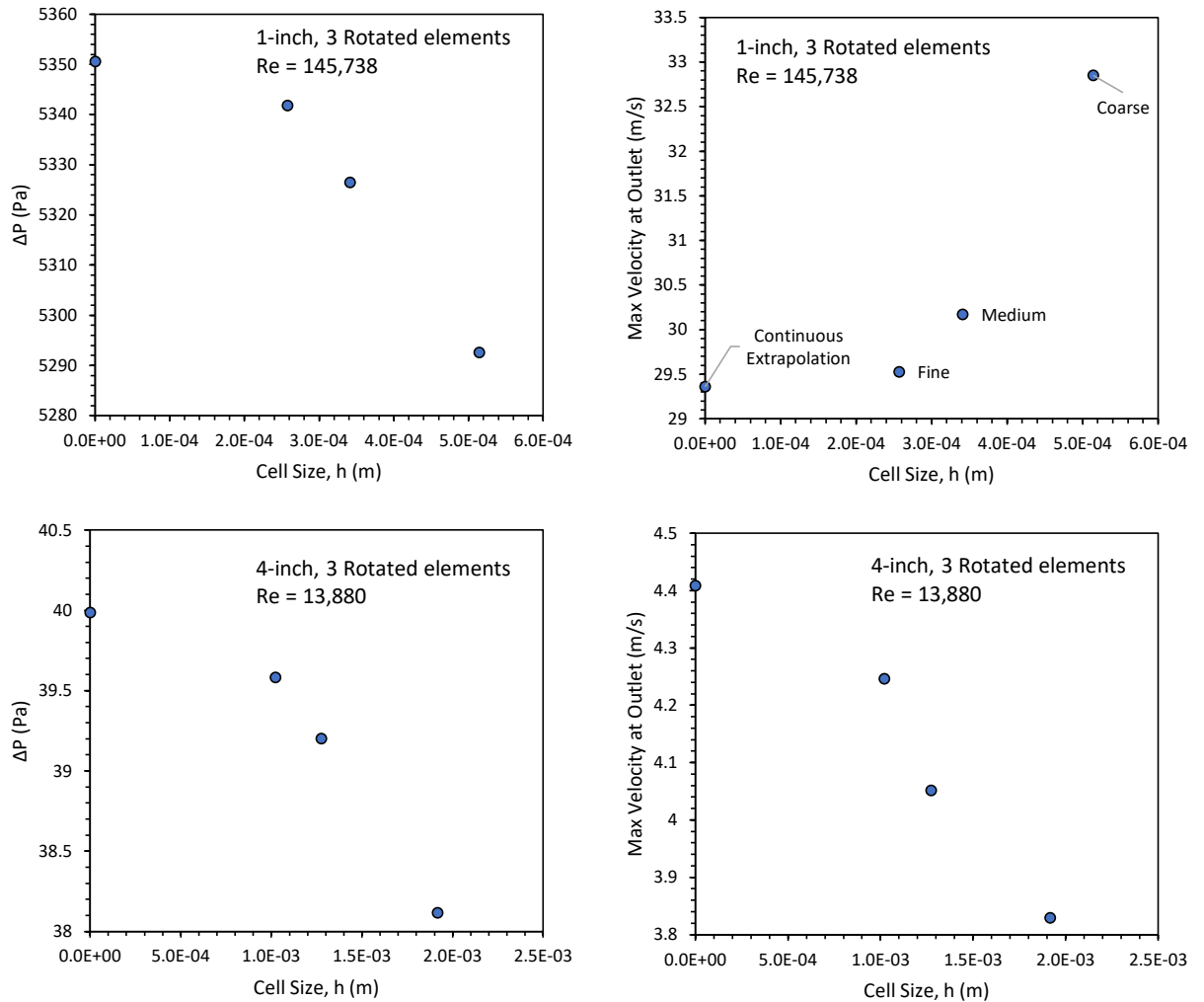
Figure 3.2. Pressure loss and velocity trends across the various grid refinements tested. The extrapolated continuous value is also shown based on the calculations from Equations 3.1-3.6

The calculated GCI for the medium mesh refinement is provided in Table 3.2. Based on

these results and the practical focus of this study, the errors associated with the medium mesh

refinement were deemed acceptable.

Table 3.2. Grid convergence index (GCI) calculated for the medium mesh refinement

Diameter	Re	GCI - Medium mesh	
		dP/L	Max Outlet Velocity
1	27,760	2.6%	8.5%
1	208,197	0.6%	3.3%
4	13,880	3.4%	7.6%
4	145,738	0.3%	1%

Figure 3.3 shows the velocity profile at a slice near the outlet for all mesh refinements under the high Reynolds number conditions in the 1-inch domain with 3 rotated elements.
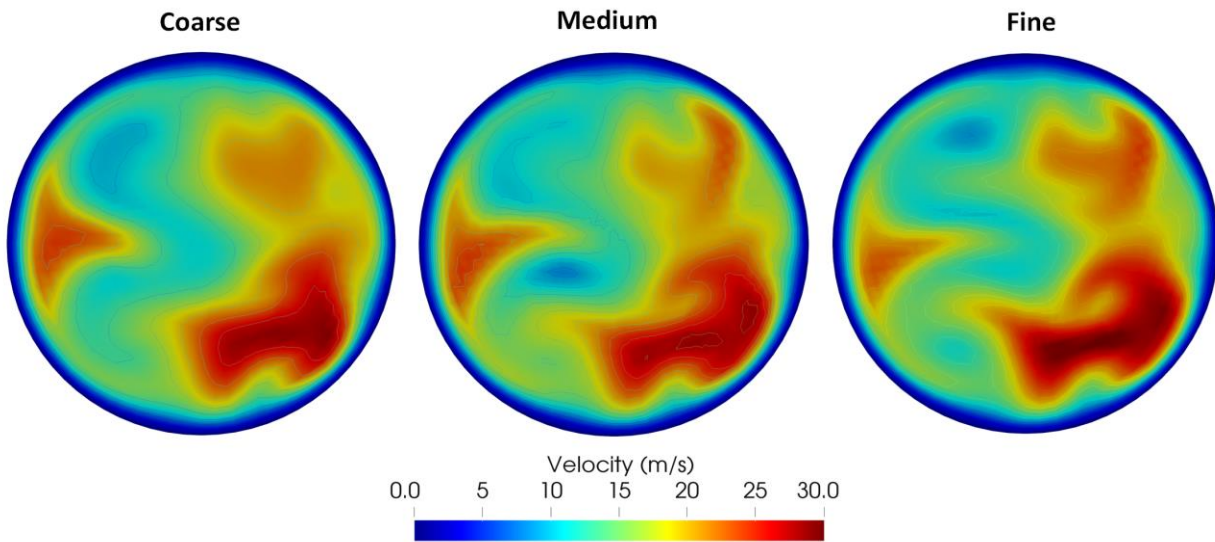
Figure 3.3. Velocity profiles near the outlet of the 1-inch domain with 3 rotated elements at high Reynolds number for each mesh refinement level.

3.2.3.2 Pressure Loss Simulations

Simulations of the total steady-state pressure losses were conducted using meshes created for 2 and 3 mixers in series at the medium refinement level determined during the grid

convergence study. Two configurations were tested as well; aligned and rotated described in the experimental section. The pressure drop of the different configurations of corrugated mixers were evaluated using OpenFOAM ver. 1912 with the simpleFoam solver. The solver is a steady-state solver for isothermal incompressible flow. The SIMPLEC solver was chosen due to its proven fast, robust convergence [33]. Second-order upwind schemes were utilized for the flow and turbulence variables. Each simulation was run to convergence which was assessed by ensuring that the pressure loss (the variable of interest in this study) varied by less than 0.01% between iterations. The input density and viscosity were matched to the experimental conditions (i.e. air at ambient temperature and relevant experimental pressures).

3.2.3.3 Numerical implementation of sand grain roughness in OpenFOAM

Sand grain wall roughness is implemented natively in OpenFOAM version 1906 in the form of the `nutkRoughWallFunction`. This model manipulates the turbulent viscosity near the wall based on the turbulent kinetic energy to shift the near wall velocity distribution and account for simulated roughness. The wall is treated differently based on the dimensionless roughness parameter (K_s^+) defined in Equation 3.7.

$$K_s^+ = \frac{C_\mu^{\frac{1}{4}} \sqrt{k} K_s}{\nu_w} \qquad\qquad 3.7$$

In Equation 3.7, C_μ is an empirical constant, K_s is the equivalent sand grain roughness, ν_w is the near wall kinematic viscosity, and k is the turbulent kinetic energy at the wall.

If $K_s^+ \leq 2.25$ then no shift to the near wall velocity is applied, and the standard wall functions are utilized. If $2.25 < K_s^+ < 90$ then a transitional roughness function (f_n) is used to correct the law-of-the-wall as shown by Equation 3.8.

$$f_n = \left(\frac{K_s^+ - 2.25}{87.75} + C_s K_s^+ \right)^{\sin\left(0.4258\left(ln\left(K_s^+\right)\right)-0.811\right)} \qquad 3.8$$

If $K_s^+ \geq 90$ then the wall is treated as fully rough and the correction function (f_n) takes the form of Equation 3.9.

$$f_n = 1 + C_s K_s^+ \qquad 3.9$$

In the fully rough regime, the viscous sub-layer is completely destroyed. The correction to the near-wall turbulent viscosity is then accomplished via Equation 3.10.

$$\nu_{t_w} = \nu_w \left(\frac{y^+ \kappa}{\ln\left(\frac{y^+}{f_n}\right) - 1} \right) \qquad 3.10$$

Apsley [57] showed that the single-value and grain roughness implementation in CFD can accurately match predictions for rough pipe flow given by the Colebrook-White equation. The study showed that CFD simulation using the k-ε turbulence modeling approach could produce accurate predictions provided the near wall $y^+ > 13$ which, on average, is met by all of the simulation geometries investigated in this study. Although the minimum y^+ value for some mesh cells was below this threshold value of 13, the deviation occurs at high curvature areas where mesh resolution demanded smaller values. The total cells that fell below this cut-off was calculated at less than 1% for the final meshes chosen for production simulations.

3.2.3.4 Verification of sand grain roughness implementation in OpenFOAM

To ensure that the OpenFOAM implementation was providing rational predictions with the current wall roughness implementation, simulations with an empty pipe at various roughness

heights and Reynolds numbers were also completed. For this an empty pipe mesh was also created using the software Gmsh which is capable of creating all-hexahedral cylindrical meshes with low skew [32].

For all simulations, the impact of roughness was included using the native roughness handling implemented in the `nutkRoughWallFunction` boundary condition Figure 3.4 shows the OpenFOAM predictions superimposed on the classic Moody chart for the Darcy friction factor [60]. Overall, the OpenFOAM wall roughness implementation produced results in good agreement with the Moody chart with an average variation of 5% across the range of wall roughness investigated (0 to 1,270 microns).
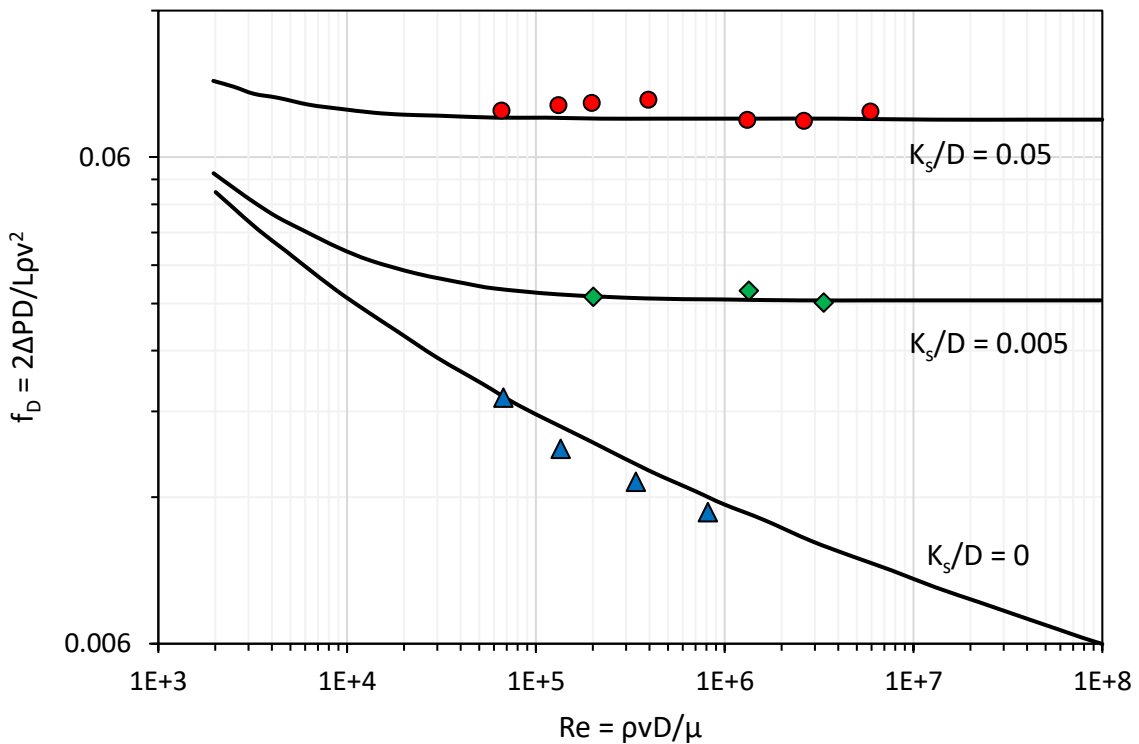
Figure 3.4. Darcy friction factor data from the Moody chart (lines) along with friction factor predictions from OpenFOAM (symbols) [60]

Although the use of a single sand grain roughness has been questioned previously in the literature [61], the OpenFOAM implementation was shown to be adequate for the purposes of this study. For instance Kadivar et al. emphasized that the Moody diagram can over-estimate the friction factor for commercial steel pipes [61]. However, a more important issue regarding the use of Moody diagram is that of defining an appropriate roughness length scale to use as the roughness height. The Moody diagram was developed using the equivalent sandgrain roughness height, K_s. However, K_s for a generic roughness cannot be accurately assigned *a priori* and must be determined experimentally/deduced from measurements as summarized above.

Having ascertained the validity of OpenFOAM's wall roughness model, the empty pipe wall roughness of our 1-inch, 2-inch and 4-inch pipes were deduced by first measuring the pressure drop across the pipes at different Reynolds numbers. Next, the Colebrook-White equation was used to fit the experimnetal data and calculate the relative roughness [62]. The validity of the calculated wall roughness height for each pipe was then checked by repeating simulations with `nutkRoughWallFunction` at multiple flow Reynolds numbers and ensuring that they matched the corresponding empty pipe pressure loss measurements.

The relative roughness of the mixing elements themselves was based on the materials of construction provided by the fabricactors. These values were used directly as input to `nutkRoughWallFunction` for all simulations. While all the details associated with this process are omitted for the sake of brevity, the deduced grain roughness heights (K_s) associated with the empty pipe and mixing elements are summarized in Table 3.3 and the details are available in a previous study [62].

Note, in Table 3.3, that the high values of roughness for the pipe obtained in the experiment for the 1- and 2-inch empty pipes is attributable to the mixer element support structure which consisted of a retaining stud and weld beads around the curcumference of the pipe. Due to the difference in pipe material (PVC vs. steel) and scale, the 4-inch sized mixing elements were retained in the pipe with an interference fit between the mixing element plate edges and the pipe wall, thereby elminating the need for a retaining stud and leading to the lower relative roughness values for the pipe.

3.2.3.5 Determination of Tortuosity

One of goals of this study was to investigate if our previously developed pressure loss correlation across a single static mixer element was extendable to multiple mixer configurations [62]. One of the parameters in the correlation was the tortuosity across the different configurations. Given that experimental determination of this parameter can be tenuous and difficult in more complex geometries, a CFD methodology was adopted and validated. The definition of tortuosity is given in Equation 3.11, where *L* is the overall length of the mixer (or series of mixers) in the primary flow direction, and ℓ is the average streamline length through the mixer or mixers [36].

$$\tau = \ell/L \qquad\qquad\qquad 3.11$$

Using the post-processed flow field generated by OpenFOAM, the streamlines were evaluated to extract an average length. Figure 3.5 shows an image of a typical set of post-processed streamlines in the 2 element configurations. Note that Figure 3.5 does not show all streamlines used for the analysis for the sake of visual clarity. To validate the procedure used to

calculate tortuosity and determine the optimal number of streamlines to utilize for computation, a sensitivity study was conducted using simulation data from the 1-inch case with 2 aligned mixer elements. The results are shown in Figure 3.6 and indicate that an average path length from least 10,000 streamlines need to be calculated to estimate tortuosity that is accurate to two significant figures.
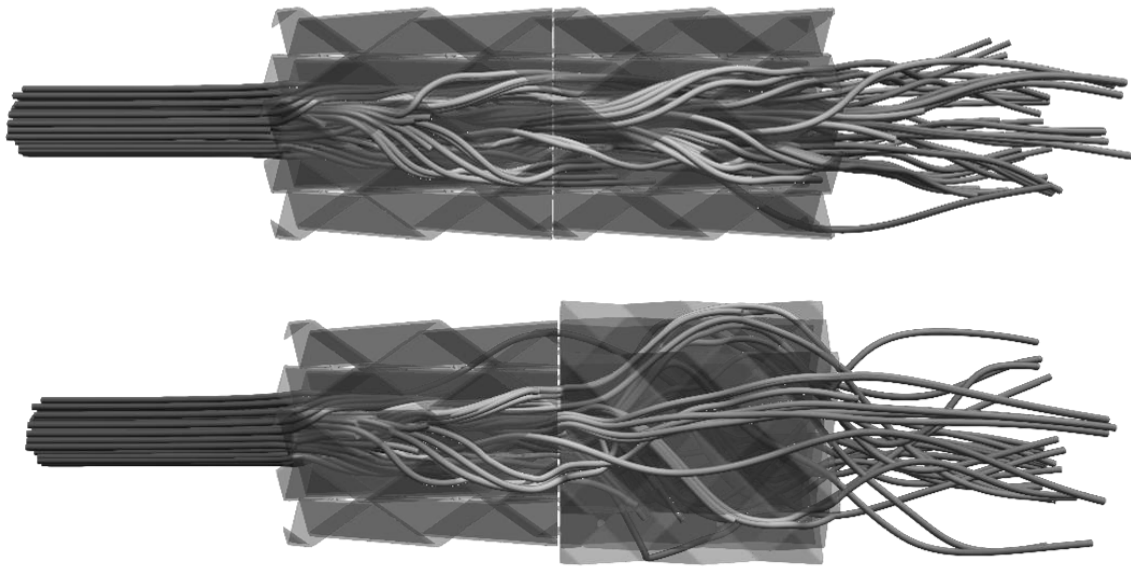
Figure 3.5. Example of streamlines calculated from CFD for the calculation of tortuosity: (Top) Two mixing elements (aligned); (Bottom) Two mixing elements (Rotated)

The procedure was then repeated across all the mixer configurations investigated and the results are summarized in Table 3.3.
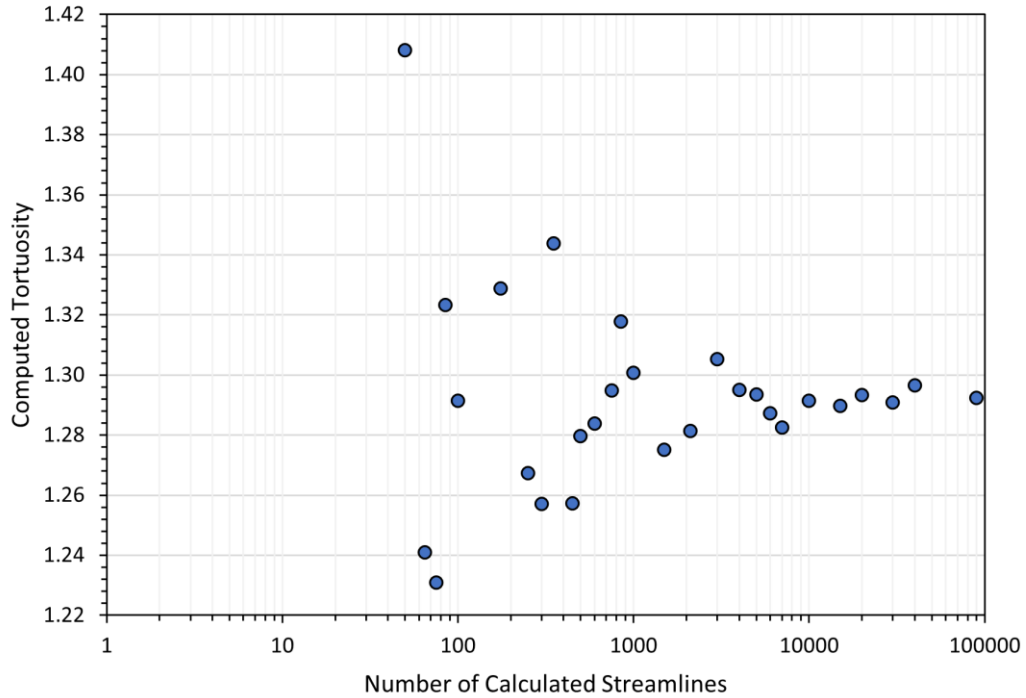
Figure 3.6. Sensitivity analysis for tortuosity calculation procedure for 1-inch case with 2 aligned mixer elements.

3.2.3.6 Mean residence time

Estimates of the mean residence time were also made by post-processing the fluid path lines in ParaView. The streamlines were calculated from the inlet of the mixer composite to the outlet of the mixer and the residence times estimated by averaging across all path lines. An average of 10,000 streamlines was calculated for each residence time average. Mean residence times for all sizes and configurations tested are shown in Figure 3.7. Figure 3.7 provides an initial estimate of mixer configurations that might provide adequate residence time (0.01 – 0.03 sec) for H_2S capture by caustic solutions at different Reynolds numbers. The difference in mean residence time between the aligned and rotated configurations diminishes at higher Reynolds numbers (increasing mixer diameter and/ velocities).
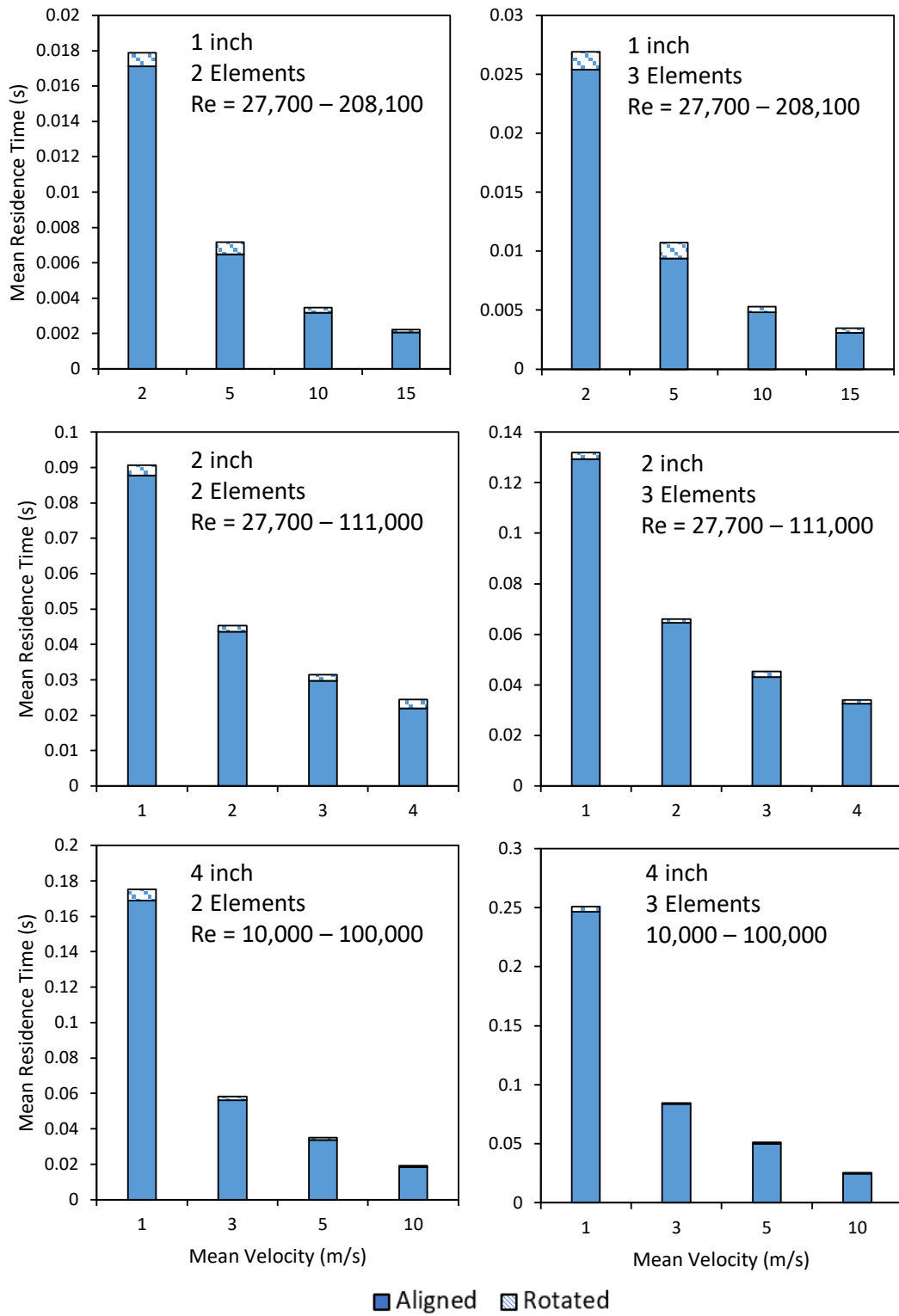
Figure 3.7. Mean residence times for different mixer configurations, diameters, and velocities

3.3   Results

3.3.1   Literature Model Comparison

The pressure loss data was aggregated and plotted against other currently available literature models. The models of Paglianti et al. [16], Cavatorta et al. [18], and Bravo et al. [17] were included in the analysis. For the model of Paglianti et al. [16], the values of porosity (ϵ) and the mixer channel hydraulic diameter D_c were identical to those in Table 3.3.

For the models of Cavatorta et al. [18] and Bravo et al. [17], the values of a' (edge length of plate corrugation) were extracted directly from the CAD files of the mixers. The sand grain roughness of the mixer elements were also determined from the materials of construction and the roughness of the pipe housing were also determined by measuring pressure loss in the empty pipe housing without mixers and fitting to the Colebrook-White equation. Extensive details of this procedure are given in previous work [62] and they compared well against the estimates from CFD (section 2.2.4) that are reported in Table 3.3.

Table 3.3 Experimental and CFD Model Mixer Element Dimensions

D (in)	L/D	Configuration	ε	τ	D_c (in)	$K_{s\text{-}mixer}$ (micron)	$K_{s\text{-}pipe}$ (micron)
1	1	1 Element		1.32			
		2 Aligned Elements		1.30			
		2 Rotated Elements	0.756	1.32	0.129	10	4,679
		3 Aligned Elements		1.28			
		3 Rotated Elements		1.34			
2	1	1 Element		1.29			
		2 Aligned Elements		1.29			
		2 Rotated Elements	0.879	1.34	0.315	10	5,347
		3 Aligned Elements		1.33			
		3 Rotated Elements		1.34			
4	1	1 Element		1.29			
		2 Aligned Elements		1.30			
		2 Rotated Elements	0.879	1.31	0.693	100	11
		3 Aligned Elements		1.30			
		3 Rotated Elements		1.32			

It is worth noting that the pipe roughness values reported in Table 3.3 are much higher than those reported in the literature for similar materials of construction. For instance, in experimental studies [63,64] equivalent sand-grain roughness of commercial steel pipes was computed by fitting flow measurements to the Colebrook or Nikuradse correlations and K_s was found to be in the range 2-20 μm. Additionally, surface roughness measurements via scan or via contact equipment indicated a 1-20 μm range. Even for a rough steel pipe, Galavics [65] reported a value of 130 μm, which is less than an order of magnitude than the K_s values for steel pipes in the shown in Table 3.3.

While the pipe and fittings used for this experimental apparatus were indeed rough (visually), the major contributor to the roughness values were: the retaining studs placed inside the pipe (to prevent the static mixing devices from flowing downstream) and the weld beads in the pipe walls. Since, geometrically resolving the retaining studs and pipe wall weld beads would

dramatically increase the mesh count, their effects were accounted for in the "equivalent sand grain roughness height" (K_s) employed in the simulations. While we did not attempt to specify a spatially varying sand grain roughness height in our simulations, we did indeed assign distinct values of K_s for the mixer and pipe based on experimental determinations, as shown in Table 3.3.

Figure 3.8 shows the aggregated results of the pressure loss measurements in 1-, 2-, and 4-inch sizes and multiple configurations. The model of Paglianti et al. [16] fit the data the best, especially at lower Reynolds numbers. This is likely because Paglianti et al. addressed the pressure losses between mixers using an interfacial length concept which is analogous to tortuosity [16]. At Reynolds numbers greater than 50,000, all the available literature models were unable to predict the pressure loss characteristics accurately. In particular, Paglianti et al. [16] reports data only up to a Reynolds number of 40,000 whereas the models of Cavatorta et al. [18] and Bravo et al. [17] are limited for Reynolds numbers below 10,000. It is likely that all the literature models are limited by being formulated primarily on low Reynolds number data. Indeed, although Streiff et al. [30] presents some data at higher Reynolds numbers, it is not sufficiently generalized for geometry and flow variables to be broadly useful or reproducible. The data of this study is consistent with previous studies that suggest that pressure losses are generally higher through corrugated mixing elements as compared to other industrial mixers. Despite this, the corrugated style mixer has been shown to produce very high interfacial area in co-current flow configurations, making it an attractive choice for mass transfer operations [19,66].
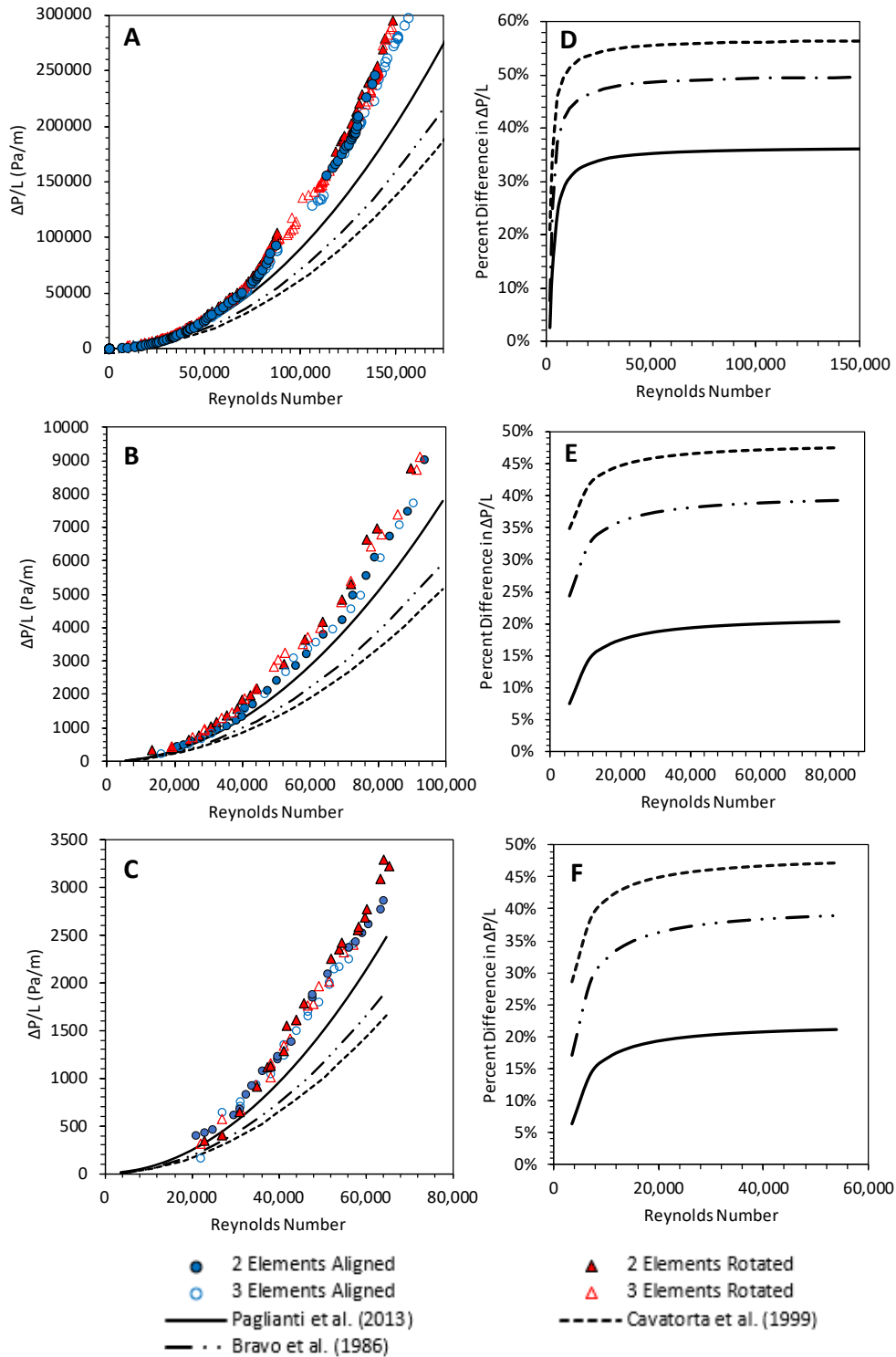
Figure 3.8. Pressure loss data and models of Pagliani et al. [18], Cavatorta et al. [16], and Bravo et al. [19], for 1-inch (A), 2-inch (B), and 4-inch (C), and percentage difference between the literature models and the experimental data of this study for 1-inch (D), 2-inch (E), and 4-inch (F)

3.3.2 Semi-Analytical Model

3.3.2.1 Pressure Drop per Unit Length

It was desirable to adopt a theoretical model that permitted sufficient generalization in terms of geometrical and flow variables to be broadly applicable. The model of Comiti and Renaud [38] was originally formulated for generalized flow through a packed bed. In this study, we adopt and expand this approach to provide a more general framework for pressure loss modeling in corrugated mixer geometries that can extend over a wide range of flow conditions (Re > 50,000 in particular).

First, the superficial velocity through the mixer can be expressed as a function of the mean flow velocity (u_0), the tortuosity (τ) and void fraction (ϵ) of the mixer [38].

$$u_s = \frac{u_0 \tau}{\epsilon} \qquad\qquad 3.12$$

Where $\tau = \ell/\mathrm{L}$ and ℓ is the average streamline length through the mixer of length, L. At low Reynolds numbers, the pressure loss through a porous media is proportional to the viscous forces and the kinetic energy losses of the flow. However, at high Reynolds number conditions, the kinetic-energy losses comprise the largest contribution to pressure loss. The model presented by Comiti and Renaud is useful for understanding generalized flow through a porous media [38]. By grouping the viscous pressure loss term, expressed by the Poiseuille equation with modifications, and the kinetic terms, a combined pressure loss expression for flow through a porous structure may be expressed [39]. Similarly, the pressure losses through a static mixing element can be expressed in terms of the viscous losses (ΔP_v) and the kinetic losses (ΔP_k). The addition of these two terms results in the total pressure loss across the mixer (ΔP_T).

$$\Delta P_T = \Delta P_k + \Delta P_v \tag{3.13}$$

For the static mixer, the viscous losses may be described by the Poiseuille equation with several key modifications. First, since the flow through the mixer channel is turbulent in this scenario, the parabolic velocity profile assumed by the traditional formulation of the Poiseuille equation is no longer accurate. In laminar flow, the maximum velocity occurs at the centerline of the conduit and the average fluid velocity under laminar flow is defined by Equation 3.14.

$$u_{0_{lam}} = \frac{u_{max}}{2} \tag{3.14}$$

In contrast, during turbulent flow the velocity profile changes and no longer follows the parabolic profile. The power-law velocity profile as been shown to describe the average turbulent flow velocity profile adequately. The relationship between the maximum velocity and the average velocity based on the power-law velocity profile is expressed as Equation 3.15 where n is the power-law index.

$$\frac{u_{0_{turb}}}{u_{max}} = \frac{2n^2}{(n+1)(2n+1)} \tag{3.15}$$

Hinze (1975) proposed Equation 3.16 as a method to determine the power-law index based on the Reynolds number [67].

$$n = -1.7 + 1.8\log(Re_c) \tag{3.16}$$

Utilizing the minimum Reynolds number measured in the mixer channel in this study (Re_c: 2784), the power law index is calculated as $n = 4.5$. Using this value in Equation 3.15 and

substituting the results in Equation 3.14 yields a correction factor (α_1) for the turbulent flow in the mixer channel.

$$\alpha_1 = \frac{u_{0\,turb}}{u_{0\,lam}} = \frac{0.74}{0.5} = 1.48 \qquad\qquad 3.17$$

Secondly, the standard Poiseuille equation is primarily validated for cylindrical flow conduits. It has been shown that the Poiseuille equation must be corrected for non-circular conduits, like the triangular mixer channel in this work. Utilizing the correction factors determined by Lewis & Boose (1995), the shape correction has been determined $\alpha_2 = 1.52$ [68]. The final formulation for the viscous contributions is given in Equation 3.18.

$$\frac{\Delta P_v}{L} = \frac{\alpha_1 \alpha_2 32 \tau^2 \mu u_0}{\epsilon D_c^2} \cong \frac{72 \tau^2 \mu u_0}{\epsilon D_c^2} \qquad\qquad 3.18$$

Note that for different flow regimes or mixer channel shapes, the values of α_1 and α_2 may change. The kinetic contributions can be expressed by the Darcy-Weisbach formulation with modifications for the porous nature of the mixer.

$$\frac{\Delta P_k}{L} = \frac{2 C_p \tau^3 \rho u_0^2}{\epsilon^2 D_c} \qquad\qquad 3.19$$

This leads to the new formulation presented in Equation 3.20.

$$\frac{\Delta P_T}{L} = \frac{72 \tau^2 \mu u_0}{\epsilon D_c^2} + \frac{2 C_p \tau^3 \rho u_0^2}{\epsilon^2 D_c} \qquad\qquad 3.20$$

In Equation 3.20, C_p is the effective friction factor of the interior mixer channel wall. When the assumption is made that the macroscopic roughness (e) (i.e. geometric bends) of the channels is on the same order of magnitude as the channel diameter itself, the friction factor of

the channel can be estimated via the classic Nikuradse equation for fully turbulent flow in highly rough pipes in the natural logarithm form [42]:

$$\frac{1}{\sqrt{C_p/2}} = 2.46 \ln\left(\frac{D_c}{2e}\right) + 4.92 \qquad\qquad 3.21$$

Under the assumption that $e \cong D_c$, the friction factor for the kinetic-loss term becomes $C_p \cong 0.1936$. which is appropriate when the channels have many flow directional changes before impacting the pipe housing. However, when the mixer channels end at the pipe housing wall, as in the case of the corrugated mixer in this study, a better assumption is that $e \cong D_c/2$ which leads to $C_p \cong 0.0826$ by solving Equation 3.21 [38].

3.3.2.2 Friction Factor

By re-arranging Equation 3.20, a combined friction factor for the mixer as a porous media may be conveniently defined:

$$f_c = \frac{D_c \Delta P \epsilon^2}{2L\rho u_0^2 \tau^3} = \frac{36\epsilon\mu}{\rho u_0 \tau D_c} + C_p \qquad\qquad 3.22$$

The dimensionless first term on the right hand side of Equation 3.22 is a Reynolds number for the mixer channel which can is defined in Equation 3.23.

$$Re_c = \frac{\rho u_0 \tau D_c}{\epsilon\mu} \qquad\qquad 3.23$$

Finally, combining Equations 3.21, 3.22, and 3.23, the semi-analytical friction factor model for the mixer in terms of the channel geometry is given in Equation 3.24.

$$f_c = \frac{36}{Re_c} + 0.0826 \qquad\qquad 3.24$$

This final expression is used as a semi-analytical basis for comparison with the experimental data. Equation 3.20 can be functionally expressed in terms of total pressure loss via Equation 3.25.

$$\frac{\Delta P_T}{L} = \frac{2 f_c \rho u_0^2 \tau^3}{D_c \epsilon^2} \qquad\qquad 3.25$$

The first term of Equation 3.24 represents the viscous contributions to flow and is primarily controlling in the low Reynolds number regimes. The second constant term is attributable to the losses in high turbulence associated with the rough corrugations and dominates at high Reynolds numbers. Legrande (2002) proposes that the change from Darcy flow to transitional flow occurs near $Re_c = 13$ and the fully turbulent regime starts near $Re_c = 830$ [40] although a previous study found that the transition may occur at higher Reynolds numbers in the corrugated mixer geometry [62]. This correlation respects the finding of previous studies that the friction factor reaches constant value at high Reynolds numbers [69]. Qualitatively, the correlation also bears resemblance to skin friction factor profiles for rough surfaces measured by Flack et al [70]. It is important to note that the correlation only accounts for the macroscopic roughness, manufacturing and geometric features, rather than microscopic roughness which was included in the CFD study.

3.3.3   Model Validation

The experimental data was aggregated and processed by calculating the pressure loss per unit length of mixing elements. The pressure losses due to the empty pipe sections that didn't

include any mixer elements were subtracted to obtain the actual losses associated with each mixer configuration. The experimental data along with the predictions of Equation 3.25 are presented in Figure 3.9 – Figure 3.11 for the 1-, 2-, and 4-inch mixing elements. Based on the results, several trends emerged. First, the aligned configurations exhibited lower pressure losses compared with the rotated configuration. This is somewhat intuitive given the more complex flow path associated with the rotated configuration. For the rotated configurations, the addition of more elements (i.e. from 2 to 3 elements) led to slightly less total pressure loss *per unit length* on average. This may be due to the dilution of the contributions from mixer inlet/outlet losses by the overall internal pressure losses [71].
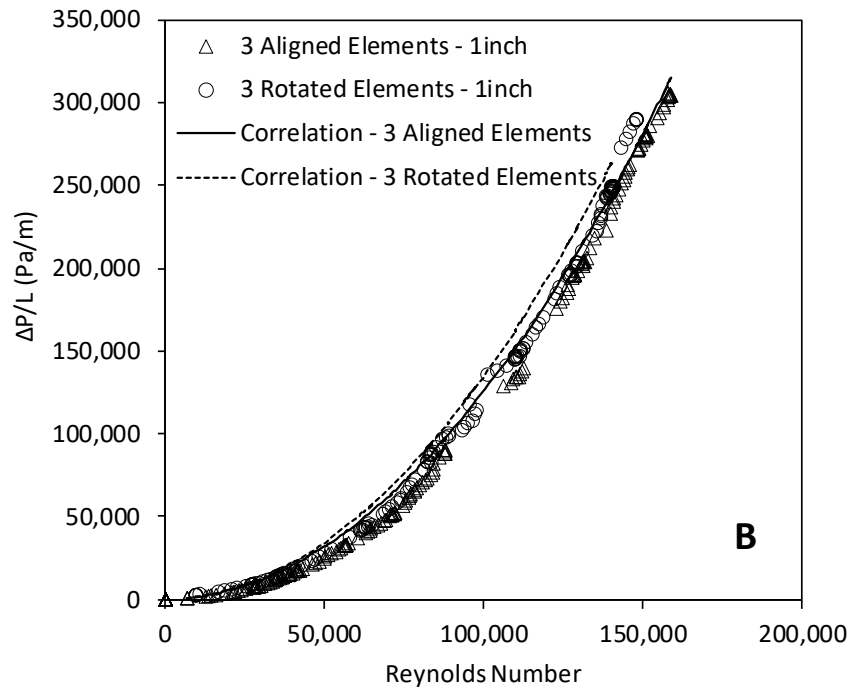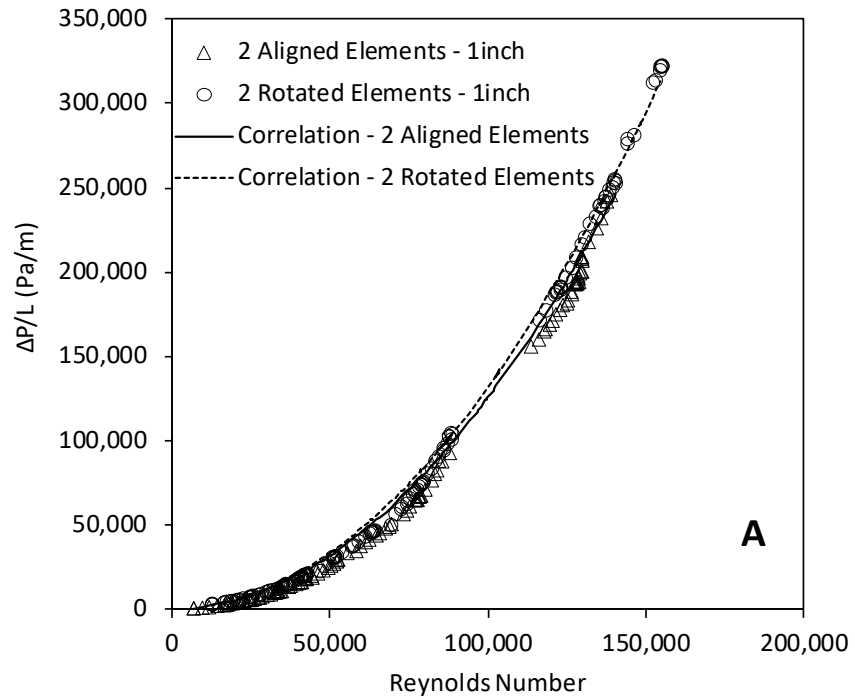
Figure 3.9. Pressure loss data compared with the semi-analytical model presented in Equation 3.25 for 1-inch corrugated mixer elements for 2 mixer elements (A) and 3 mixer elements (B)
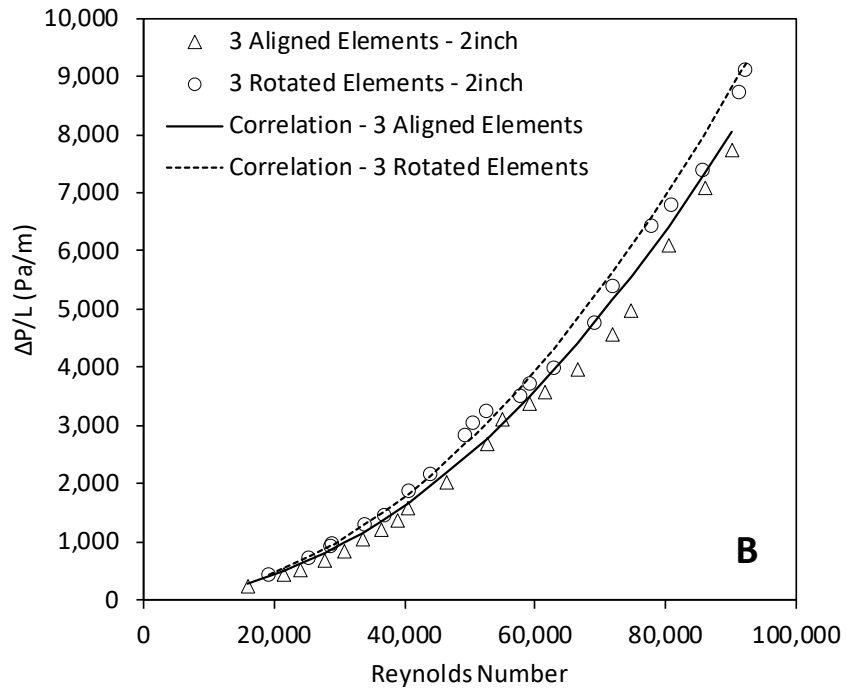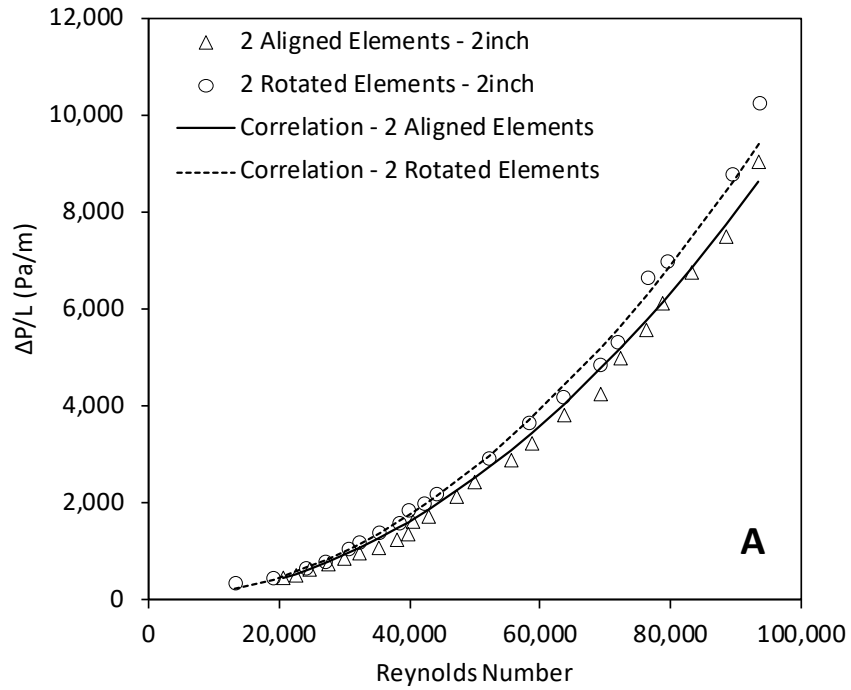
Figure 3.10. Pressure loss data compared with the semi-analytical model presented in Equation 3.25 for 2-inch corrugated mixer elements for 2 mixer elements (A) and 3 mixer elements (B)
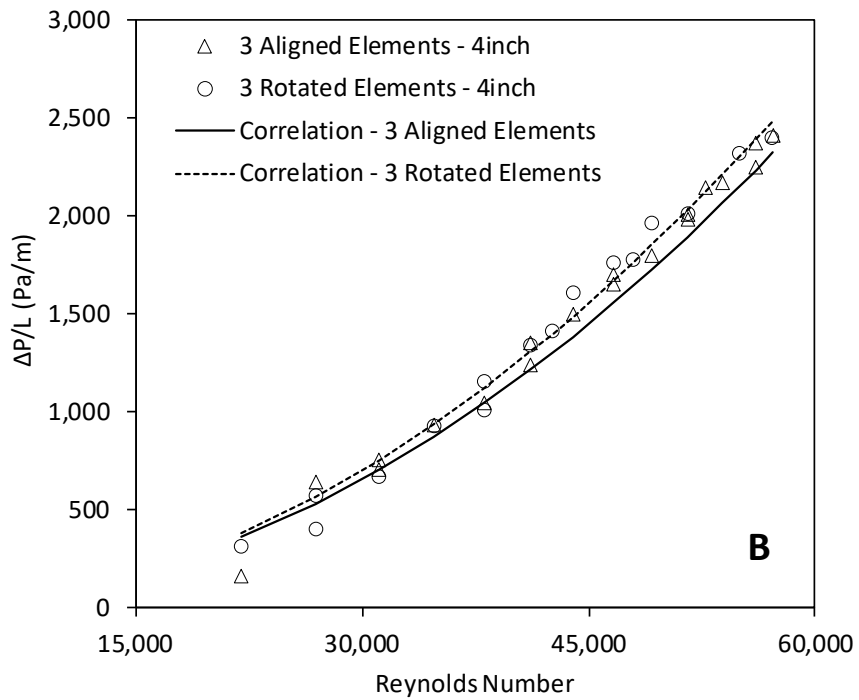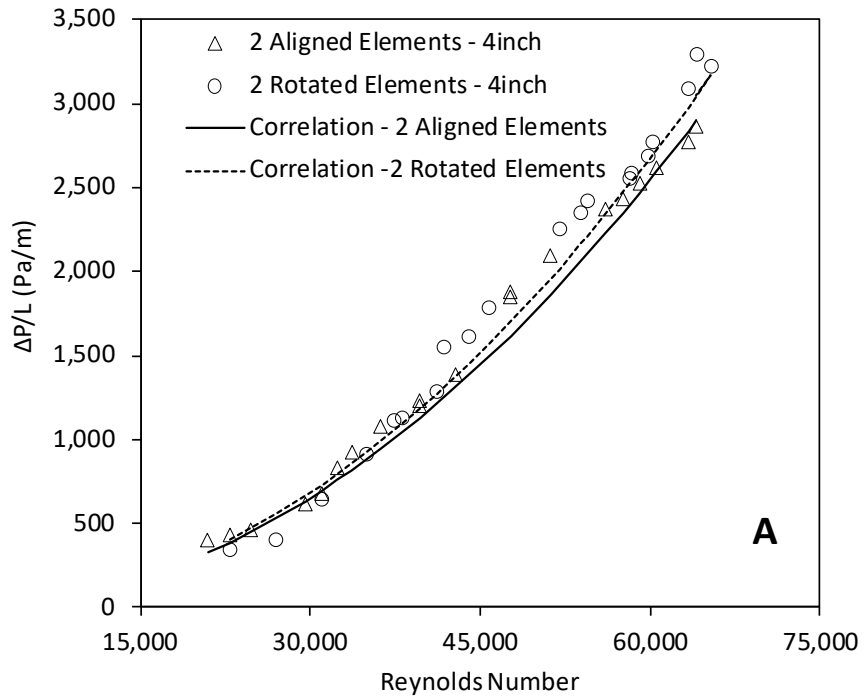
Figure 3.11. Pressure loss data compared with the semi-analytical model presented in Equation 3.25 for 4-inch corrugated mixer elements for 2 mixer elements (A) and 3 mixer elements (B)

The semi-analytical model was generally accurate at predicting the pressure losses associated for the different diameters and configurations. The inclusion of tortuosity in the correlation appeared to capture the small difference in pressure losses between the aligned and rotated configurations. For all the data, the mean absolute percentage error (MAPE) for the data compared to the predictions of semi-analytical correlation (cf. Equation 3.25) is given in Table 3.4. The correlation showed the best predictions above pipe Reynolds numbers of about 30,000.

Table 3.4. Mean absolute percentage error (MAPE) of the semi-analytical model (Equation 3.25) compared to the experimental data

Configuration	Nominal Diameter (in)		
	1	2	4
1 Element	13.4%	8.9%	16.4%
2 Aligned Elements	12.8%	7.4%	7.2%
2 Rotated Elements	15.0%	5.1%	8.3%
3 Aligned Elements	13.8%	9.9%	11.7%
3 Rotated Elements	9.7%	4.0%	7.6%

To further validate the accuracy and capability of the semi-analytical correlation for prediction of pressure losses in various configurations, the data of Paglianti et al. [16] was extracted for comparison to the correlation. The data was extracted for 0.04 m diameter, 5-plate corrugated mixing elements in the aligned and rotated configuration with 2 and 3 elements. The void fraction of each mixer was listed by the authors as $\epsilon = 0.63$. To determine the tortuosity, a mixer with the same size and void fraction was created from the original CAD model and the tortuosity for each scenario was estimated using the CFD method described in the earlier sections. The parameter D_c was also determined from the CAD model since it was not provided by the authors.
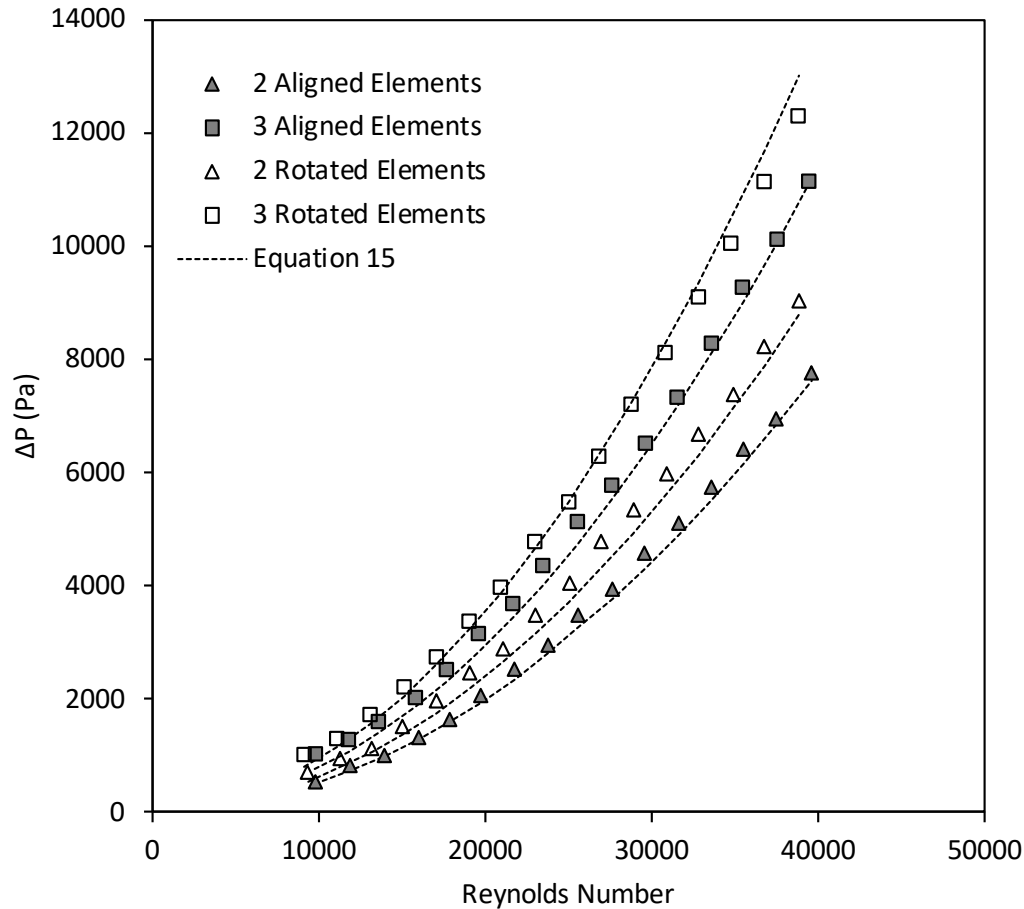
Figure 3.12. Data of Paglianti et al. [16] plotted with the semi-analytical model of Equation 3.25

The data of Paglianti et al. [16] was predicted quite well by the model of Equation 3.25 as shown in Figure 3.12. The experiments of Paglianti were carried out for the fluid near that of water (995 kg/m^3) and Reynolds numbers up to about 45,000 [16]. The semi-analytical model could predict the pressure loss with an overall MAPE of 6.7% compared to the experimental data in Figure 11. The error was higher for Reynolds numbers below about 15,000 which suggests the use of Equation (19) should primarily be at higher Reynolds number conditions.

It is noteworthy that the reported values are well within the pressure drop of 13,800 Pa that is reported as optimal for operating co-current H$_2$S scrubbers [50]. Energy dissipation rates

and mass transfer coefficients were compared in literature and correlated well indicating that large pressure drops (within appreciable limits) are acceptable as long as it promotes effective mass transfer [72,73].

3.3.4   CFD Prediction of Pressure Loss

3.3.4.1 Comparison with Correlation

OpenFOAM CFD simulations were evaluated for prediction of the pressure loss across multiple configurations and diameters for the corrugated mixers. The fluid conditions of the experiments were used as input to all the simulations. The rotated and aligned configurations were evaluated in the 1-, 2-, and 4-inch sizes. The sand grain roughness for the pipe wall and mixer elements was determined previously and is given in Table 3.3. Figure 3.13 – Figure 3.15 show the CFD simulation results along with the semi-analytical model. Overall, OpenFOAM provided good agreement with experimental measurements and the semi-analytical correlation of Equation 3.25.
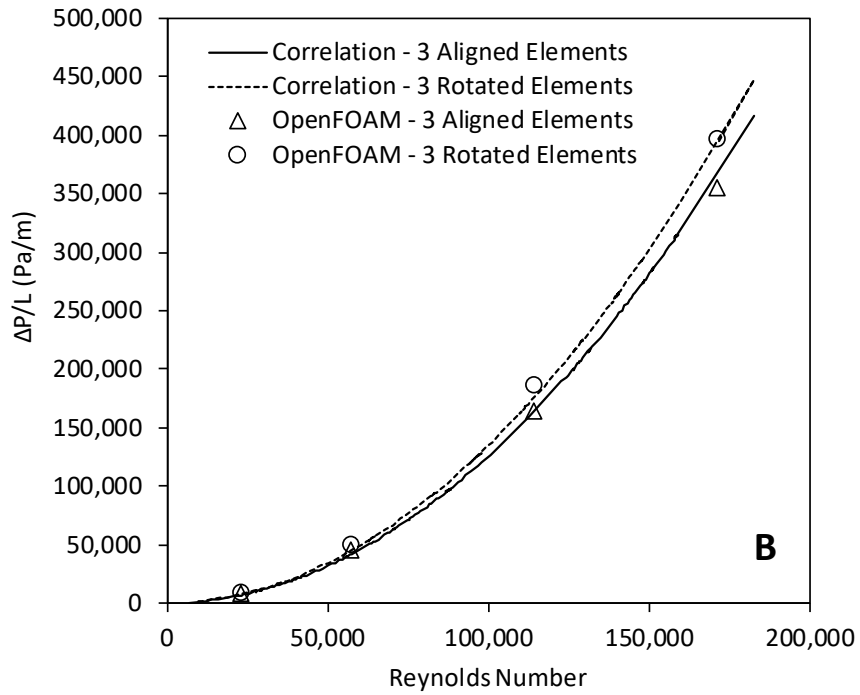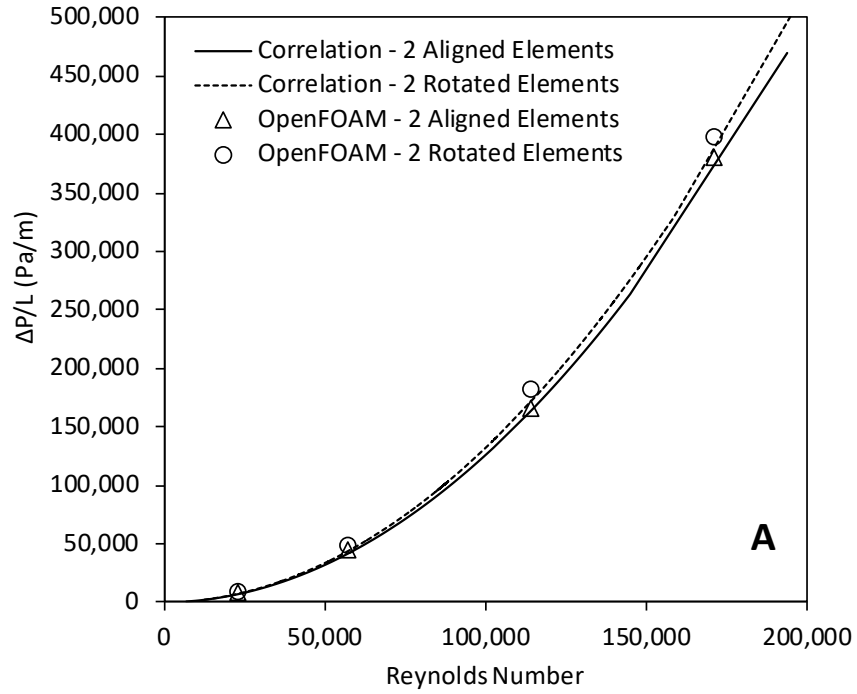
Figure 3.13. OpenFOAM CFD simulations compared to Equation 3.25 for the 1-inch mixer configurations for 2 mixer elements (A) and 3 mixer elements (B)
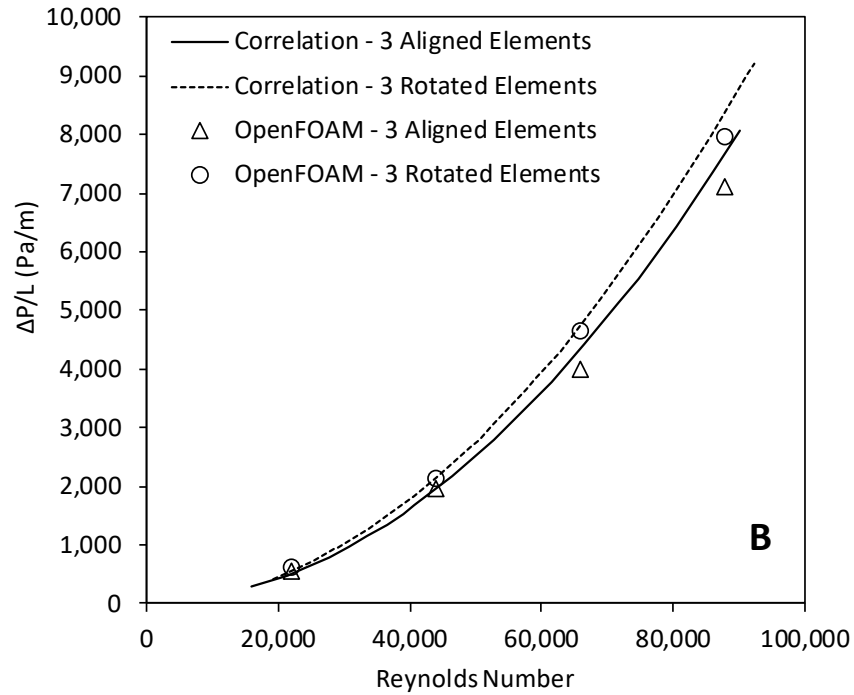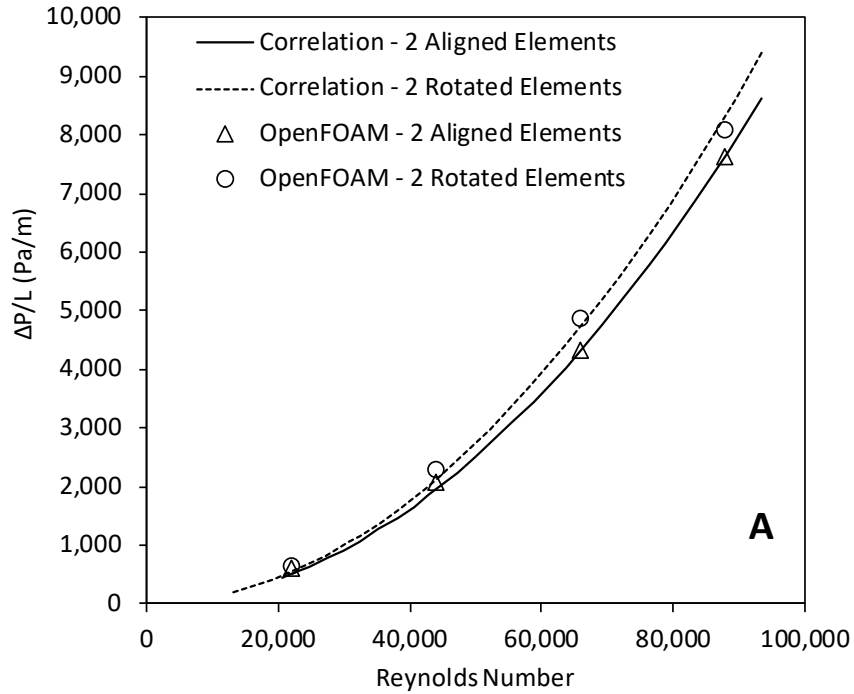
Figure 3.14. OpenFOAM CFD simulations compared to Equation 3.25 for the 2-inch
mixer configurations for 2 mixer elements (A) and 3 mixer elements (B)
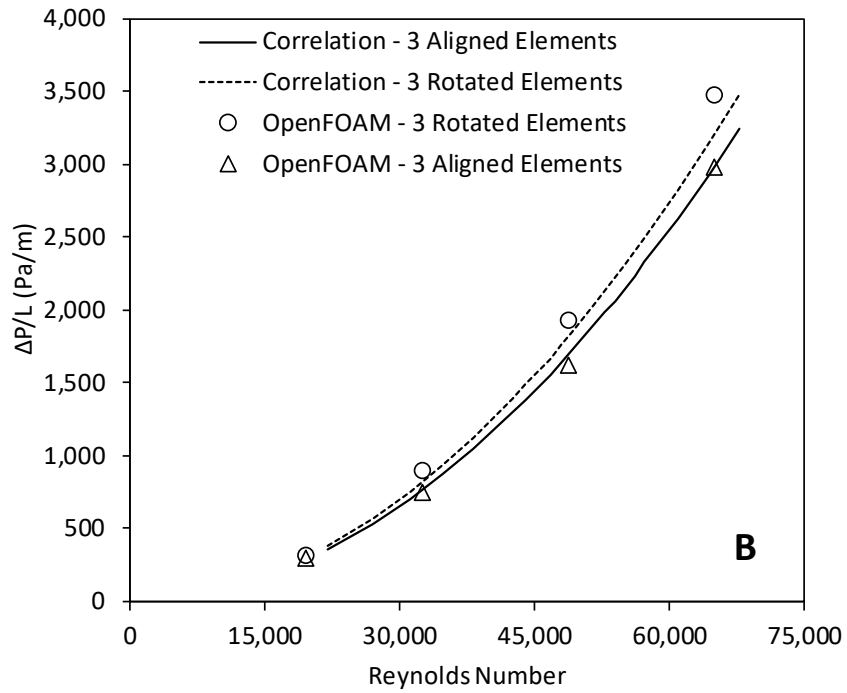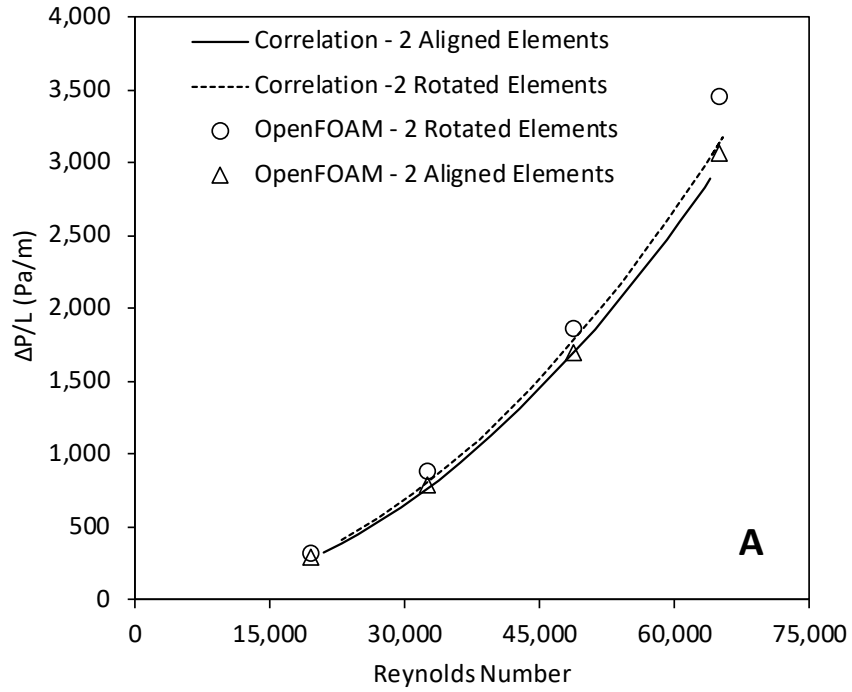
Figure 3.15. OpenFOAM CFD simulations compared to Equation 3.25 for the 4-inch mixer configurations for 2 mixer elements (A) and 3 mixer elements (B)

78

3.3.4.2 Impact of Tortuosity and Void Fraction

To examine the ability of the correlation to account for wide variations in tortuosity and void fraction, a 1-inch (25.4mm) diameter CAD model of a mixer with thicker corrugated plates was created. This mixer model possessed a tortuosity of 1.17 (compared to 1.3 for the original design) and a void fraction of 0.447. As before, the pressure loss was simulated over a range of Reynolds numbers using OpenFOAM. The correlation of Equation 3.25 was also calculated using the new design. Figure 15 shows the large impact of changing the tortuosity and void fraction on the overall pressure loss profile. As would be anticipated, the lower void fraction contributed to much larger pressure losses through the mixer. Despite the changes, the correlation of Equation 3.25 was able to account for the geometric differences and predict pressure loss values similar to those produced by OpenFOAM.
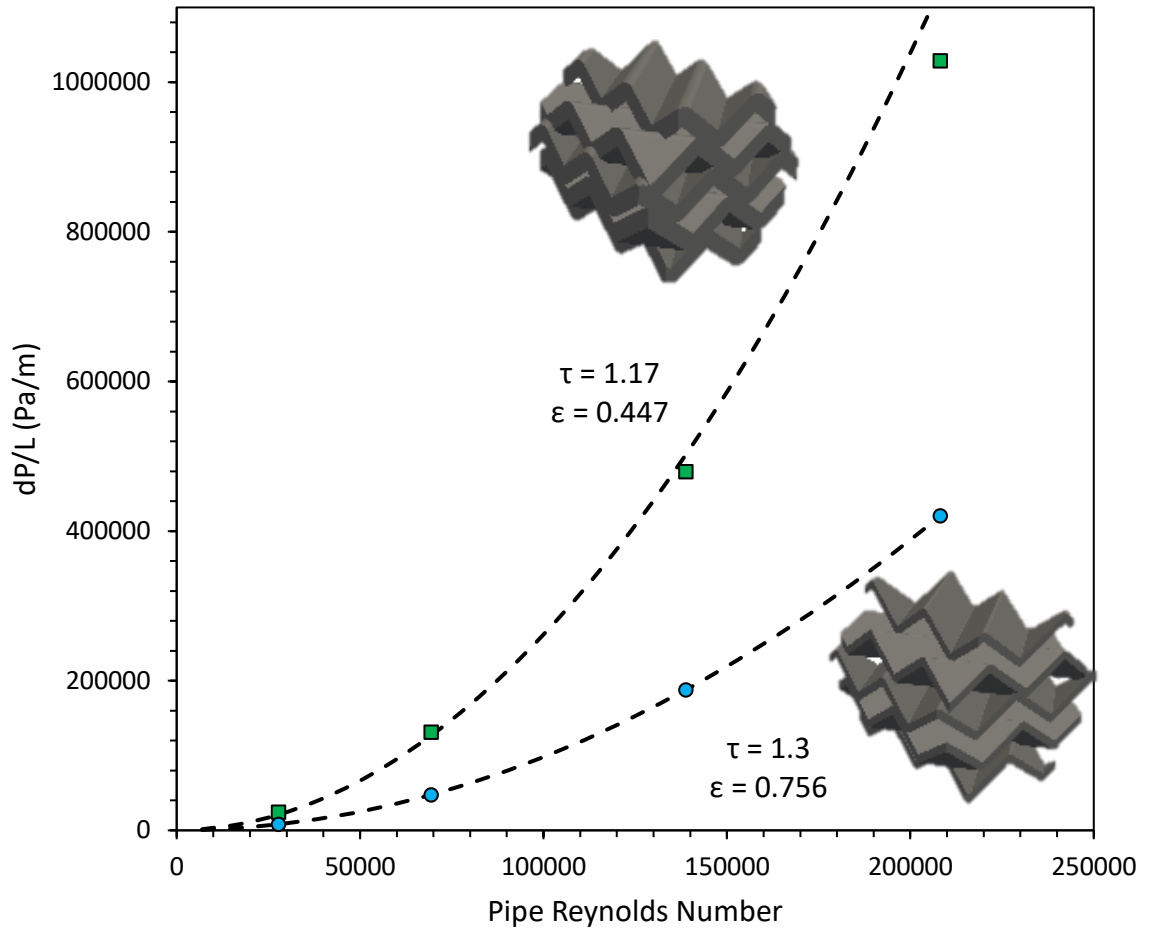
Figure 3.16. Pressure loss predictions for CFD simulations of single 1-inch mixers with different tortuosity and void fraction compared to the correlation of Equation 3.25 (dashed lines)

3.3.4.3 Impact of Roughness

The impact of roughness was evaluated by running the same simulations as previously without the wall roughness implementation in OpenFOAM (i.e. fully smooth wall). The impact of roughness is larger and contributes up to 55% of the total pressure losses in the smaller diameter pipe sizes, especially at lower velocities. As would be expected, the roughness in the 4-inch pipe size resulted in the smallest impact on the overall pressure loss. These results

demonstrate the importance of including roughness when utilizing lab and pilot scale

measurements for generalizing correlations.
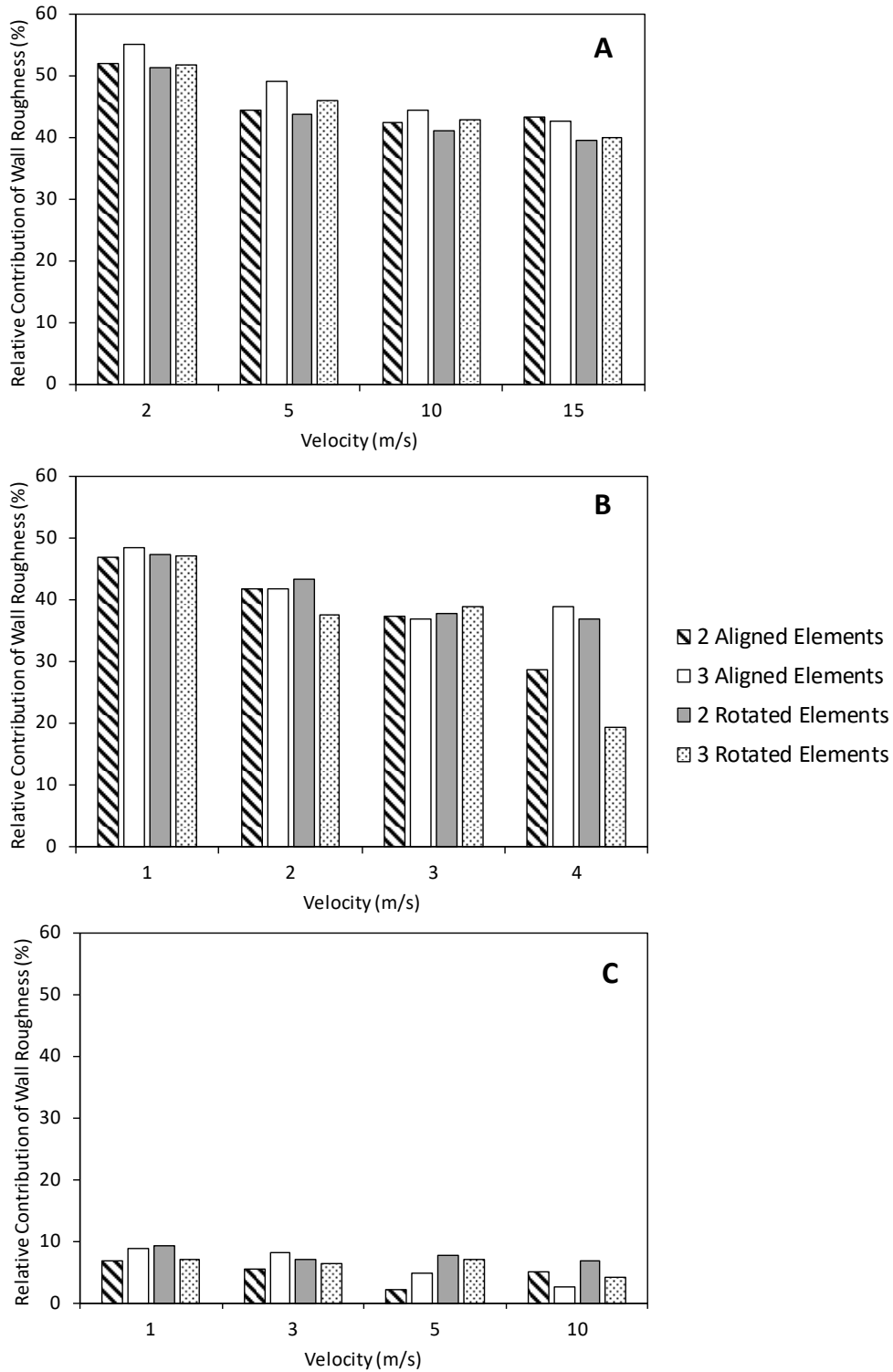
Figure 3.17. Difference in pressure loss predicted by OpenFOAM CFD with and without wall roughness for 1-inch (A), 2-inch (B), and 4-inch (C) static mixers

Comparison of the CFD simulations with the experimental data made clear that failing to account for roughness can results in large under- or over-prediction of pressure loss when using lab data to scale-up for applications in the field. As a result of this study, we recommend the following experimental workflow when conducting pressure loss measurements at laboratory scales.

1. Ensure that the roughness of the conduit is measured or able to be approximated. This is more critical in pressurized gas piping where imperfections or rough connection points are more common.

2. Subtract or otherwise account for any excess losses in the system that occur between the differential pressure measurement locations (i.e. excess pipe run or connections).

3. If conducting CFD simulations, utilize sand grain roughness estimates within the simulations to aid in developing predictions that are more accurate, remembering that roughness effects will be more dominant at smaller diameters.

3.4   Conclusions

Corrugated mixing elements are a viable option for sour gas sweetening in the range of Reynolds numbers encountered in natural gas pipeline systems between $10^5 < \text{Re} < 10^6$. Unfortunately, currently available correlations for pressure drop across these configurations have been formulated for $\text{Re} < 10^4$ and can show widespread prediction disparity (up to 50%) when extended beyond their intended range of application. To fill this void, the results from an experimental and numerical study of pressure drop for Re in the range ($10^4 < \text{Re} < 2\text{x}10^5$) encompassing different configurations (aligned, rotated) of corrugated mixing elements in series

for a range of pipe diameters (1 inch to 4 inches), mixer sand grain surface roughness (10 microns – 100 microns) and pipe housing roughness are reported here. Based on the results the following conclusions can be drawn:

1. Our previously proposed correlation for pressure loss across a single mixing element at high Reynolds numbers is shown to be robust enough to be applicable to multiple corrugated mixing elements across all the investigated configurations. On average, the correlation predicted all the experimental pressure loss data with a MAPE of 9.4%. In addition, the model includes separate terms for viscous and kinetic contributions enabling it to encompass a broad range of Reynolds number for its applicability.

2. Through the inclusion of the mixer tortuosity (τ), porosity (ε) and macro-scale geometric mixer wall roughness (e), the correlation not only matches historical pressure drop data (at different τ, ε) reported by other researchers but also demonstrates their utility as adjustable parameters (during the mixer manufacturing process) that can help optimize its performance. This was ascertained by employing a well validated computational fluid dynamics CFD methodology.

3. The tortuosity (τ) associated with these complex configurations were estimated from averaging the length of fluid path lines from CFD simulations. This method provides an easy way to estimate τ as an alternative to complex/prohibitive mixer geometry-based estimates.

4. Both the experiments and CFD modeling revealed that while the pressure drop per unit length (at a fixed Reynolds number) were relatively invariant to the number

of mixing elements or the mixer configuration, the rotated configuration increased the residence time by up to 13% in comparison to its aligned counterpart. This effect was more pronounced in the smaller diameter mixer configurations. This may have implications on the selective absorption of sour gas components that are based on fast kinetics. For instance, the selective absorption of H_2S (as opposed to CO_2) in caustic solution requires an optimal residence time in the range 0.01 – 0.03 seconds [50].

5. In lieu of alleviating recently reported concerns regarding the adequacy/validity of using the traditional Moody chart, measurements of pressure drop in an empty pipe were taken to estimate a sand grain roughness using the Moody chart. The estimated sand grain roughness was then provided as an input parameter in the CFD simulations of the empty pipe experiments. The pressure loss from the CFD simulations agreed to within 5% of the corresponding experimental measurements thereby ascertaining the validity of employing a single sand grain roughness to represent the loss profile across the entire pipe in the experiments. This procedure was repeated across the different pipe diameters and unique sand grain roughness values for each pipe diameter was estimated. The sand grain roughness of the different static mixers was estimated from the manufacturing process and material and also validated against CFD simulations.

6. CFD simulations showed good agreement (within about 8%) against the experimental data for all the configurations tested. The necessity of accounting for surface roughness when using CFD for predictions at lab scale was established by conducting the same simulations with and without the native sand grain

roughness. Mixing element and pipe housing roughness exhibited the largest influence on pressure loss, up to 55%, on the smaller diameter tests and at lower velocities. These results demonstrate the necessity of accounting for surface roughness (for both pipe and mixer) when utilizing lab and pilot scale data for estimating pressure losses in larger scale installations.

CHAPTER 4

Two-Phase Pressure Loss Correlation for Co-Current Flow in Corrugated Plate Static Mixers and Structured Packing[3]

Abstract

Co-current contacting of gas and liquid with a gas-continuous phase is a process with industrial relevance for natural gas processing, biogas upgrading, and carbon capture. Intensification of this process requires knowledge of wet pressure losses associated with the static mixer reactor system. There is currently a dearth of literature investigating two-phase co-current pressure loss in corrugated geometries such as static mixers and structured packing. To this end, an experimental campaign was completed to investigate multi-phase pressure loss in corrugated plate geometries under co-current flow. A correlation is developed based on the separated flow model of Lockhart & Martinelli [2] and previous work for single phase flows [62]. The new correlation is shown to provide superior predictions (overall MAPE = 17%) for multi-phase flows in corrugated plate geometries, especially for high gas Reynolds numbers and lower liquid loading. The final correlation for the two-phase pressure loss is presented as:

$$\left(\frac{\Delta P}{L}\right)_{TP} = \left[1 + \left(\sqrt{\frac{\rho_G}{\rho_L}} + \sqrt{\frac{\rho_L}{\rho_G}}\right)\chi^{0.857+1.143/\left(1+\left(Re_{c_G}/Re_{c_{G\,crit}}\right)^{5.94}\right)} + \chi^2\right]\left(\frac{\Delta P}{L}\right)_G$$

Where $Re_{c_{G\,crit}} = 24{,}920$ for the data collected in this study and $\left(\frac{\Delta P}{L}\right)_G$ is calculated from the correlation provided in previous work [62]. The model of Ishii & Gromles [74] is

---

[3] Reprinted with permission from Lowry, E. & Krishnamoorthy, G. Two-Phase Pressure Loss Correlation for Co-Current Flow in Corrugated Plate Static Mixers and Structured Packing. To be submitted to *The Canadian Journal of Chemical Engineering*.

shown to be useful for estimating the value of $Re_{c_{G_{crit}}}$ as the onset of entrainment in the corrugation channel which is idealized as a rough conduit. The critical role of entrainment onset is captured as the interfacial contribution to pressure loss and is identified as an important parametric difference between co-current and counter-current flow in corrugated geometries.

4.1   *Introduction*

Corrugated sheet geometries are commonly used for industrial mass transfer processes due to their relative ease of manufacture, high mass transfer rates, and high specific areas [15,27,75,76]. In addition to industrial structured packings (such as Sulzer Mellapak[TM]), these geometries are in use as static mixing devices, specifically when a gas-continuous phase is present [1,19]. Counter-current flow in these geometries, in which liquid flows vertically down the plates while gas flow vertically upward, has been studied at low gas Reynolds numbers very extensively. Stichlmair et al. [77] provided a correlation for wet pressure loss in counter-current flow through packed columns, including corrugated packing geometries. Rocha et al. [78] adopted a channel model approach and utilized a semi-empirical approach to correlate the wetted pressure losses in counter-current flow with corrugated packings. Brunazzi & Paglianti presented a thorough model for multiphase pressure losses in corrugated geometries in counter-current flow [79]. Their model predicted the multiphase pressure losses acceptably up to gas Reynolds numbers of about 10,000. Additionally, the study provided a correlation for liquid reversal in counter-current flow, commonly known as flooding [79].

Co-current flow occurs when both phases (gas and liquid) flow in the same direction, either vertically up or down or in a horizontal configuration. Co-current flow through structured packing and corrugated static mixers is often utilized when a reaction is taking place such as

hydro-cracking, alcohol oxidation, or hydrodesulfurization as well as acid gas removal with caustic, amine, or ferric solvent [50,80–83]. By choosing a co-current operation, chemical processes can be intensified by employing a small diameter pipe or column shell. Additionally, previous work has demonstrated very high mass transfer coefficients can be achieved using co-current operation with corrugated plate mixers or packing, often an order of magnitude higher than counter-current operation and multiple times more than monoliths or spherical packings [19,84,85].

Generally, pressure loss in multi-phase co-current flow in a conduit can be examined using two theoretical approaches: the homogenous flow [86,87], and separated flow models [88]. The separated flow model, most commonly attributed to Lockhart & Martinelli [2] who proposed its use for two-phase pipe flow, considers the flow to consist of individual single phase pressure losses that can be calculated as if each of the phases were flow alone through the geometry. Chisholm [89] provided an analytical closure to the Lockhart-Martinelli equations that included a term for interfacial pressure losses due to energy transfer between phases [90,91]. The separated flow model has been employed previously in geometries ranging from helical ribbon mixers [92] and SMX mixers [28], to random packed beds [93,94].

Despite significant effort into understanding the multiphase pressure loss in corrugated plate geometries under counter-current flow conditions, there exists no correlation in the open literature for co-current pressure loss when gas and liquid phases are present. To address this issue, an experimental study of multiphase pressure loss in corrugated plate mixers was undertaken to develop a more accurate correlation for co-current multiphase pressure loss, with specific focus on higher Reynolds numbers that are more common in field applications. The following section outlines the experimental methods used for measuring the pressure loss data.

Additionally, a theoretical approach is developed in view of previous multiphase correlations. The results are presented, along with the new correlation developed. Data from a previous study is also compared to the proposed correlation. Finally, recommendations for use of the correlation in design and potential future work directions are discussed.

4.2   Methods

4.2.1   Experimental System

To measure the experimental multiphase gas-liquid pressure loss variables across static mixing systems, a flow system was constructed. The system was designed to operate with compressed air up to a pressure of 120 psig. Air flow (at 110 psig) was supplied by a 150 HP air compressor with a 1,000 gal pressure vessel. All process piping was composed of schedule 40 stainless steel in 1-inch nominal sizing. A pipe run of 24 inches was allowed after the inlet valve to allow the flow to fully develop prior to measuring the flowrate using a cylindrical averaging differential pressure probe. The differential pressure gauges for the flowmeter and measurement section were acquired from Alicat Scientific, Inc. (Tuscon, AZ, USA) and have a calibrated accuracy of 0.2% across the entire range of Reynolds numbers. A computer data acquisition system was used to log the data from the differential pressure meters. The system could produce maximum velocities of around 30 m/s in the 1-inch empty pipe configuration (Re of 440,000). The piping configuration was constructed to allow the measurement section to be switched to a 2-inch nominal pipe run for measurements in a larger diameter. For all tests, a pipe run of at least 10 pipe diameters was placed before the start of the measurement section to allow for flow development. Table 4.1 provides the range of experimental conditions. The ranges of liquid and

gas rates were chosen to approximate, as much as possible, ranges experienced in the field. For

example, operating field H_2S scavenger installations can operate between $Re_L = 5 - 1000$ [95].

Table 4.1. Range of experimental conditions for two-phase pressure loss measurements

Variable	Range
Gas Velocity (m/s)	1 – 26
Liquid Rate (mL/min)	10 – 690
Gas Density (kg/m3)	11 – 2.3
Pipe Diameter (in)	1 – 2
Number of Mixing Elements	1 – 5
Re_G	3,065 - 320,400
Re_L	9 - 590

The liquid injection was accomplished using a positive displacement piston pump with

pulseless flow which introduced the liquid into the gas flow via an injection quill placed at the

centerline of the pipe. The quill was positioned 5 pipe diameters upstream of the mixer(s) and

differential pressure measurements we obtained before and after the mixing elements. Figure 4.1

shows the cross-sectional drawing view of the experimental system for 1-inch mixing elements.
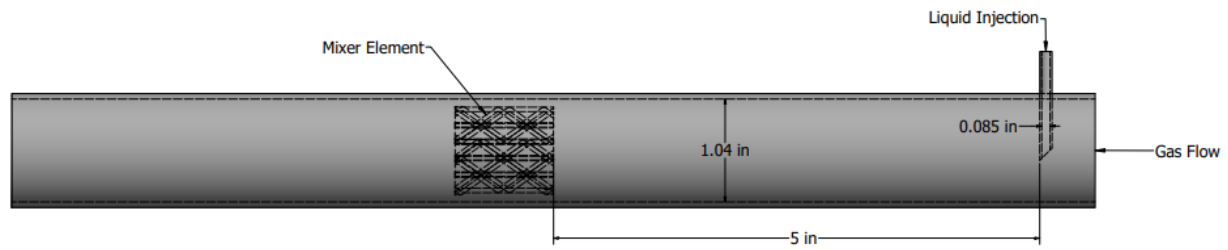
Figure 4.1. Cross-sectional side view of the experimental system for 1-inch test element

4.2.2 *Static Mixer Geometry*

The static mixers were fabricated from stainless steel and designed to fit inside the 1- and 2-inch pipe housings used in the experimental system. A variety of configurations were tested including multiple mixers in series to obtain an average pressure loss per unit length for the mixing elements under multiphase flow conditions. Previous study has shown minimal difference in pressure loss per unit length with variation in rotational orientation of mixers in series. Each mixer element is characterized by channels that are oriented at 45 degrees relative to the pipe axis. An equivalent hydraulic diameter of the mixer channel may be defined (D_c) based on the perimeter of a single mixing channel as in Equation 4.1 and illustrated in Figure 4.2.

$$D_c = \frac{P}{\pi} \qquad\qquad 4.1$$

Additionally, each mixer possesses an intrinsic void fraction (ϵ) and tortuosity (τ) which define the flow characteristics of the mixer [62]. The characteristics for the mixing elements used in this study are given in Table 4.2.
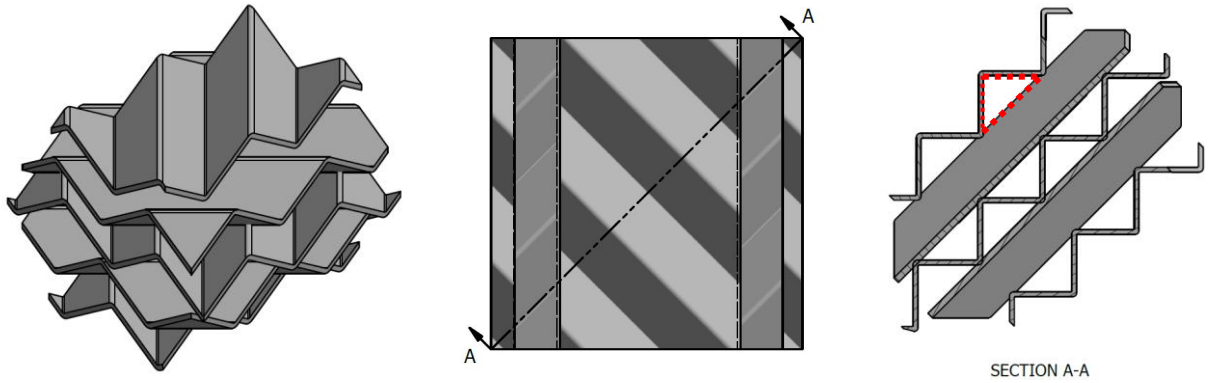
Figure 4.2. 3D CAD rendering of the corrugated mixers used for experimental measurements. The red dashed lines denote the perimeter (P) of one channel used for determination of the mixer channel hydraulic diameter

Table 4.2. Experimental Mixer Element Conditions

D (in)	L/D	ε	τ	D_c (in)	K_s (micron)
1	1	0.756	1.32	0.126	10
2	1	0.879	1.29	0.315	10

4.2.3   Computational Fluid Dynamics (CFD) Methods

Computational fluid dynamics (CFD) simulations were conducted with a multi-phase model to ascertain the accuracy for predicting two-phase pressure loss. A single mixing element was simulated using a mesh that was generated in a previous study and shown to reproduce single-phase experimental data [62]. Ansys Fluent version R2021 was used for conducting the simulations and analyzing the data. The discrete phase model (DPM) was chosen to represent the liquid phase. The DPM approach treats liquid droplets as particles with a defined diameter, mass,

and velocity, from which the appropriate momentum source terms are generated and transferred to the gas phase. The droplets were injected at the inlet of the domain into an area equivalent to the injector quill cross-section as shown in Figure 4.1. A fixed mass flow of liquid was specified for each simulation as well as a gas velocity at the inlet. The gas and liquid properties were chosen to match the average experimental properties. Droplets were tracked in a steady-state fashion every 50 iterations of the continuous phase. The standard spherical drag force model was applied to the droplets and the droplet diameter was fixed uniformly for all droplets. A parametric study of the impact of injected droplet size was conducted by varying the size from 25 microns to 1000 microns. At higher Reynolds numbers, the droplet size had less than 5% impact over the droplet size range. At low Reynolds number, the impact of droplet size reached 27%. Based on the results of the droplet size evaluation, 100-micron droplet size was chosen for the final simulations.
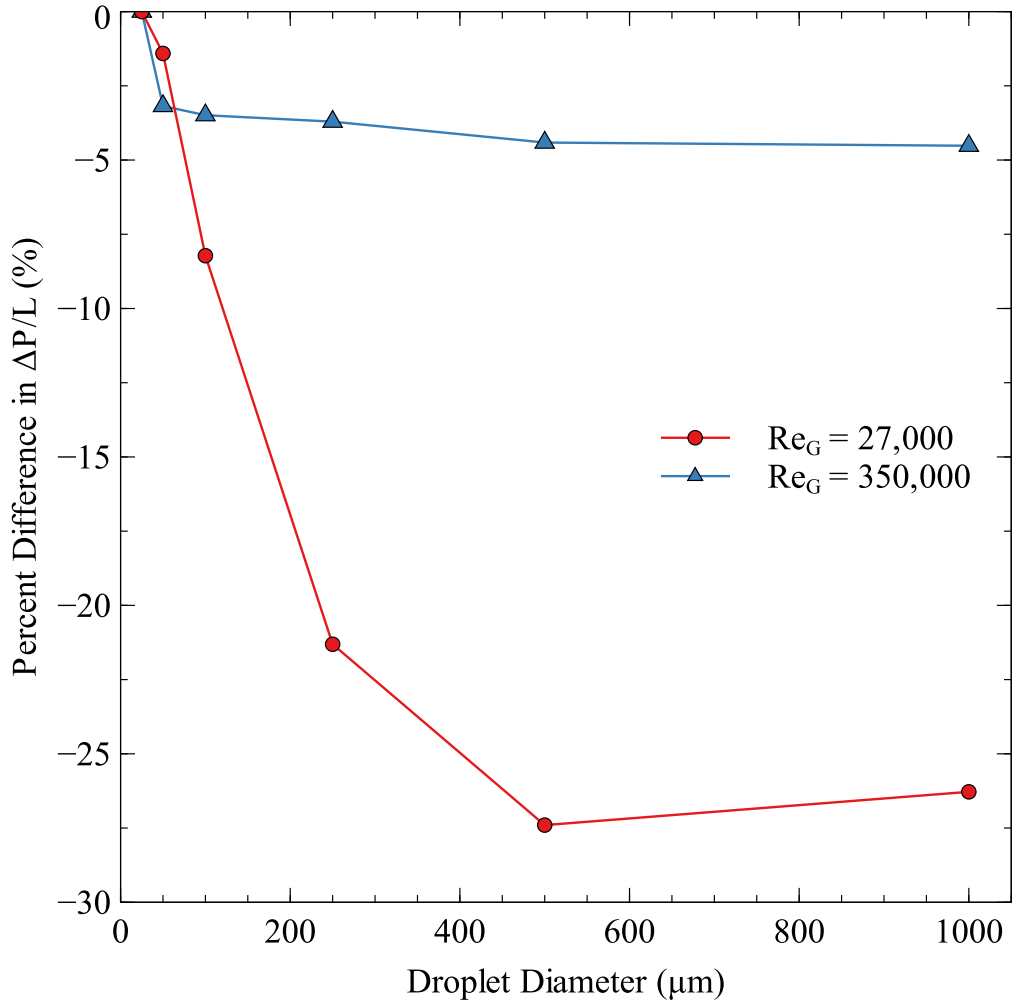
Figure 4.3. Change in ΔP/L with different droplet sizes relative to the differential pressure with 25-micron droplet size

The walls of the mixer and pipe were calculated as ideal reflecting surfaces for the droplet phase and no droplets were absorbed by the surface. The pressure loss across the mixer was calculated by taking an average pressure slice across the domain before and after the mixer once the simulation had converged as determined by the stabilization of the inlet pressure.

4.2.4   Experimental Correlation

Previously, a correlation for single-phase flow in corrugated static mixers was developed [62]. Utilizing a frictional loss coefficient defined in terms of the mixer channel, an expression can be obtained for the total viscous and kinetic losses through the mixer in single-phase flow (**Error! Reference source not found.**-**Error! Reference source not found.**).

$$\frac{\Delta P}{L} = \frac{2f_c \rho u_0^2 \tau^3}{D_c \epsilon^2} \qquad\qquad 4.2$$

$$f_c = \frac{36}{Re_c} + 0.0826 \qquad\qquad 4.3$$

$$Re_c = \frac{\rho u_0 \tau D_c}{\epsilon \mu} \qquad\qquad 4.4$$

In multiphase flow, the losses associated with both phases must be accurately captured, in addition to any inter-phase energy transfer that takes place. Given that the mixer geometry is complex, it is a reasonable assumption that inter-phase energy transfer is not negligible and will likely impact the overall two-phase pressure loss in gas-liquid flow.

Due to the generalizable nature of pipe flows, much of previous literature has centered on prediction of two-phase pressure loss in these conduits. Although many models have been posited, there are two major model philosophies that have been reasonably successful at capturing the relevant physics associated with gas-liquid pipe flow. The homogeneous model, originally proposed by McAdams [86], assumes that the gas and liquid phases flow in the pipe or channel at the same velocity. This model has been expanded by many including the widely used

model of Dukler et al. [87]. A second method for pressure loss prediction was developed by

Lockhart & Martinelli [2,96] and later an analytical closure of the equations was provided by

Chisholm [89]. The model decomposes the pressure loss into components consisting of the

liquid-only, gas-only, and interfacial pressure loss terms. A two-phase multiplier is utilized to

correct the single-phase flow pressure loss and provide an accurate determination of the two-

phase pressure loss. The form of the two-phase pressure loss equation adapted from Chisholm

[89] is given by Equation 4.5.

$$\left(\frac{\Delta P}{L}\right)_{TP} = \left(\frac{\Delta P}{L}\right)_G + C\left(\left(\frac{\Delta P}{L}\right)_L \left(\frac{\Delta P}{L}\right)_G\right)^{\frac{1}{2}} + \left(\frac{\Delta P}{L}\right)_G \qquad 4.5$$

The subscripts of G and L represent the gas-only and liquid-only pressure losses which

are calculated by assuming flow through the conduit of either phase at its individual superficial

velocity. The constant, C, and the square root term encompasses the losses associated with

energy transfer between phases. The calculation of the two-phase pressure loss is determined via

the Martinelli parameter defined by Equation 4.6.

$$\chi = \sqrt{\frac{\Delta P_L}{\Delta P_G}} \qquad 4.6$$

Subsequently, the two-phase frictional pressure loss multipliers may be defined via

Equation 4.7.

$$\phi_L^2 = \frac{(\Delta P/L)_{TP}}{(\Delta P/L)_L}, \quad \phi_G^2 = \frac{(\Delta P/L)_{TP}}{(\Delta P/L)_G} \qquad 4.7$$

Muzychka & Awad provided a generalized closure for Equation 4.5, similar to the

Chisolm [89] formulation, that allows for the interfacial contribution to be manipulated based on

experimental data via Equation 4.8 [91].

$$\phi_L^2 = \left(1 + \frac{C}{\chi^m} + \frac{1}{\chi^2}\right), \qquad \phi_G^2 = (1 + C\,\chi^m + \chi^2)$$

4.8

From this, the two-phase total pressure loss follows mathematically as Equation 4.9.

$$\left(\frac{\Delta P}{L}\right)_{TP} = \phi_L^2 \left(\frac{\Delta P}{L}\right)_L = \phi_G^2 \left(\frac{\Delta P}{L}\right)_G$$

4.9

The separated flow model of Equation 4.5 provides the flexibility to adjust the interfacial

contribution to accurately account for the flow physics. In the original Chisholm model, $m = 1$

and C takes on values of either 20 for turbulent gas and turbulent liquid or 12 for turbulent gas

and laminar liquid flow. As such, this model is well suited for two-phase flow in static mixing

devices, where the interfacial contributions are more likely to be non-negligible. Indeed, this

method has been used for static mixing devices in gas-liquid flow with success in previous

studies [1,20,28,92]. We adopt here this separated flow model for fitting and correlating the data

in the current study.

Utilizing the semi-analytical correlation of Equation 4.2, the individual phase-only

pressure losses can be calculated by utilizing the superficial phase velocity and phase properties.

Equation 4.10 provides the requisite definition of the phase friction factor where subscript i

represents the phase (i.e. gas or liquid).

$$f_{c_i} = \frac{36}{Re_{c_i}} + 0.0826$$

4.10

The phase Reynolds number inside the mixing element channel (which is idealized as a conduit) can be expressed in Equation 4.11.

$$Re_{c_i} = \frac{\rho_i u_{i_0} \tau D_c}{\epsilon \mu_i} \quad \text{where } u_{i_0} = \frac{\dot{m}_i}{\rho_i A_{pipe}}$$

4.11

$$\left(\frac{\Delta P}{L}\right)_i = \frac{2 f_{c_i} \rho_i u_{i_0}^2 \tau^3}{D_c \epsilon^3}$$

4.12

From this, the pressure loss for the gas and liquid phase alone flowing in the mixer channel can be calculated using Equation 4.10 and Equation 4.12. The Martinelli parameter and the two-phase frictional loss multipliers are calculable using the equations presented before. Finally, the C and m parameters controlling the interfacial pressure loss in Equation 4.8 may be fit from the experimental data.

The total experimental dataset utilized for fitting the parameters for the correlation consisted of 1,250 points taken over a range of $130 < Re_{c_G} < 58{,}000$ and $2 < Re_{c_L} < 133$. In terms of the pipe Reynolds numbers, these ranges are $3{,}300 < Re_G < 2.6 \times 10^5$ and $9 < Re_L < 641$. For fitting the dataset, the expression for C provided by Whalley (Equation 4.13) was adopted [97].

$$C = \sqrt{\frac{\rho_G}{\rho_L}} + \sqrt{\frac{\rho_L}{\rho_G}}$$

4.13

For correlating the power-law parameter m, other authors have suggested various values. Sun & Mishima presented the correlation of Equation 4.14 based on the original Chisholm model.

$$\phi_G^2 = 1 + \left(1.79 \left(\frac{Re_{c_G}}{Re_{c_L}}\right)^{0.4} \left(\frac{1-x}{x}\right)^{0.5}\right) \chi^{1.19} + \chi^2 \qquad \text{4.14}$$

Other values of m have been utilized in the literature and are reviewed in detail by Awad [90]. Muzychka & Awad suggest that for complicated flow scenarios m should be an adjustable parameter that functionally depends on the flow regime and phase Reynolds numbers [91]. Indeed, they found that the gas two-phase multiplier (ϕ_G^2) from the data of Lockhart & Martinelli [2] was fit by $m > 1$ for lower Reynolds number flows and observed that m decreased with increasing gas Reynolds number. Based on the experimental data in this study, m was found to depend primarily on the gas phase Reynolds number in the mixer (cf. Equation 4.11). The functional relationship provided in Equation 4.15 was determined to provide the best fit for the entire dataset while minimizing the overall prediction errors.

$$m(Re_{c_G}) = m_{max} + \frac{m_{min} - m_{max}}{1 + \left(\frac{Re_{c_G}}{Re_{c_{G\,crit}}}\right)^n} \qquad \text{4.15}$$

In Equation 4.15, the parameter $Re_{c_{G\,crit}}$ represents the critical gas-phase Reynolds number at which interfacial energy transfer begins to become a dominant term in the total pressure loss. Intuitively, this occurs when the liquid ceases to form stable films on the mixer plate surface and begins to be entrained into the gas flow at a high rate in the form of droplets. The entrainment phenomena is well studied in annular gas-liquid flows in pipes [74,98–100].

Treating the mixer channel as a rough conduit, analogous to a pipe, the model of Ishii & Grolmes is useful for estimating the onset of entrainment [74]. The liquid film Reynolds number in the mixer channel and the viscosity number can be defined by Equation 4.16 and Equation 4.17.

$$Re_{c_{film}} = \frac{4\rho_L Q_L (D_c/D_{pipe})}{\mathcal{P}\mu_L}$$

$$\qquad\qquad 4.16$$

$$N_\mu = \frac{\mu_L}{\left(\rho_L \sigma \sqrt{\frac{\sigma}{\Delta\rho g}}\right)^{0.5}}$$

$$\qquad\qquad 4.17$$

Where Q_L is the volumetric liquid flowrate being injected into the pipe and $\mathcal{P}$ is the perimeter of a single mixer channel (cf. Figure 4.2). For film Reynolds numbers below 1,635, the criteria for inception of entrainment in a conduit is given by Equation 4.18.

$$\begin{cases} u_{G_s} \geq \left(\frac{\sigma}{\mu_L}\right)\sqrt{\frac{\rho_L}{\rho_G}}\left(11.78\, N_\mu^{0.8} Re_{c_{film}}^{-\frac{1}{3}}\right); & \text{for } N_\mu \leq \frac{1}{15} \\[2ex] u_{G_s} \geq \left(\frac{\sigma}{\mu_L}\right)\sqrt{\frac{\rho_L}{\rho_G}}\left(1.38\, Re_{c_{film}}^{-\frac{1}{3}}\right); & \text{for } N_\mu > \frac{1}{15} \end{cases}$$

$$\qquad\qquad 4.18$$

For full turbulent flows, defined as film Reynolds numbers above 1,635, the inception criteria is defined by Equation 4.19.

$$\begin{cases} u_{G_s} \geq \left(\frac{\sigma}{\mu_L}\right)\sqrt{\frac{\rho_L}{\rho_G}}\, N_\mu^{0.8}; & \text{for } N_\mu \leq \frac{1}{15} \\[2ex] u_{G_s} \geq 0.1146\left(\frac{\sigma}{\mu_L}\right)\sqrt{\frac{\rho_L}{\rho_G}}; & \text{for } N_\mu > \frac{1}{15} \end{cases}$$

$$\qquad\qquad 4.19$$

In Equation 4.18 and Equation 4.19, the variable u_{G_s} is the gas superficial velocity through the mixer channel at which entrainment begins to occur. Using this correlation, the mixer channel gas-phase Reynolds number was calculated for all the experimental data points. The statistical results are shown in Figure 4.4. The mean Re_{c_G} at which liquid entrainment was predicted to occur was $Re_{c_G} = 24,920$.
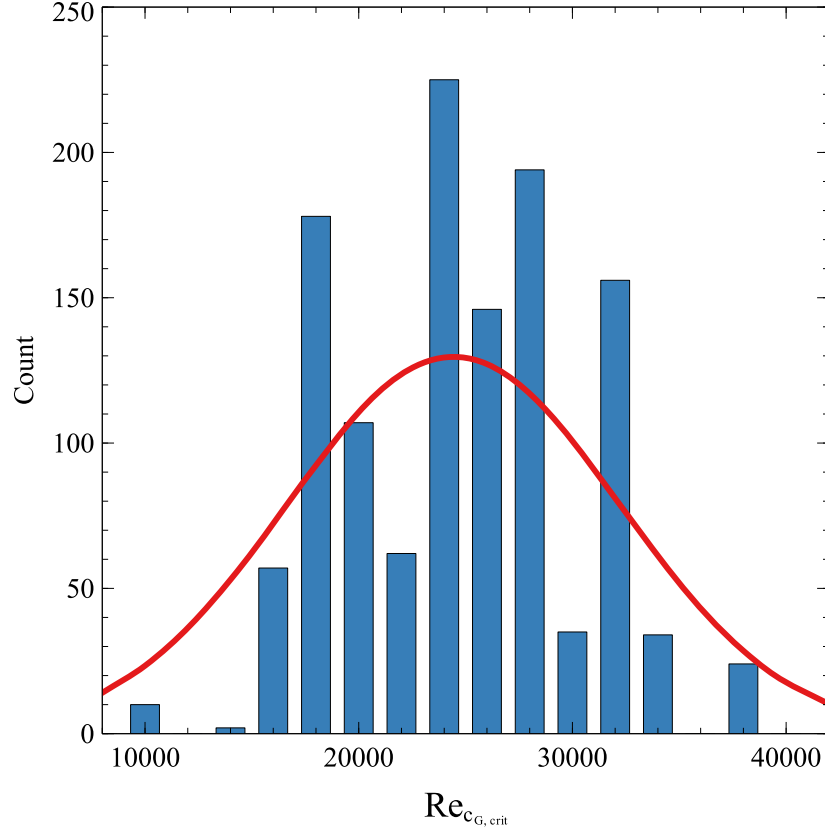
Figure 4.4. Critical gas Reynolds number for entrainment in mixer channel calculated for all data points in this study based on criteria of Ishii & Grolmes [74]

Utilizing the findings of Figure 4.4 to inform the fitting process, the expression for m based on fitting the experimental data in this study is provided in Equation 4.20.

$$m(Re_{c_G}) = 0.857 + \frac{1.143}{1 + \left(\frac{Re_{c_G}}{24,920}\right)^{5.94}}$$
4.20

Utilizing the expression for m in Equation 4.20 and the expression for C provided in Equation 4.13 the two-phase frictional multiplier can be calculated via Equation 4.8. The individual phase-only pressure losses are calculated via the modified mixer channel equations (cf. Equation 4.10). Finally, the predicted two-phase pressure loss may be calculated by using

Equation 4.9. The final form of the correlation expressed in terms of the gas-phase two-phase pressure loss multiplier is given by Equation 4.21.

$$\left(\frac{\Delta P}{L}\right)_{TP} = \left[1 + \left(\sqrt{\frac{\rho_G}{\rho_L}} + \sqrt{\frac{\rho_L}{\rho_G}}\right)\chi^{0.857+1.143/\left(1+\left(Re_{cG}/Re_{cG_{crit}}\right)^{5.94}\right)} + \chi^2\right]\left(\frac{\Delta P}{L}\right)_G \qquad 4.21$$

Where $Re_{cG_{crit}} = 24{,}920$ for the data collected in this study as noted previously and $\left(\frac{\Delta P}{L}\right)_G$ is calculated via Equation 4.12.

4.3   Results

4.3.1   Experimental Correlation

Several models were evaluated against the data collected in this study. The traditional Chisholm model with $C = 20$ and $C = 12$ [89]. Additionally, the models of Whalley [97] as well as Sun & Mishima [101] were evaluated. Finally, the single-phase gas model presented in previous work by the authors was compared [62]. Most of the previous literature models were able to capture the low Reynolds number flow with a MAPE of less than 15% (cf. Table 4.3). However, above the entrainment inception point, most previous literature models diverged significantly from the experimental data as in Figure 4.5. Collected data for multiphase pressure loss in 1-inch SMV-style mixers (black circles) compared to existing correlations and the correlation of this study. We postulate that the main reason that previous models struggle to accurately account for the high Reynolds number regime in corrugated static mixers is the increased contribution of the interfacial terms at high Reynolds numbers.

Table 4.3. Mean absolute percentage error (MAPE) for total experimental dataset with respect to previous literature models and the model presented in this study

Model	MAPE (%)	MAPE (%), $Re_{C_G} > 25$k	MAPE (%), $Re_{C_G} < 25$k
Chisholm, $C = 20$ [89]	65	95	11
Chisholm, $C = 12$ [89]	45	62	15
Whalley (1996) [97]	40	54	15
Sun & Mashima (2009) [101]	23	24	21
Lowry & Krishnmoorthy (2022) [62]	22	21	22
This Model	17	7	23
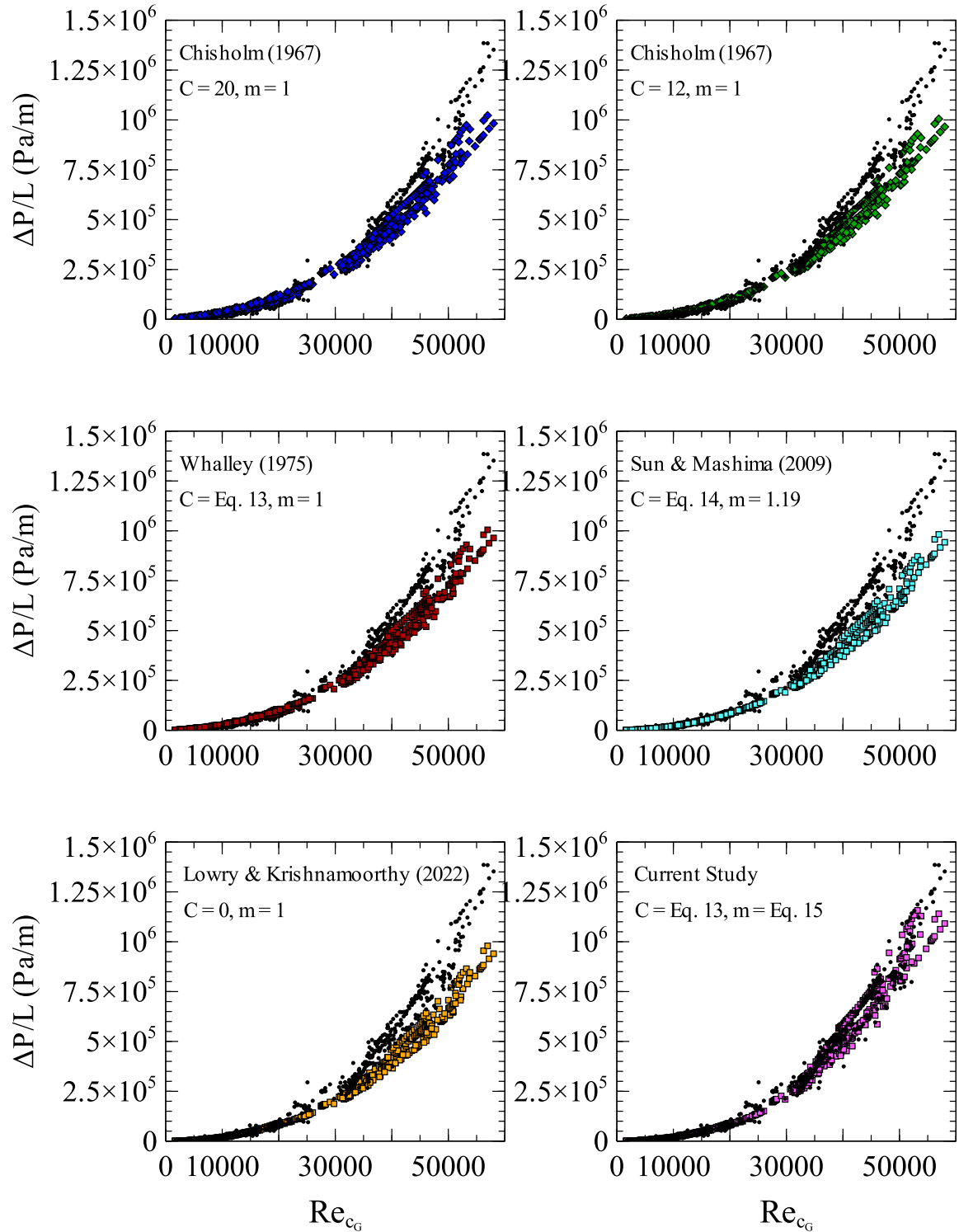
Figure 4.5. Collected data for multiphase pressure loss in 1-inch SMV-style mixers (black circles) compared to existing correlations and the correlation of this study

The proposed correlation appears to capture the total pressure losses in the static mixers for both horizontal flow and vertical down-flow configurations. Intuitively, if the liquid Reynolds number was to be much higher than the range investigated in this study, one may expect that the observed pressure losses would diverge from the predictions of the correlation in this study. The additional gravitational head induced by the liquid in a vertical configuration would likely become significant for high liquid Reynolds numbers. In design practice, Paul et al. [1] suggest that the vertical configurations be chosen when the mixture Froude number (Equation 4.22) is less than 20.

$$Fr_c = \frac{\rho_G u_{G_0}}{(\rho_L - \rho_G)D_c g}$$
4.22

Similar fit quality was observed across the diameters tested in this study. As shown in Figure 4.7, the 2-inch static mixer pressure losses were captured well at two different liquid Reynolds numbers. The predictions were slightly lower than the data at low gas Reynolds numbers.

Based on a survey of the existing literature, there is very little two-phase pressure loss data in corrugated plate mixers or structured packings under *co-current* flow conditions. The data of Couvert et al. [19] was the only dataset similar to this study. As can be seen in **Error! R eference source not found.**, the correlation in this study predicted the pressure loss data reported by Couvert et al. [19] with reasonable accuracy.
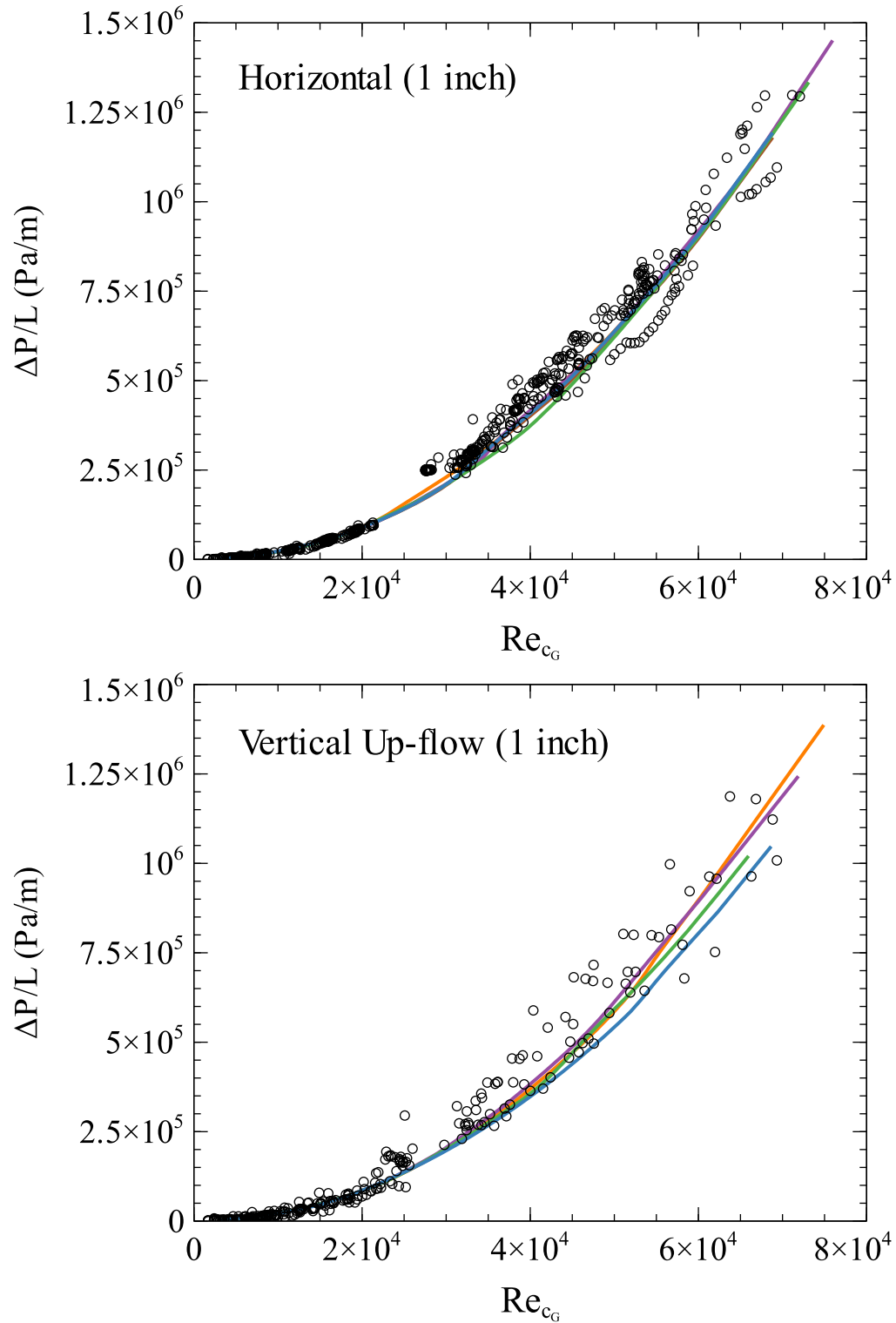
Figure 4.6. Experimental two-phase pressure loss data (circles) at $10 < Re_{c_L} < 133$ for 1 inch corrugated mixers in both horizontal and vertical down-flow. Correlation of this study is shown as lines
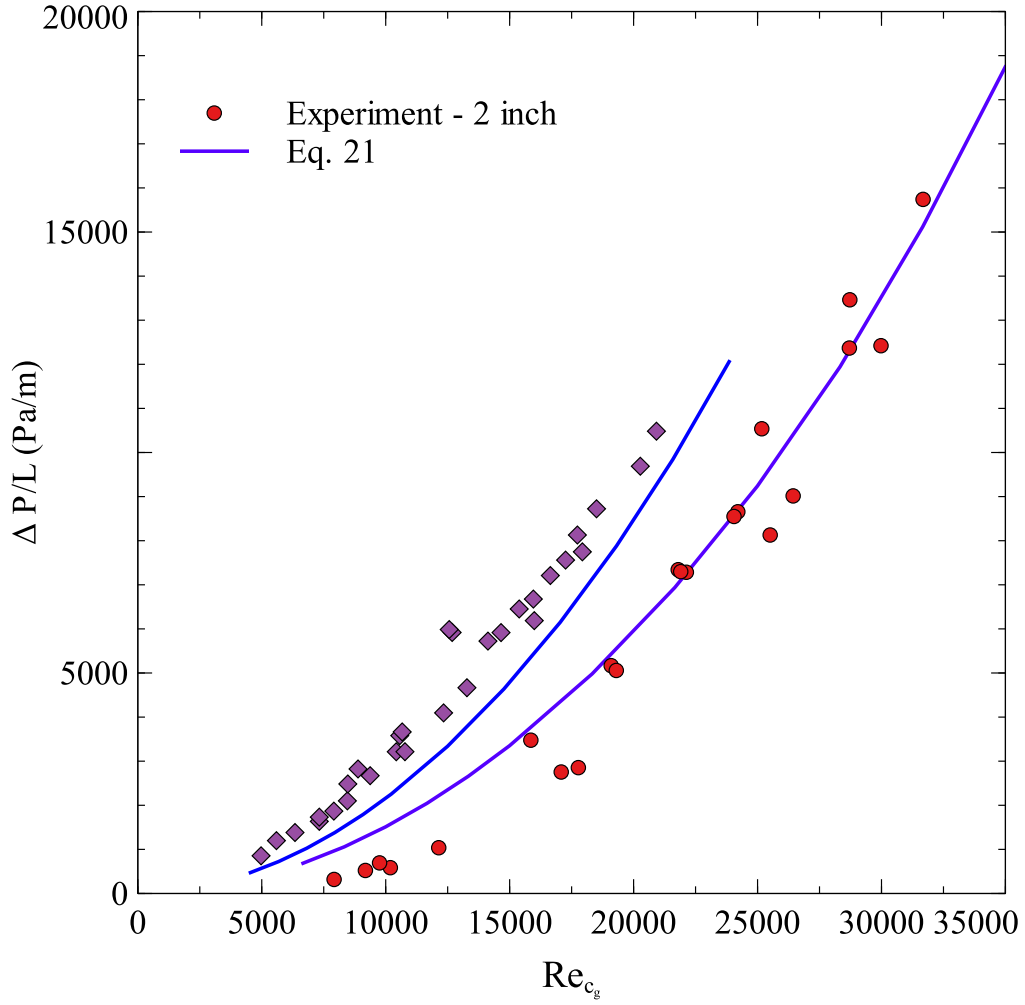
Figure 4.7. Experimental data for two-phase pressure loss in 2-inch corrugated mixers for $Re_{c_L} = 10$ (red circles) and $Re_{c_L} = 67$ (purple diamonds)
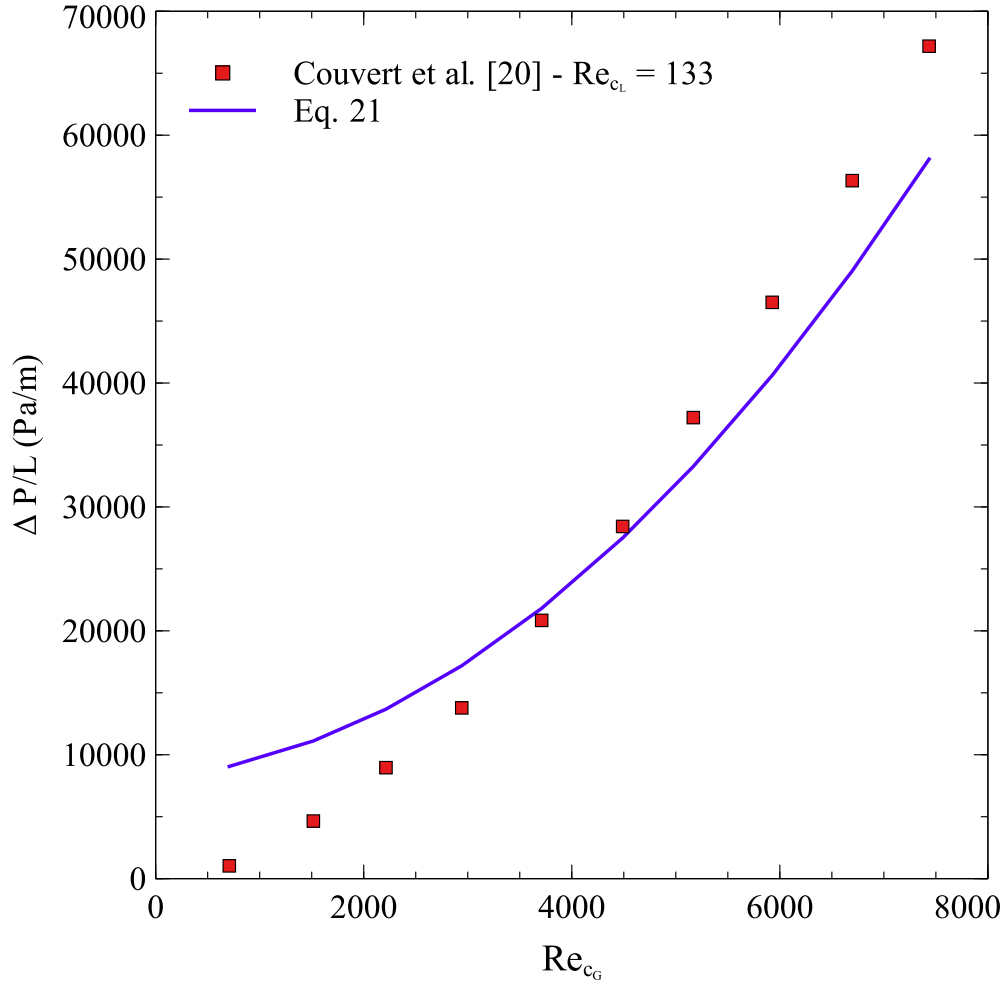
Figure 4.8. Experimental data from Couvert et al. [19] for 1-inch corrugated mixing elements at $Re_{c_L} = 133$ (red squares) and the correlation of this study

Figure 4.9 shows the relative contributions of the gas, liquid, and interfacial pressure losses based on the correlation of this study. At the lower liquid and gas Reynolds numbers, the error introduced by assuming single-phase gas flow is generally less than 10%. The contribution of the interfacial term and the liquid term increases with increased liquid loading. This phenomenon is analogous to the drastic impact of liquid load on pressure loss in structured packing columns. At high gas Reynolds numbers and increasing liquid Reynolds numbers, the liquid entrainment and holdup increase rapidly in a counter-current structured packing system at the point where liquid reversal occurs [17,29]. In counter-current flow, once the gas momentum can provide very large liquid holdups, the pressure drop rises rapidly. Several authors have noted that this often occurs at pressure loss ranges defined by Equation 4.23 [77,102].

$$0.1 \leq \frac{\left(\frac{\Delta P}{L}\right)_{flood}}{\rho_L g} \leq 0.3 \qquad\qquad 4.23$$

By contrast, under co-current flow conditions, flooding cannot occur since the liquid holdup reaches a maximum prior to the gas momentum overcoming the interfacial forces and entraining the liquid as droplets, which are then transported downstream. This is likely why the entrainment onset Reynolds number (cf. Equation 4.20) is a rational parameter for estimating the point at which the interfacial pressure losses begin to contribute to the overall pressure loss terms. Based on this theoretical consideration, one anticipates that co-current and counter-current multiphase flow systems would have similar pressure loss profiles (other than gravitational effects) up to the counter-current flooding point, at which the counter-current system pressure loss increases asymptotically to infinite value. Additionally, this provides a theoretical explanation for the asymptotic constant behavior of the interfacial contribution in co-current flow once the entrainment process has started inside the corrugation channels (cf. Figure 4.7).
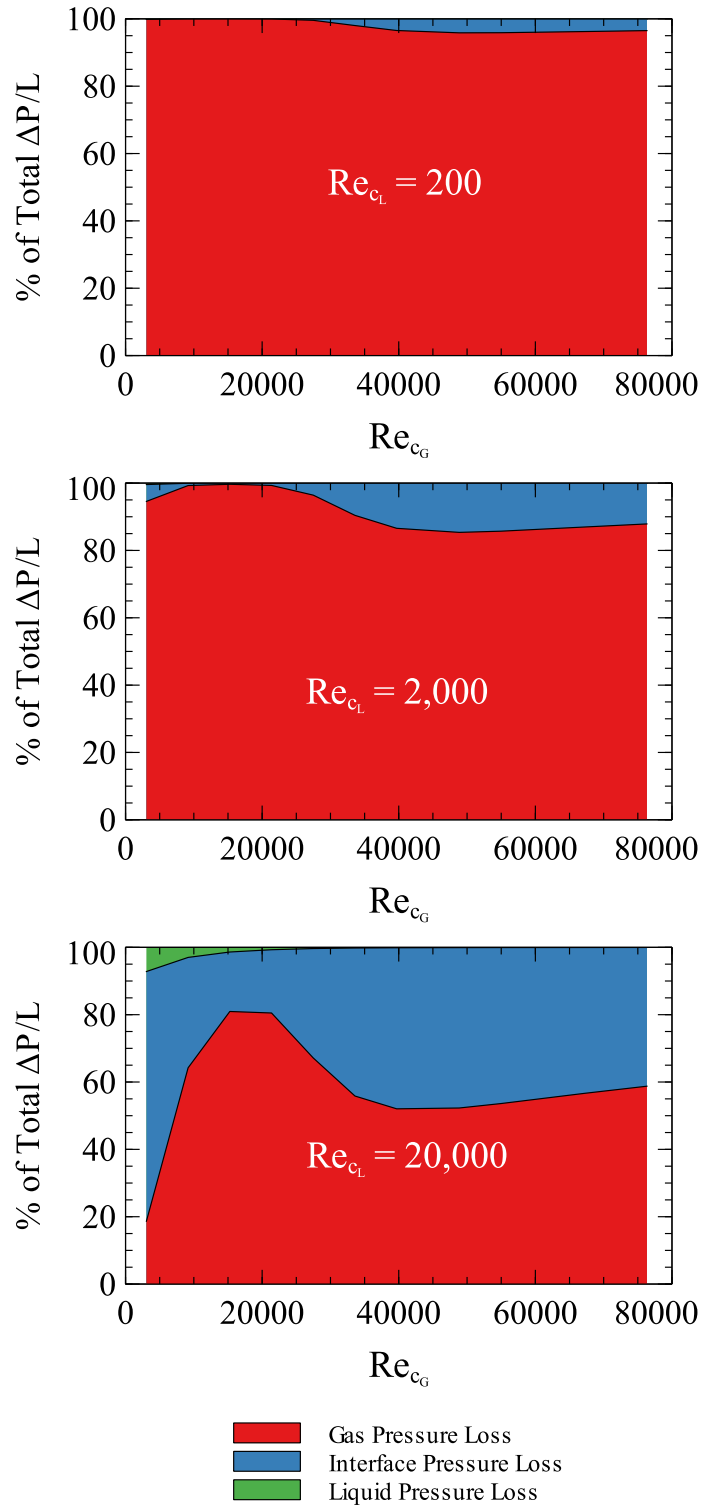
Figure 4.9. Contribution of liquid, gas, and interfacial pressure losses as calculated by the correlation in this study at varying gas and liquid Reynolds numbers.

4.4   CFD Simulations

The two-phase pressure loss was calculated from CFD simulations as described in previous sections. The discrete phase wall interaction was handled by the reflecting model which appears to have captured the relevant pressure loss well. Figure 4.10 shows that the CFD simulation was able to capture the increase in pressure loss with increasing liquid Reynolds number in the 1-inch mixer. As would be expected, the CFD predictions were most accurate at $Re_{c_G} > 25,000$ or $Re_G > 110,000$ and $Re_L < 85$. At higher gas Reynolds numbers, the liquid would likely remain predominantly in droplet form, making the discrete phase model a better approximation at these conditions. At lower Reynolds numbers, a liquid film would form on the surface of the mixer and impart much less drag on the gas phase. This explains why the single-phase pressure loss model appears to provide a decent approximation at lower gas Reynolds numbers.

As shown in Figure 4.11, the CFD model could match the experimental data well at low liquid loads. At $Re_L = 590$, the discrete phase model with reflecting wall conditions could not accurately capture the multiphase pressure loss. This could be due to more complex interactions between the liquid and the mixer wall such as film flow and entrainment. Further study is warranted into alternative CFD models for high liquid loads at high gas Reynolds numbers.
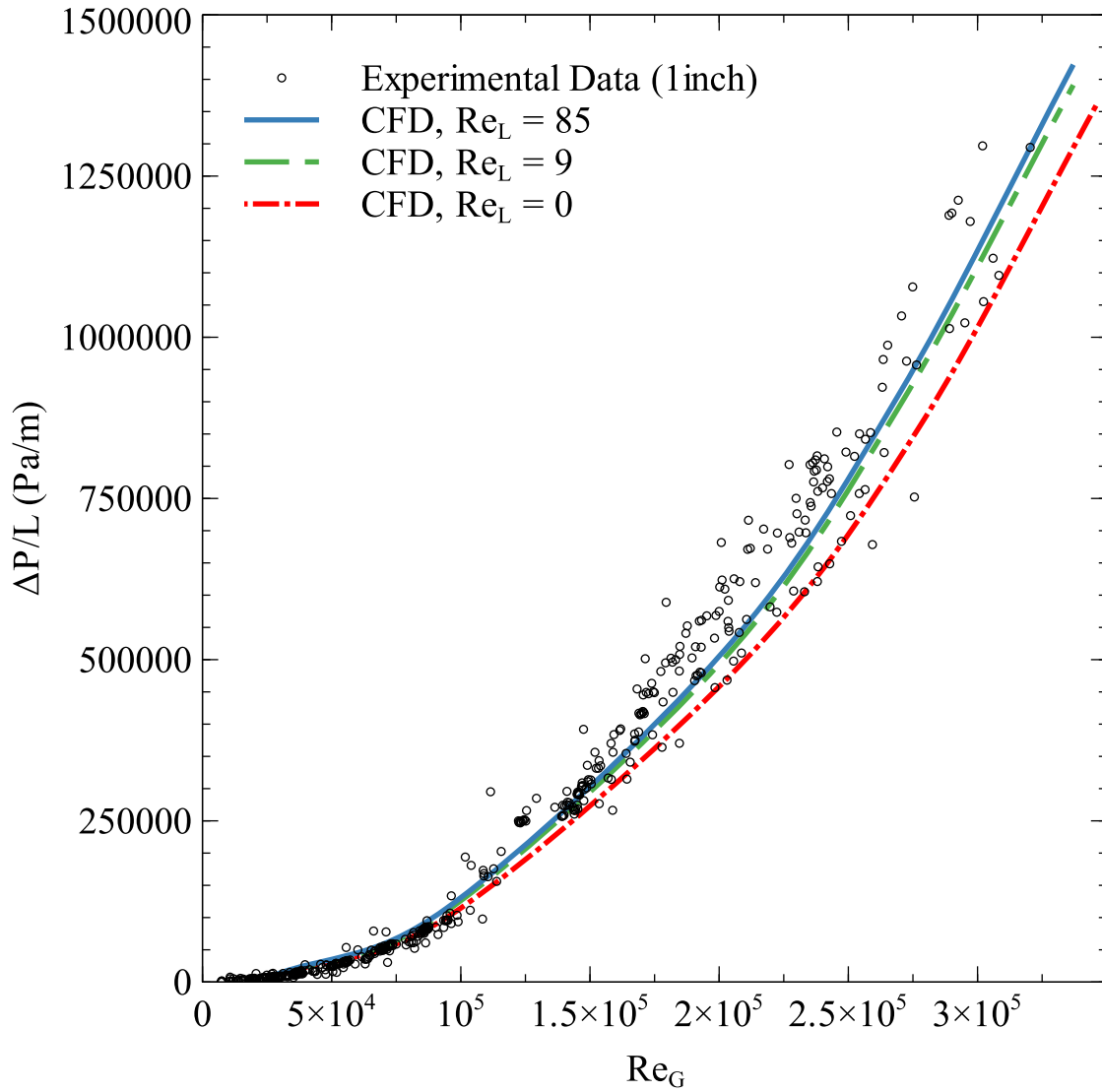
Figure 4.10. Two-phase pressure loss results with gas/liquid CFD simulations. Note that the results are shown in terms of the gas Reynolds number for the pipe (not mixer channel).
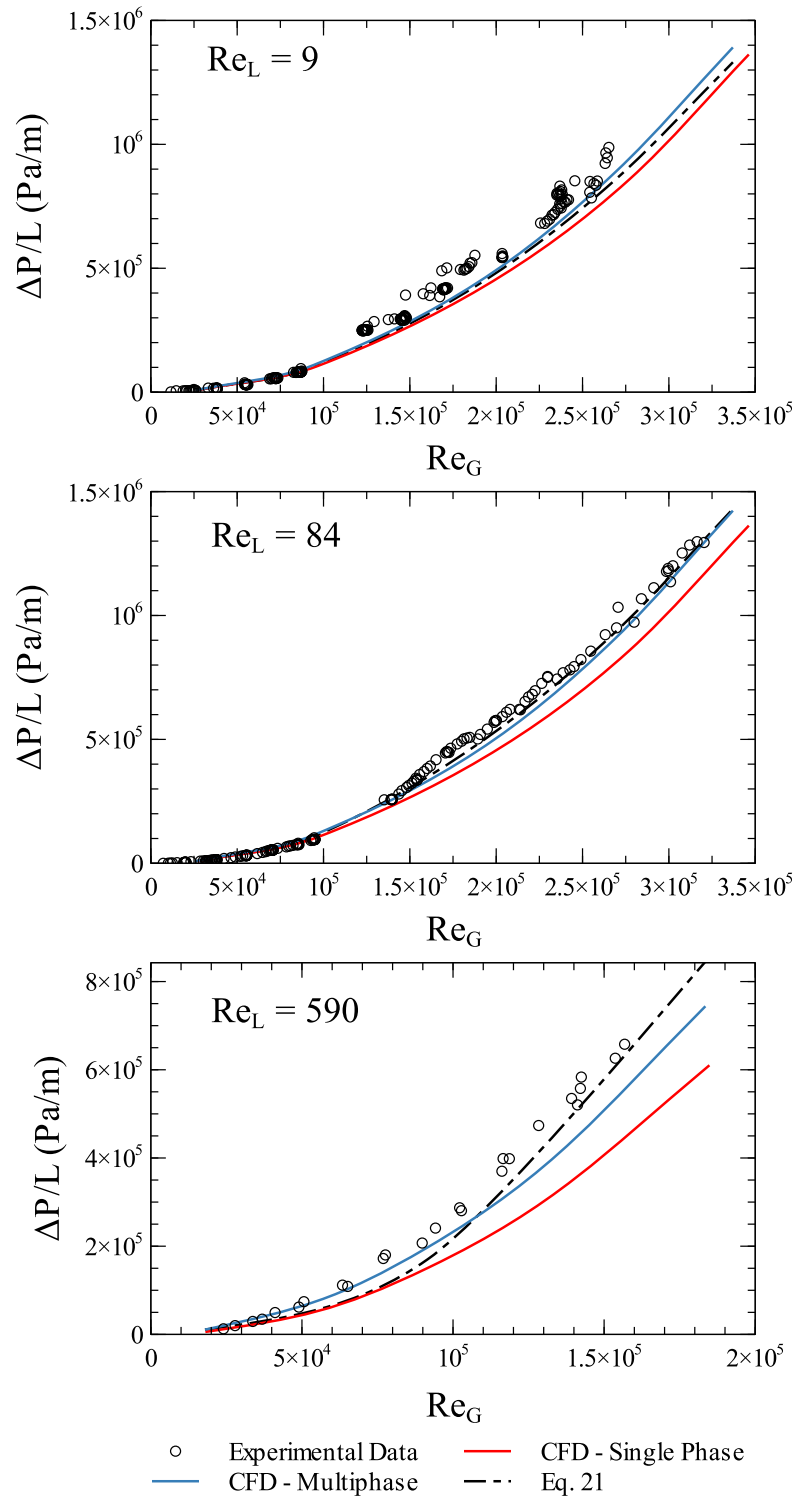
Figure 4.11. Individual datasets for multiphase flow in 1-inch mixers at various liquid Reynolds numbers. Note that the results are shown in terms of the gas Reynolds number for the pipe (not mixer channel).

114

4.5   Conclusions

Corrugated plate elements are commonly utilized in the process industry for static mixing in turbulent flow and for column packings. These geometries are especially useful for mass transfer with a gas continuous phase due to their high specific surface area and large mass transfer coefficients. Two-phase operation in co-current flow (as opposed to counter-current) is advantageous in many situations and can be used to intensify gas-liquid reactive processes. Unfortunately, current literature models are only accurate for counter-current flow at low gas Reynolds numbers. To expand knowledge in this area, an experimental study was conducted to measure multiphase pressure loss in co-current flow through corrugated plate mixing elements at high gas Reynolds numbers. Existing multiphase pressure loss correlations were unable to match the pressure loss data, especially at high Reynolds numbers.

A new correlation is proposed which matched the data better than existing correlations formulated for pipe flow or single-phase flow (MAPE = 17%). The proposed correlation utilizes the separated flow model of Lockhart & Martinelli along with single phase correlations developed in previous work. An interfacial factor is introduced that considers entrainment effects inside the mixer that are present in co-current flow but not in counter-current flow. Future work may include investigation of mass transfer in co-current flow and possible interplay between the pressure loss and interfacial area.

Computational fluid dynamics (CFD) simulations were able to produce good results that matched the experimental data despite the use of a simplified discrete phase model with constant droplet diameter and reflecting walls. Predictions appeared to be less accurate above $Re_L = 84$ and at higher gas Reynolds number ($Re_G > 110,000$). Overall, the results support the use of

CFD with a simple discrete phase model as a design tool to estimate multiphase pressure loss in static mixers.

In summary the key findings of this study are:

- Current literature correlations for corrugated style static mixers and structured packing may not accurately predict multiphase pressure losses at high Reynolds numbers.

- The interfacial contribution to the multiphase pressure loss is postulated to increase with gas Reynolds number and correlates well with the Reynolds number when entrainment begins to occur in the mixer channel

- A new correlation based on the separated flow model of Lockhart & Martinelli is developed to fit the experimental data with the aim of creating an accessible and intuitive formulation for the multiphase pressure loss

- CFD simulations utilizing a discrete phase model for the liquid phase with fixed droplet size and reflecting wall model could produce predictions for pressure loss up to $Re_L = 84$ and at lower gas Reynolds numbers. Additionally, the simulation was able to produce acceptable predictions at $Re_G < 110,000$ and $Re_L = 590$.

CHAPTER 5

Research Conclusions & Future Work

5.1   Research Conclusions

Throughout the course of study for this dissertation, several main conclusions and contributions have arisen. The research focused on high Reynolds number mixing with specific application to gas-continuous contact with a liquid phase. The applications for this flow mode ubiquitous and include reactive and non-reactive absorption, cooling, and liquid-stripping. Unfortunately, the literature was lacking critical data and correlations that could be used in practice by the design engineer for actual installations. It has been known that pressure loss estimation is critical for design in terms of mass transfer as well as sizing of downstream equipment and upstream compression. To advance the knowledge in this space and contribute workable semi-empirical models to the open literature, several studies were undertaken to measure pressure loss and develop a correlation and CFD workflow for accurately capturing the pressure loss at high Reynolds numbers.

The corrugated geometry was chosen due to its wide acceptance as the best option for gas-liquid mixing when a highly turbulent gas-continuous phase is present. Additionally, the corrugated geometry is pervasive in structured packing geometries and as such, we expected contributions to over-lap and augment predictions in co-current structured packing installations. The experimental campaign focused on high Reynolds number flows with compressed air in a broad variety of mixer arrangements and pipe diameters ranging from 1-inch to 4-inch. The experimental facilities to accomplish these measurements were constructed completely during this dissertation study and have been described in previous chapters. The experimental data was

117

carefully analyzed, and a correlation was developed for both single- and multi-phase flows starting from theory. The correlations were shown to be extensible to other conditions and geometries by nature of their close relationship with the underlying theory and physics of flow.

In addition to experimental measurements, a CFD workflow was developed for accurately simulating the pressure loss in the complex corrugated geometry, specifically at high Reynolds numbers which had not been attempted previously in literature. Finally, a multi-phase discrete phase approach was applied to aid in predictions at moderate liquid loads and high gas Reynolds number conditions. The following sections outline the concusionts and contributions of this dissertation to the general knowledge.

5.1.1 Single-phase flow

A detailed correlation for the single-phase flow behavior in the corrugated mixer geometry was created, starting from theory of flow in porous media. The correlation fit the data well for both single mixer elements as well as mixer elements in series under different rotational configurations (i.e. rotated or aligned). The correlation relied on intrinsic variables related to the mixer geometry like the tortuosity and void fraction. As such, the correlation is more generalizable to many geometrical variations than previous correlations. Additionally, a CFD workflow was developed and demonstrated for determining the tortuosity of a variant mixer geometry from streamline analysis.

The CFD simulations showed good coherence with the experimental data and correlation. Wall roughness was identified as a critical parameter for accurately predicting the pressure loss. The roughness was shown to contributed up to 55% of the pressure loss at lower Reynolds numbers in the smallest diameter (1-inch) mixing systems. It was shown that the wall roughness,

even when caused by retainers, weld beads, or other small imperfections in the pipe surrounding the mixer are critical factors which must be accounted for when scaling lab data or utilizing for a correlation.

5.1.2   Multi-phase flow

A multi-phase pressure loss model was created utilizing the framework proposed by Lockhart & Martinelli for two-phase flow in pipes. By idealizing the corrugated mixing channel as a conduit, a correlation was developed with accounted for the film entrainment point inside the mixing channel. The correlation showed a good fit with the experimental data, even better than a single-phase model or utilizing a correlation intended for two-phase pipe flow. The onset of entrainment appeared to be an important factor in determining the pressure loss in the mixer at high Reynolds numbers.

A discrete phase model was utilized to simulate the multi-phase flow behavior in the corrugated mixer geometry utilizing CFD. Simplifying assumptions of constant droplet diameter and reflecting (non-absorptive) wall conditions were posited and showed good predictions up to $Re_L = 89$. At higher liquid Reynolds numbers and above about $Re_G = 110{,}000$, the simplified discrete phase model was not able to accurately capture the experimental data. This finding may indicate that more complicated physics begin to control the pressure loss at high liquid loading such as film flow and entrainment.

5.1.3   Future work

Future work should be focused on understanding the mass transfer behavior in the corrugated mixer geometry in the context of pressure loss. With this information, the design engineer may fully specify a unit operation with the mixer. Linking the mass transfer behavior to

the pressure loss is an intuitive and practical way to provide design guidance for co-current flow in these devices.

Additional work is needed to fully understand the multi-phase pressure loss behavior at high gas Reynolds numbers and moderate liquid loads (i.e. $Re_L > 500$). Perhaps more sophisticated CFD models will be capable of elucidating the physics. This work could lead to an enhanced understanding of generalized two-phase flow through porous media in the inertial regime, which is still basic for many scenarios.

On a more practical level, utilizing the findings of this dissertation under field conditions to validate performance would enhance the credibility of the results and help in developing an understanding of any deviations from the original study conditions.

REFERENCES

1. Paul, E.L.; Atiemo-obeng, V.A.; Kresta, S.M. *Handbook of Industrial Mixing Science and Practice*; Wiley-Interscience, 2004; ISBN 3175723993.

2. Lockhart, R.W.; Martinelli, R.C. Proposed correlation of data for isothermal two-phase, two-component flow in pipes. *Chem. Eng. Prog.* **1949**, *45*, 39–48.

3. ISHII, M.; GROLMES, M.A. Inception Criteria for Droplet Entrainment in Two Phase Concurrent Film Flow. **1975**, *21*.

4. Mokhatab, S.; Poe, W.; Mak, J. *Handbook of Natural Gas Transmission and Processing*; 3rd ed.; Gulf Publishing Company, 2015; ISBN 9780128014998.

5. Farquharson, D.; Jaramillo, P.; Schivley, G.; Klima, K.; Carlson, D.; Samaras, C. Beyond global warming potential: a comparative application of climate impact metrics for the life cycle assessment ofcoal and natural gas based electricity. *J. Ind. Ecol.* **2016**, *41*.

6. Schivley, G.; Azevedo, I.; Samaras, C. Assessing the evolution of power sector carbon intensity in the United States. *Environ. Res. Lett.* **2018**, *13*, doi:10.1088/1748-9326/aabe9d.

7. Srinivasan, V.; Aiken, R.C. Selective absorption of H2S from CO2 - factors controlling selectivity toward H2S. *Fuel Process. Technol.* **1988**, *19*, 141–152, doi:10.1016/0378-3820(88)90062-8.

8. Mamrosh, D.; McIntush, K.; Fisher, K. Caustic scrubber designs for H2S removal from refinery gas streams. In Proceedings of the American Fuel and Petrochemical Manufacturers, AFPM - AFPM Annual Meeting 2014; 2014.

9. Addington, L.; Ness, C. An evaluation of general "rules of thumb" in amine sweetening unit design and operation. *GPA Annu. Conv. Proc.* **2010**, *1*, 119–135.

10. Hajiw, M.; Chapoy, A.; Coquelet, C.; Lauermann, G. Prediction of methanol content in

natural gas with the GC-PR-CPA model. *J. Nat. Gas Sci. Eng.* **2015**, *27*, 745–750, doi:10.1016/j.jngse.2015.09.021.

11.   Lowry, E.; Yuan, Y.; Thomas, D.; Maydak, S. Removal of Methanol from Natural Gas Liquids Using a Proven Extraction Technology. In Proceedings of the 70th Annual Laurance Reid Gas Conditioning Conference; University of Oklahoma: Norman, OK, 2020.

12.   Bahadori, A.; Vuthaluru, H.B. Simple methodology for sizing of absorbers for TEG (triethylene glycol) gas dehydration systems. *Energy* **2009**, *34*, 1910–1916, doi:10.1016/j.energy.2009.07.047.

13.   Edmister, W.C. Design for Hydrocarbon Absorption and Stripping. *Ind. Eng. Chem.* **1943**, *35*, 837–839.

14.   Kuo, J.C.; Wang, K.H.; Chen, C. Pros and cons of different Nitrogen Removal Unit (NRU) technology. *J. Nat. Gas Sci. Eng.* **2012**, *7*, 52–59, doi:10.1016/j.jngse.2012.02.004.

15.   Charpentier, J.C. *Mass-transfer rates in gas-liquid absorbers and reactors*; 1981; Vol. 11; ISBN 0120085119.

16.   Paglianti, A.; Montante, G. A mechanistic model for pressure drops in corrugated plates static mixers. *Chem. Eng. Sci.* **2013**, *97*, 376–384, doi:10.1016/j.ces.2013.04.042.

17.   Bravo, J.L.; Rocha, J.A.; Fair, J.R. Pressure Drop in Structured Packings. *Hydrocarb. Process.* **1986**, *65*.

18.   Cavatorta, O.N.; Böhm, U.; De Del Giorgio, A.M.C. Fluid-dynamic and mass-transfer behavior of static mixers and regular packings. *AIChE J.* **1999**, *45*, 938–948, doi:10.1002/aic.690450504.

19.   Couvert, A.; Péculier, M.-F.; Laplanche, A. Pressure Drop and Mass Transfer Study in Static Mixers with Gas Continuous Phase. *Can. J. Chem. Eng.* **2002**, *80*, 727–733, doi:10.1002/cjce.5450800426.

20.   Thakur, R.K.; Vial, C.; Nigam, K.D.P.; Nauman, E.B.; Djelveh, G. Static mixers in the

process industries - a review. *Chem. Eng. Res. Des.* **2003**, *81*, 787–826, doi:10.1205/026387603322302968.

21. Paglianti, A. Recent Innovations in Turbulent Mixing with Static Elements. *Recent Patents Chem. Eng.* **2012**, *1*, 80–87, doi:10.2174/2211334710801010080.

22. Turunen, I.; Haario, H. Mass transfer in tubular reactors equipped with static mixers. *Chem. Eng. Sci.* **1994**, *49*, 5257–5269, doi:10.1016/0009-2509(94)00277-0.

23. Sanchez, C.; Couvert, A.; Laplanche, A.; Renner, C. Hydrodynamic and mass transfer in a new co-current two-phase flow gas-liquid contactor. *Chem. Eng. J.* **2007**, *131*, 49–58, doi:10.1016/j.cej.2006.12.004.

24. Jaworski, Z.; Pianko-Oprych, P.; Marchisio, D.L.; Nienow, A.W. CFD modelling of turbulent drop breakage in a kenics static mixer and comparison with experimental data. *Chem. Eng. Res. Des.* **2007**, *85*, 753–759, doi:10.1205/cherd06179.

25. Konopacki, M.; Kordas, M.; Fijałkowski, K.; Rakoczy, R. Computational fluid dynamics and experimental studies of a new mixing element in a static mixer as a heat exchanger. *Chem. Process Eng. - Inz. Chem. i Proces.* **2015**, *36*, 59–72, doi:10.1515/cpe-2015-0005.

26. Rauline, D.; Tanguy, P.A.; Le Blévec, J.M.; Bousquet, J. Numerical investigation of the performance of several static mixers. *Can. J. Chem. Eng.* 1998, *76*, 527–535.

27. Valenz, L.; Rejl, F.J.; Šíma, J.; Linek, V. Absorption mass-transfer characteristics of mellapak packings series. *Ind. Eng. Chem. Res.* **2011**, *50*, 12134–12142, doi:10.1021/ie200577k.

28. Madhuranthakam, C.M.R.; Pan, Q.; Rempel, G.L. Hydrodynamics in sulzer SMX static mixer with air/water system. *Ind. Eng. Chem. Res.* **2009**, *48*, 719–726, doi:10.1021/ie801407y.

29. Suess, P.; Spiegel, L. Hold-up of mellapak structured packings. *Chem. Eng. Process.* **1992**, *31*, 119–124, doi:10.1016/0255-2701(92)85005-M.

30. Streiff, F.A.; Jaffer, S.; Schneider, G.; Engineers, S. of C. *The Design and Application of*

Static Mixer Technology; PROCEEDINGS OF INTERNATIONAL SYMPOSIUM ON MIXING IN INDUSTRIAL PROCESSES; Society of Chemical Engineers, Japan, 1999;

31.   Brunazzi, E.; Paglianti, A. Liquid-Film Mass-Transfer Coefficient in a Column Equipped with Structured Packings. *Ind. Eng. Chem. Res.* **1997**, *36*, 3792–3799, doi:10.1021/ie970045h.

32.   Geuzaine, C.; Remacle, J.F. Gmsh: A 3-D finite element mesh generator with built-in pre- and post-processing facilities. *Int. J. Numer. Methods Eng.* **2009**, *79*, 1309–1331, doi:10.1002/nme.2579.

33.   Zeng, M.; Tao, W.Q. A comparison study of the convergence characteristics and robustness for four variants of SIMPLE-family at fine grids. *Eng. Comput. (Swansea, Wales)* **2003**, *20*, 320–340, doi:10.1108/02644400310467234.

34.   Shih, T.-H.; Liou, W.W.; Shabbir, A.; Yang, Z.; Zhu, J. A new k-e eddy viscosity model for high:reynolds number turbulent flows. *Comput. Fluids* **1995**, *24*, 227–238, doi:10.1016/0045-7930(94)00032-T.

35.   Cebeci, T.; Bradshaw, P. *Momentum Transfer in Boundary Layers*; Hemisphere Publishing Corp., 1977;

36.   Matyka, M.; Koza, Z. How to calculate tortuosity easily? *AIP Conf. Proc.* **2011**, *1453*, 17–22, doi:10.1063/1.4711147.

37.   Zare, M.; Hashemabadi, S.H. CFD simulation and experimental validation of tortuosity effects on pellet-fluid heat transfer of regularly stacked multi-lobe particles. *Chem. Eng. J.* **2019**, *361*, 1543–1556, doi:10.1016/j.cej.2018.10.188.

38.   Comiti, J.; Renaud, M. A new model for determining mean structure parameters of fixed beds from pressure drop measurements: application to beds packed with parallelepipedal particles. *Chem. Eng. Sci.* **1989**, *44*, 1539–1545, doi:10.1016/0009-2509(89)80031-4.

39.   Morancais, P.; Hirech, K.; Carnelle, G.; Legrand, J. Friction factor in static mixer and determination of geometric parameters of smx sulzer mixers. *Chem. Eng. Commun.* **1999**, *171*, 77–93, doi:10.1080/00986449908912750.

40. Legrand, J. Revisited Analysis of Pressure Drop in Flow through Crushed Rocks. *J. Hydraul. Eng.* **2002**, *128*, 1027–1031, doi:10.1061/(asce)0733-9429(2002)128:11(1027).

41. Wyllie, M.R.J.; Gregory, A.R. Fluid Flow through Unconsolidated Porous Aggregates. *Ind. Eng. Chem.* **1955**, *47*, 1379–1388, doi:10.1021/ie50547a037.

42. Nikuradse, J. *Stromungsgesetze in rauhen Rohren*; 1933;

43. Lage, J.L.; Antohe, B. V. Darcy ' s Experiments and the Deviation to Nonlinear Flow. *J. Fluids Eng. Trans. ASME* **2016**, *122*, 619–625.

44. Stewart, M.I. Chapter 9: Gas Sweetening. In *Surface Production Operations, Volume 2: Design of Gas-Handling Systems and Facilities*; 2014; pp. 433–539 ISBN 9780123822079.

45. Ghanem, A.; Lemenand, T.; Della Valle, D.; Peerhossaini, H. Static mixers: Mechanisms, applications, and characterization methods - A review. *Chem. Eng. Res. Des.* **2014**, *92*, 205–228, doi:10.1016/j.cherd.2013.07.013.

46. Mamrosh, D.L.; Beitler, C.A.M.; Benn, B.; McIntush, K.E.; Hileman, O.E. Use of Caustic in a Short Contact Time Approach to Selectively Scrub H2S from CO2-Contaminated Gas Streams. In Proceedings of the Proceedings of the 59th Laurance Reid Gas Conditioning Conference; University of Oklahoma, 2009.

47. Reiss, L.P. Cocurrent Gas-Liquid Contacting in Packed Columns. *I&EC Process Des. Dev.* **1967**, *6*, 486–499.

48. Taylor, G.N.; Matherly, R. Structural elucidation of the solid byproduct from the use of 1,3,5-tris(hydroxyalkyl)hexahydro-s-triazine based hydrogen sulfide scavengers. *Ind. Eng. Chem. Res.* **2011**, *50*, 735–740, doi:10.1021/ie101985v.

49. Eow, J.S. Recovery of sulfur from sour acid gas: A review of the technology. *Environ. Prog.* **2002**, *21*, 143–162, doi:10.1002/ep.670210312.

50. Hohlfeld, R.W. Selective Absorption of H2S From Sour Gas. **1979**, 1083–1089, doi:10.2118/7972-pa.

51.   Ling, K. Gas Viscosity at High Pressure and High Temperature, Texas A&M University, 2012.

52.   Tsai, R.E.; Siebert, F.; Eldridge, B.; Rochelle, G.T. A Dimensionless Model for Predicting the Mass-Transfer Area of Structured Packing. *AIChE J.* **2011**, *57*, 1173–1184.

53.   Zhu, Z.; Hannon, J.; Green, A. Use of high intensity gas-liquid mixers as reactors. *Chem. Eng. Sci.* **1992**, *47*, 2847–2852, doi:10.1016/0009-2509(92)87140-L.

54.   Lehmann, M.; Pojtanabuntoeng, T.; Long, Y.; Yookhong, M.; Iannuzzi, M. Evaluation of Hydrogen Sulfide Scavengers for Use with Static Mixers. In Proceedings of the Offshore Technology Conference Asia; 2020.

55.   Celik, I.B.; Ghia, U.; Roache, P.J.; Freitas, C.J.; Coleman, H.; Raad, P.E. Procedure for estimation and reporting of uncertainty due to discretization in CFD applications. *J. Fluids Eng. Trans. ASME* **2008**, *130*, 0780011–0780014, doi:10.1115/1.2960953.

56.   Roache, P.J. Quantification of uncertainty in computational fluid dynamics. *Annu. Rev. Fluid Mech.* **1997**, *29*, 123–160, doi:10.1146/annurev.fluid.29.1.123.

57.   Apsley, D. CFD calculation of turbulent flow with arbitrary wall roughness. *Flow, Turbul. Combust.* **2007**, *78*, 153–175, doi:10.1007/s10494-006-9059-x.

58.   Suga, K.; Craft, T.J.; Iacovides, H. An analytical wall-function for turbulent flows and heat transfer over rough walls. *Int. J. Heat Fluid Flow* **2006**, *27*, 852–866, doi:10.1016/j.ijheatfluidflow.2006.03.011.

59.   Meana-Fernández, A.; Fernández Oro, J.M.; Argüelles Díaz, K.M.; Galdo-Vega, M.; Velarde-Suárez, S. Application of Richardson extrapolation method to the CFD simulation of vertical-axis wind turbines and analysis of the flow field. *Eng. Appl. Comput. Fluid Mech.* **2019**, *13*, 359–376, doi:10.1080/19942060.2019.1596160.

60.   Moody, L.F. Friction factors for pipe flow. *Trans. ASME* **1944**, *66*, 671–684.

61.   Kadivar, M.; Tormey, D.; McGranaghan, G. A review on turbulent flow over rough surfaces: Fundamentals and theories. *Int. J. Thermofluids* **2021**, *10*, 100077,

doi:10.1016/j.ijft.2021.100077.

62. Lowry, E.; Yuan, Y.; Krishnamoorthy, G. A new correlation for single-phase pressure loss through SMV static mixers at high Reynolds numbers. *Chem. Eng. Process. - Process Intensif.* **2022**, *171*, 108716, doi:10.1016/j.cep.2021.108716.

63. Botros, K.K. Experimental Investigation into the Relationship between the Roughness Height in Use with Nikuradse or Colebrook Roughness Functions and the Internal Wall Roughness Profile for Commercial Steel Pipes. *J. Fluids Eng. Trans. ASME* **2016**, *138*, 1–8, doi:10.1115/1.4032601.

64. Langelandsvik, L.I.; Kunkel, G.J.; Smits, A.J. Flow in a commercial steel pipe. *J. Fluid Mech.* **2008**, *595*, 323–339, doi:10.1017/S0022112007009305.

65. Galavics, F. Die Methode der Rauhigkeits-Charakteristik zur Ermittlung der Rohrreibung in geraden Stahlrohr-Fernleitungen. *Fernheizkraftw. d. ETH.* **1939**.

66. Couvert, A.; Sanchez, C.; Charron, I.; Laplanche, A.; Renner, C. Static mixers with a gas continuous phase. *Chem. Eng. Sci.* **2006**, *61*, 3429–3434, doi:10.1016/j.ces.2005.11.040.

67. J., O., H. *Turbulence*; 2nd ed.; McGraw-Hill Companies: New York, 1975;

68. Lewis, A.; B.E. Estimating volume flow rates through xylem conduits. *Am. J. Bot.* **2011**, *82*, 1112–1116.

69. Song, H.S.; Han, S.P. A general correlation for pressure drop in a Kenics static mixer. *Chem. Eng. Sci.* **2005**, *60*, 5696–5704, doi:10.1016/j.ces.2005.04.084.

70. Flack, K.A.; Schultz, M.P.; Barros, J.M. Skin Friction Measurements of Systematically-Varied Roughness: Probing the Role of Roughness Amplitude and Skewness. *Flow, Turbul. Combust.* **2020**, *104*, 317–329, doi:10.1007/s10494-019-00077-1.

71. Malico, I.; Ferreira de Sousa, P.J.S.A. Pressure Drop through Structured Porous Media - Inlet and Outlet Effects. *Diffus. Found.* **2017**, *10*, 55–69, doi:10.4028/www.scientific.net/df.10.55.

72. Azizi, F.; Al Taweel, A.M. Mass Transfer in an Energy-Efficient High-Intensity Gas-

Liquid Contactor. *Ind. Eng. Chem. Res.* **2015**, *54*, 11635–11652, doi:10.1021/acs.iecr.5b01078.

73. Munter, R. Comparison of mass transfer efficiency and energy consumption in static mixers. *Ozone Sci. Eng.* **2010**, *32*, 399–407, doi:10.1080/01919512.2010.517492.

74. Ishii, M.; Grolmes, M.A. Inception criteria for droplet entrainment in two-phase concurrent film flow. *AIChE J.* **1975**, *21*, 308–318, doi:10.1002/aic.690210212.

75. Tsai, R.E.; Schultheiss, P.; Kettner, A.; Lewis, J.C.; Seibert, A.F.; Eldridge, R.B.; Rochelle, G.T. Influence of surface tension on effective packing area. *Ind. Eng. Chem. Res.* **2008**, *47*, 1253–1260, doi:10.1021/ie070780l.

76. Zakeri, A.; Einbu, A.; Svendsen, H.F. Experimental investigation of pressure drop in structured packings. *Chem. Eng. Sci.* **2012**, *73*, 285–298, doi:10.1016/j.ces.2012.01.025.

77. Stichlmair, J.; Bravo, J.L. General model for prediction of pressure drop and capacity of countercurrent gas/liquid packed columns. *Gas Sep. Purif.* **1989**, *3*, 19–28, doi:10.1021/ja01267a009.

78. Rocha, J.A.; Bravo, J.L.; Fair, J.R. Distillation Columns Containing Structured Packings: A Comprehensive Model for Their Performance. 1. Hydraulic Models. **1993**, 641–651.

79. Brunazzi, E.; Paglianti, A. Mechanistic Pressure Drop Model for Columns Containing Structured Packings. *AIChE J.* **1997**, *43*, 317–327, doi:10.1002/aic.690430205.

80. Ettiyappan, P.; Babu, J.; Arunagiri, A.; Murugesan, T. Prediction of two-phase pressure drop and liquid holdup in co-current gas-liquid downflow of air-Newtonian systems through packed beds. *J. Chem. Technol. Biotechnol.* **2006**, *81*, 70–81, doi:10.1002/jctb.1359.

81. Lavalle, G.; Lucquiaud, M.; Wehrli, M.; Valluri, P. Cross-flow structured packing for the process intensification of post-combustion carbon dioxide capture. *Chem. Eng. Sci.* **2018**, *178*, 284–296, doi:10.1016/j.ces.2017.12.022.

82. Mamrosh, D.; Bettler, C.; Fisher, K.; Stem, S. Consider improved scrubbing designs for

acid gases : Better application of process chemistry enables efficient sulfur abatement : Gas processing developments. *Hydrocarb. Process. (International ed.)* **2008**, *87*.

83. Demmink, J.F.; Wubs, H.J.; Beenackers, A.A.C.M. Oxidative Absorption of Hydrogen Sulfide by a Solution of Ferric Nitrilotriacetic Acid Complex in a Cocurrent Down Flow Column Packed with SMV-4 Static Mixers. *Ind. Eng. Chem. Res.* **1994**, *33*, 2989–2995, doi:10.1021/ie00036a013.

84. Battista, J.; Böhm, U. Mass transfer in trickle-bed reactors with structured packing. *Chem. Eng. Technol.* **2003**, *26*, 1061–1067, doi:10.1002/ceat.200301739.

85. Raynal, L.; Ballaguet, J.P.; Barrere-Tricca, C. Determination of mass transfer characteristics of co-current two-phase flow within structured packing. In Proceedings of the Chemical Engineering Science; 2004; Vol. 59, pp. 5395–5402.

86. McAdams, W.H. Vaporization inside horizontal tubes-II, Benzene oil mixtures. *Trans. ASME* **1942**, *64*, 193–200.

87. Dukler, A.E.; Moye Wicks, I.; Cleveland, R.G. Frictional pressure drop in two-phase flow: A. A comparison of existing correlations for pressure loss and holdup. *AIChE J.* **1964**, *10*, 38–43.

88. Thome, J.; Cioncolini, A. Two-Phase Pressure Drop. In *Encyclopedia of Two-Phase Heat Transfer and Flow I*; World Scientific, 2017; pp. 143–176 ISBN 9789814623216.

89. Chisholm, D. A theoretical basis for the Lockhart-Martinelli correlation for two-phase flow. *Int. J. Heat Mass Transf.* **1967**, *10*, 1767–1778, doi:10.1016/0017-9310(67)90047-6.

90. Awad, M.M. Two-Phase Flow Modeling in Circular Pipes, 2007.

91. Muzychka, Y.S.; Awad, M.M. Asymptotic generalizations of the lockhart-martinelli method for two phase flows. *J. Fluids Eng. Trans. ASME* **2010**, *132*, 0313021–03130212, doi:10.1115/1.4001157.

92. Shah, N.F.; Kale, D.D. Two-phase, gas-liquid flows in static mixers. *AIChE J.* **1992**, *38*, 308–310, doi:10.1002/aic.690380218.

93.	Larkins, R.P.; White, R.R.; Jeffrey, D.W. Two-phase concurrent flow in packed beds. *AIChE J.* **1961**, *7*, 231–239, doi:10.1002/aic.690070213.

94.	Sato, Y.; Hirose, T.; Takahashi, F.; Toda, M. Pressure loss and liquid holdup in packed bed reactor with cocurrent gas–liquid down flow. *J. Chem. Eng. Japan* **1973**, *6*, 147–152.

95.	Leppin, D.; Fisher, K.; Matonis, D. Modeling direct injection of H2S scavenger in pipelines: Laboratory investigations and improved computer model. In Proceedings of the GPA Annual Convention Proceedings; 2009; Vol. 1, pp. 253–270.

96.	Martinelli, R.C.; Nelson, D.B. Prediction of pressure drop during forced-circulation boiling of water. *Trans. ASME* **1948**, *70*, 695–702.

97.	Whalley, P.B. *Two-Phase Flow and Heat Transfer*; No. 42.; Oxford University Press: USA, 1996;

98.	Lopez de Bertodano, M.A.; Assad, A.; Beus, S.G. Experiments for entraiment rate of droplets in the annular regime. *Int. J. Multiph. Flow* **2001**, *27*, 685–699, doi:10.1016/S0301-9322(00)00046-X.

99.	Berna, C.; Escrivá, A.; Muñoz-Cobo, J.L.; Herranz, L.E. Review of droplet entrainment in annular flow: Interfacial waves and onset of entrainment. *Prog. Nucl. Energy* **2014**, *74*, 14–43, doi:10.1016/j.pnucene.2014.01.018.

100.	Mantilla, I.; Gomez, L.; Mohan, R.; Shoham, O.; Kouba, G.; Roberts, R. Modeling of liquid entrainment in gas in horizontal pipes. *Proc. ASME Fluids Eng. Div. Summer Conf. 2009, FEDSM2009* **2009**, *1*, 979–1007, doi:10.1115/FEDSM2009-78459.

101.	Sun, L.; Mishima, K. Evaluation analysis of prediction methods for two-phase flow pressure drop in mini-channels. *Int. Conf. Nucl. Eng. Proceedings, ICONE* **2008**, *2*, 649–658, doi:10.1115/ICONE16-48210.

102.	Rocha, J.A.; Bravo, J.L.; Fair, J.R. Distillation columns containing structured packings: A comprehensive model for their performance. 2. Mass-transfer model. *Ind. Eng. Chem. Res.* **1996**, *35*, 1660–1667, doi:10.1021/ie940406i.